Date: April 8, 2018

Proposal for JLab PAC45

PR12–17–001

Strange Hadron Spectroscopy with a Secondary K_L Beam at GlueX

S. Adhikari[13], H. Al Ghoul[14], A. Ali[20], M. J. Amaryan[37,*,†], E. G. Anassontzis[2], A. V. Anisovich[4,28], A. Austregesilo[46], M. Baalouch[37], F. Barbosa[46], A. Barnes[10], M. Bashkanov[11,†], T. D. Beattie[43], R. Bellwied[21], V. V. Berdnikov[35], T. Black[39], W. Boeglin[13], W. J. Briscoe[15], T. Britton[46], W. K. Brooks[45], B. E. Cannon[14], E. Chudakov[46], P. L. Cole[22], V. Crede[14], M. M. Dalton[46], A. Deur[46], P. Degtyarenko[46], S. Dobbs[14], G. Dodge[37], A. G. Dolgolenko[29], M. Döring[15,46], M. Dugger[1], R. Dzhygadlo[20], R. Edwards[46], H. Egiyan[46], S. Eidelman[5,41], A. Ernst[14], A. Eskandarian[15], P. Euginio[14], C. Fanelli[33], S. Fegan[15], C. Fernandez-Ramirez[34], A. M. Foda[43], J. Frye[23], S. Furletov[46], L. Gan[39], A. Gasparian[38], G. Gavalian[46], V. Gauzshtein[47,48], N. Gevorgyan[57], D. I. Glazier[18], J. Goity[46,19], K. Götzen[20], V. S. Goryachev[29], L. Guo[13], H. Haberzettl[15], M. Hadžimehmedović[50], H. Hakobyan[45], A. Hamdi[20], S. Han[56], J. Hardin[33], A. Hayrapetyan[17], T. Horn[8], G. M. Huber[43], C. E. Hyde[37], D. G. Ireland[18], M. M. Ito[46], B. C. Jackson[16], N. S. Jarvis[7], R. T. Jones[10], V. Kakoyan[57], G. Kalicy[8], M. Kamel[13], C. D. Keith[46], C. W. Kim[15], F. J. Klein[15], C. Kourkoumeli[2], G. Krafft[46], S. Kuleshov[45], I. Kuznetsov[47,48], A. B. Laptev[31], I. Larin[29], D. Lawrence[46], M. Levillain[38], W. I. Levine[7], K. Livingston[18], G. J. Lolos[43], V. E. Lyubovitskij[47,48,49,45], D. Mack[46], M. Mai[15], D. M. Manley[27], H. Marukyan[57], U.-G. Meißner[4,26], V. Mathieu[23], M. Matveev[28], V. Matveev[29], M. McCaughan[46], M. McCracken[7], W. McGinley[7], J. McIntyre[10], C. A. Meyer[7], R. Miskimen[32], R. E. Mitchell[23], F. Mokaya[10], V. Mokeev[46], B. Moussallam[49], K. Nakayama[16], F. Nerling[20], Y. Oh[30], H. Osmanović[50], A. I. Ostrovidov[14], R. Omerović[50], Z. Papandreou[43], K. Park[46], E. Pasyuk[46], M. Patsyuk[33], P. Pauli[18], R. Pedroni[38], J. R. Pelaez[51], M. R. Pennington[18], L. Pentchev[46], K. J. Peters[20], W. Phelps[15], A. Pilloni[46], E. Pooser[46], B. Pratt[10], J. W. Price[6], N. Qin[56], J. Reinhold[13], D. Richards[46], D.-O. Riska[12], B. G. Ritchie[1], J. Ritman[3,25,†], L. Robison[40], A. Rodas[51], D. Romanov[35], J. Ruiz de Elvira[50], H-Y. Ryu[42], C. Salgado[36], E. Santopinto[24], A. V. Sarantsev[4,28], R. A. Schumacher[7], C. Schwarz[20], J. Schwiening[20], A. Semenov[43], I. Semenov[43], K. K. Seth[40], M. R. Shepherd[23], E. S. Smith[46], D. I. Sober[8], D. Sokhan[18], A. Somov[46], S. Somov[35], O. Soto[45], N. Sparks[1], J. Stahov[51], M. J. Staib[7], J. R. Stevens[55,†], I. I. Strakovsky[15,†], A. Subedi[23], A. Švarc[44], A. Szczepaniak[23,46], V. Tarasov[29], S. Taylor[46], A. Teymurazyan[43], A. Tomaradze[40], A. Tsaris[14], G. Vasileiadis[2], D. Watts[11], D. Werthmüller[18], N. Wickramaarachchi[37], T. Whitlatch[46], M. Williams[33], B. Wojtsekhowski[46], R. L. Workman[15], T. Xiao[40], Y. Yang[33], N. Zachariou[11], J. Zarling[23], J. Zhang[52], Z. Zhang[56], B. Zou[9], X. Zhou[56], B. Zihlmann[46]

[1] Arizona State University, Tempe, AZ 85287, USA
[2] National and Kapodistrian University of Athens, Athens 15771, Greece
[3] Institut für Experimentalphysik I - Ruhr-Universität, Bochum 44780, Germany
[4] Helmholtz-Institut für Strahlen- und Kernphysik, Universität Bonn, Bonn 53115, Germany
[5] Budker Institute of Nuclear Physics SB RAS, Novosibirsk 630090, Russia
[6] California State University, Dominguez Hills, Carson, CA 90747, USA
[7] Carnegie Mellon University, Pittsburgh, PA 15213, USA
[8] The Catholic University of America, Washington, DC 20064, USA
[9] Institute of Theoretical Physics CAS, Beijing 100190, People's Republic of China
[10] University of Connecticut, Storrs, CO 06269, USA
[11] University of Edinburgh, Edinburgh EH9 3FD, United Kingdom
[12] Finnish Society of Science and Letters, Helsinki 00130, Finland
[13] Florida International University, Miami, FL 33199, USA
[14] Florida State University, Tallahassee, FL 32306, USA
[15] The George Washington University, Washington, DC 20052, USA
[16] University of Georgia, Athens, GA 30602, USA
[17] II. Physikalisches Institut, Justus Liebig-University of Giessen, Giessen 35392, Germany
[18] University of Glasgow, Glasgow G12 8QQ, United Kingdom
[19] Hampton University, Hampton, VA 23668, USA
[20] GSI Helmholtzzentrum für Schwerionenforschung GmbH, Darmstadt 64291, Germany
[21] University of Houston, Houston, TX 77204, USA
[22] Idaho State University, Pocatello, ID 83209, USA
[23] Indiana University, Bloomington, IN 47403, USA
[24] I.N.F.N. Sezione di Genova, Genova 16146, Italy
[25] Institute für Kernphysik & Jülich Center für Hadron Physics, Jülich 52425, Germany
[26] Institute for Advanced Simulation, Institut für Kernphysik and Jülich Center for Hadron Physics, Jülich 52425, Germany
[27] Kent State University, Kent, OH 44242, USA
[28] National Research Centre "Kurchatov Institute", Petersburg Nuclear Physics Institute, Gatchina 188300, Russia
[29] National Research Centre "Kurchatov Institute", Institute for Theoretical and Experimental Physics, Moscow 117218, Russia
[30] Kyungpook National University, Daegu 702-701, Republic of Korea
[31] Los Alamos National Laboratory, Los Alamos, NM 87545, USA
[32] University of Massachusetts, Amherst, MA 01003, USA
[33] Massachusetts Institute of Technology, Cambridge, MA 02139, USA
[34] Instituto de Ciencias Nucleares, Universidad Nacional Autonoma de Mexico, Ciudad de Mexico 04510, Mexico
[35] National Research Nuclear University Moscow Engineering Physics Institute, Moscow 115409, Russia
[36] Norfolk State University, Norfolk, VA 23504, USA
[37] Old Dominion University, Norfolk, VA 23529, USA
[38] North Carolina A&T State University, Greensboro, NC 27411, USA
[39] University of North Carolina at Wilmington, Wilmington, NC 28403, USA
[40] Northwestern University, Evanston, IL 60208, USA

[41] Novosibirsk State University, Novosibirsk 630090, Russia
[42] Pusan National University, Busan 46241, Republic of Korea
[43] University of Regina, Regina, SA S4S 0A2, Canada
[44] Rudjer Bošković Institute, Zagreb 10002, Croatia
[45] Universidad Técnica Federico Santa María, Casilla 110-V Valparaíso, Chile
[46] Thomas Jefferson National Accelerator Facility, Newport News, VA 23606, USA
[47] Tomsk State University, Tomsk 634050, Russia
[48] Tomsk Polytechnic University, Tomsk 634050, Russia
[49] Institute of Theoretical Physics, University of Tübingen, Tübingen 72076, Germany
[50] University of Bern, CH-3012 Bern, Switzerland
[51] Universidad Complutense de Madrid, 28040 Madrid, Spain
[52] Universite Paris-Sud 11, 91400 Orsay, France
[53] University of Tuzla, Tuzla 75000, Bosnia and Herzegovina
[54] University of Virginia, Charlottesville, VA 22904, USA
[55] College of William and Mary, Williamsburg, VA 23185, USA
[56] Wuhan University, Wuhan, Hubei 430072, People's Republic of China
[57] Yerevan Physics Institute, Yerevan 0036, Armenia
[*] Contact Person: mamaryan@odu.edu
[†] Spokesperson

(The GLUEX Collaboration)

Abstract

We propose to create a secondary beam of neutral kaons at Hall D at Jefferson Lab to be used with the GlueX experimental setup for strange hadron spectroscopy. The superior CEBAF electron beam will enable a flux on the order of $1 \times 10^4\ K_L/s$, which exceeds the magnitude of that previously attained at SLAC by three orders of magnitude. This will allow a broad range of measurements that will correspondingly improve the statistics of earlier data obtained on a hydrogen targets likewise by three orders of magnitude. The use of a deuteron target will provide first measurements ever with neutral kaons on neutrons.

The experiment will measure both differential cross sections and self-analyzed polarizations of the produced Λ, Σ, Ξ, and Ω hyperons using the GlueX detector at the Jefferson Lab Hall D. The measurements will span CM $\cos\theta$ from -0.95 to 0.95 in the range W = 1490 MeV to 2500 MeV. These new GlueX data will greatly constrain partial-wave analyses and reduce model-dependent uncertainties in the extraction of strange resonance properties (including pole positions), and provide a new benchmark for comparisons with QCD-inspired models and lattice QCD calculations.

The proposed facility will also have an impact in the strange meson sector by providing measurements of the final-state $K\pi$ system from threshold up to 2 GeV invariant mass to establish and improve on the pole positions and widths of all $K^*(K\pi)$ P-wave states as well as for the S-wave scalar meson $\kappa(800)$.

Contents

1 Executive Summary

We propose to establish a secondary K_L beamline at JLab Hall D for scattering experiments on both proton and neutron (for the first time) targets in order to determine the differential cross sections and the self-polarization of strange hyperons with the GlueX detector to enable precise partial wave analysis (PWA) in order to determine all the resonances up to 2500 MeV in the spectra of the Λ, Σ, Ξ, and Ω hyperons.

In addition, we intend to do strange meson spectroscopy by studies of the $\pi - K$ interaction to locate the pole positions in the $I = 1/2$ and $3/2$ channels.

The K_L beam will be generated by directing a high energy, high intensity photon beam onto a Be-target in front of the GlueX detector. The flux of the K_L beam will be of the order 1×10^4 K_L/s on a liquid hydrogen/deuterium (LH_2/LD_2) cryogenic target within the GlueX detector, which has a large acceptance with coverage of both charged and neutral particles. This flux will allow statistics in the case of hydrogen targets to exceed that of earlier experiments by almost three orders of magnitude. The main components of the experimental setup are the Compact Photon Source, the Be-target assembly with a beam plug, and sweeping magnet.

The physics case for the experiments is aligned with the *2015 Long Range Plan for Nuclear Science* [1]: "*...a better understanding of the role of strange quarks became an important priority*". Knowledge of the hyperon spectra is an important component for this. The empirical knowledge of the low lying spectra of the Λ and Σ hyperons remains very poor in comparison with that of the nucleon, and in the case of the Ξ hyperons extremely poor. The structure of these hyperon resonances cannot be understood without empirical determination of their pole positions and decays, which is the goal of the proposed experiments. The determination of the strange hyperon spectra in combination with the current measurements of the spectra of the charm and beauty hyperons at the LHCb experiment at CERN should allow a clear understanding of soft QCD matter and the approach to heavy quark symmetry.

As the first stage of the GlueX program the focus will be on two-body and quasi-two-body reactions: elastic $K_L p \to K_S p$ and charge-exchange $K_L p \to K^+ n$ reactions, then on two-body reactions producing $S = -1 (S = -2)$ hyperons as $K_L p \to \pi^+ \Lambda$, $K_L p \to \pi^+ \Sigma^0$, and $K_L p \to \pi^0 \Sigma^+ (K_L p \to K^+ \Xi^0)$, as well as three body $K_L p \to K^+ K^+ \Omega^-$.

For analyzing the data a coupled channel PWA of the GlueX data will be done in parallel with an analysis of the data from the J-PARC K^- measurements, when available. The best fit will determine the partial wave amplitudes and the resonance pole positions, residues and Breit-Wigner (BW) parameters. These will provide a benchmark for results of forthcoming QCD lattice calculations and lead to the desired understanding of the structure of the strange hyperons.

Our timeline is to begin K_L beam experiments at the completion of the current GlueX physics program.

2 Scope of the Proposal

The nature of QCD confinement continues to provide a challenge to our understanding of soft QCD. Experimental investigation of the baryon spectrum provides the obvious avenue to understand QCD in this region since the location and properties of the excited states depend on the confining interaction and the relevant degrees of freedom of hadrons.

Through analyses of decades worth of data, from both hadronic and electromagnetic (EM) scattering experiments, numerous baryon resonances have been observed, many of which with masses, widths, and quantum numbers fully determined. There are 109 baryons in the PDG2016 listings, but only 58 of them with 4^* or 3^* quality [2]. Many more states are predicted by quark models (QMs). For example, in the case of $SU(6)_F \times O(3)$ symmetry, 434 resonances would be required, if all partly revealed multiplets were completed (three 70-plets and four 56-plets).

The light and strange quarks can be arranged in six baryonic families, N^*, Δ^*, Λ^*, Σ^*, Ξ^*, and Ω^*. The possible number of members in a family is not arbitrary [3]. Under the $SU(3)_F$ symmetry these are the octet: N^*, Λ^*, and Σ^*, and the decuplet: Δ^*, Σ^*, Ξ^*, and Ω^*. The number of experimentally identified resonances in each baryon family in PDG2016 summary tables is 17 N^*, 24 Δ^*, 14 Λ^*, 12 Σ^*, 7 Ξ^*, and 2 Ω^*. Constituent QMs, for instance, predict the existence of no fewer than 64 N^* and 22 Δ^* states with masses less than 3 GeV. The "missing-states" problem [4] is obvious from these numbers. To complete $SU(3)_F$ multiplets, one needs no fewer than 17 Λ^*s, 41 Σ^*s, 41 Ξ^*s, and 24 Ω^*s.

If these "missing resonances" exist, they have either eluded detection or have produced only weak signals in the existing data sets. The search for those resonances provides a most natural motivation for future measurements at Jefferson Lab. As stated in the *2015 Long Range Plan for Nuclear Science* [1]: *For many years, there were both theoretical and experimental reasons to believe that the strange sea-quarks might play a significant role in the nucleon's structure; a better understanding of the role of strange quarks became an important priority.*

The JLab 12 GeV energy upgrade, with the new Hall D, provides an ideal tool for extensive studies of both non-strange and, specifically, strange baryon resonances [5, 6]. Our plan is to take advantage of the existing high-quality photon beamline and the experimental area in the Hall D complex at Jefferson Lab to deliver a beam of K_L particles onto a LH_2/LD_2 within the GlueX detector.

The recently constructed GlueX detector is a large-acceptance spectrometer with good coverage for both charged and neutral particles that can be adapted to this purpose. Obviously, a K_L beam facility with good momentum resolution is crucial for providing the data needed to identify and characterize the properties of hyperon resonances. The masses and widths of the lowest Λ and Σ baryons were determined mainly with kaon beam experiments in the 1970s [2]. The first determinations of the pole position in the complex-energy plane for a hyperon, for instance, for the $\Lambda(1520)3/2^-$, have been made only recently [7]. An intense K_L beam would open a new window of opportunity, not only to locate "missing resonances", but also to establish their properties by studying different decay channels systematically.

A recent white paper, dedicated to the physics with meson beams and endorsed by a broad physics community, summarized unresolved issues in hadron physics, and outlined the vast opportuni-

ties and advances that only become possible with a "secondary beam facility" [8]. The Hall D GlueX K-long Facility (KLF) measurements will allow studies of very poorly known multiplets of Λ^*, Σ^*, Ξ^*, and even Ω^* hyperons with unprecedented statistical precision. These measurements also have the potential to observe dozens of predicted (but heretofore unobserved) states and to establish the quantum numbers of already observed hyperon resonances listed in PDG2016 [2]. Interesting puzzles exist for PDG-listed excited hyperons that do not fit into any of the low-lying excited multiplets, and these need to be further revisited and investigated. Excited Ξs, for instance, are very poorly known. Establishing and discovering new states is important, in particular, for determination of the multiplet structure of excited baryons.

We have organized four Workshops: *Physics with Neutral Kaon Beam at JLab* (KL2016) (February 2016) [9], *Excited Hyperons in QCD Thermodynamics at Freeze-Out* (YSTAR2016) (November 2016) [10], *New Opportunities with High-Intensity Photon Sources* (HIPS2017) (February 2017) [11], and *Pion-Kaon Interactions* (PKI2018) (February 2018) [12]. They were dedicated to the physics of hyperons produced by the neutral kaon beam. The KL2016 Workshop [13] followed our LoI–12–15–001 [14] to help address the comments made by PAC43 and to prepare the full proposal for PAC45 [15]. The proposed GlueX KLF program is complementary, for instance, to the CLAS12 baryon spectroscopy experiments [16, 17] and would operate at Hall D for several years. The YSTAR2016 Workshop [18] was a successor to the recent KL2016 Workshop and considered the influence of possible "missing" hyperon resonances on QCD thermodynamics, on freeze-out in heavy ion collisions and in the early universe, and in spectroscopy. Then, the HIPS2017 Workshop [19] aimed at producing an optimized photon source concept with potential increase of scientific output at Jefferson Lab, and at refining the science for hadron physics experiments benefitting from such a high-intensity photon source. Finally, the PKI2018 Workshop is dedicated to the physics of strange mesons produced by the neutral kaon beam [20].

Additionally, the proposed facility will also have great impact in the strange meson sector by measurements of the final-state $K\pi$ system from threshold up to 2 GeV in invariant mass to establish and improve on pole positions and widths of all $K^*(K\pi)$ P-wave states and the S-wave scalar mesons $K_0^*(800)$ or $\kappa(800)$. In particular, the $\kappa(800)$ meson has been under discussion for decades and still remains to be unequivocally confirmed with corresponding quantum numbers by detailed phase-shift analysis with high statistics data [21]. A detailed study of the $K\pi$ system is required to extract the so-called $K\pi$ vector and scalar form factors that are to be compared with $\tau \to K\pi\nu_\tau$ decay and can be used to constrain the V_{us} Cabibbo-Kobayashi-Maskawa (CKM) matrix element as well as to be used in testing CP violation in decays of heavy B and D mesons into $K\pi\pi$ final states.

The proposal is organized in the following manner. We give an executive summary in Sec. 1 and the scope of the proposal in Sec 2. Then the case of hyperon spectroscopy is given in Sec. 3 while hyperons in lattice studies are presented in Sec. 4. An overview of the interest of the RHICH/LHC community in hyperon measurements is summarized in Sec. 5. The short overview of previous bubble chamber measurements is given in Sec. 6. Partial-wave phenomenology is considered in Sec. 7 and theory for the "neutron" target in Sec. 8. A short overview for strange meson spectroscopy is given in Sec. 9. Our proposed measurements are reported in Sec. 10. It describes a compact photon source, K_L production and K_L beam properties, start counter resolution, measurements of K_L flux, and cryogenic target description. Running conditions are described in Sec. 11.

Sec. 12 contains the cover letter for the KLF proposal submission. The Appendices contain many technical details for our proposal: Analysis of three-body final states in Appendix A1 13, determination of pole positions in Appendix A2 14, statistics tools for spectroscopy of strange resonances in Appendix A3 15, neutron and gamma background in Appendix A4 16, details of Monte Carlo study in Appendix A5 17, current hadronic projects in Appendix A6 18, additional physics potential with a K_L Beam Appendix in A7 19, and list of new equipment and of changes in existing setup required in Appendix A8 20.

3 The Case for Strange Hyperon Spectroscopy

The present experimental knowledge of the spectra of the strange hyperons remains remarkably incomplete, despite the fact that the ground states of the strange hyperons have been known since the 1960s. In the case of the Λ hyperon resonance spectrum, only the lowest negative-parity doublet and the positive parity singlet are well established, even though the structure of these resonances remains under discussion. In the case of the Σ and Ξ hyperons, only the lowest decuplet resonance states $\Sigma(1385)$ and $\Xi(1530)$ are well established.

The masses of the lowest positive-parity resonances in the spectrum of the Λ and Σ hyperons, the $\Lambda(1600)$ and $\Sigma(1660)$ are experimentally known, but their structure is not. In the case of the Ξ hyperon, the lowest positive-parity resonance remains unobserved.

To settle the nature of the hyperon resonances, their main decay modes have to be determined by experiment. A clear example of how the decay modes can settle the structure of the resonances is provided by the π-decay widths of the decuplets $\Delta(1232)$, $\Sigma(1385)$, and $\Xi(1530)$. The ratio of these decay widths is 13:4:1, whereas if they were simple three-quark states, with 3, 2, and 1 light quarks each, the ratio should be 9:4:1. A comparison of these ratios indicates that the $\Sigma(1385)$ and $\Xi(1530)$ appear to be three-quark states, while the $\Delta(1232)$ is more complex and formed by a three-quark core with a surrounding meson (or multiquark) cloud. This conclusion is well supported by extensive theoretical calculations [22, 23].

3.1 Heavy Quark Symmetry and the Hyperons

Heavy quark symmetry [24] provides a powerful tool for analyzing the structure of hyperons with heavy flavor quarks to those with strange quarks. Heavy quark symmetry follows from the fact that the strength of quark spin couplings scale with the inverse of the constituent mass. In the case of the hyperons this implies that the spin-orbit splittings in the hyperon spectra decrease with increasing quark mass. In the case of hyperons with light and heavy quarks this implies that the heavy quark spin decouples from those of the light quarks. Heavy quark symmetry suggests, that the ratio of the sizes of such spin-orbit splittings in the corresponding multiplets in the spectra of the strange, charm and beauty hyperons should approximately correspond to the ratio of the inverses of the corresponding constituent quark (or approximately) meson (K, D, B) masses: 10.7:2.8:1. Where the spin-orbit splittings conform to this scaling law the implication is that the structure of the corresponding hyperon resonances in the different flavor sectors are very similar, and where not,

their structures are anomalous and more complex.

This tool will be the more accurate, the heavier the constituent masses and for those hyperons, which do not contain light-flavor quarks. Given this it shall be exceptionally interesting compare the spin-orbit splittings between the Cascade hyperons in the different flavor sectors, once these are determined experimentally. Hitherto the comparable splittings are only known for the lowest negative parity doublets in the strange, charm and beauty hyperon spectra, with two light-flavor and only one single heavy quark, however. This argument is strongest in the case of the resonance spectrum of the Ξ and Ω hyperons, once better known, and when corresponding resonances can be detected for the corresponding charm and beauty hyperons.

In the case of those lowest energy flavor-singlet $1/2^-$ – $3/2^-$ parity doublets in the strange, charm and bottom hyperon spectra: $\Lambda(1405)$–$\Lambda(1520)$, $\Lambda_c(2595)$–$\Lambda_c(2625)$, $\Xi_c(2790)$–$\Xi_c(2815)$, and $\Lambda_b(5912)$–$\Lambda_b(5920)$ [2] the ratio between the splittings in these three doublets are 14.4:3.7:3.1:1. These ratios agree qualitatively and within 30% with the corresponding inverse ratios of the K, D, and B meson masses: 10.7:2.8:1. As these resonances all contain one light quark pair the latter is what one should expect from the gradual approach to heavy-quark symmetry with increasing meson (or constituent quark) mass if the quark structure of these three multiplets is similar. This pattern is also consistent with the large N_C limit of QCD.

The determination of the energies and quantum numbers of the $S = -2$ Cascade resonances beyond the $\Xi(1530)$ should have high priority, especially when the LHC_b experiment at CERN [25] may be expected do similar determination for double charm resonances. This is *a fortiori* the case for the spectrum of the Ω hyperons.

3.2 The $\Lambda(1405)1/2^- - \Lambda(1520)3/2^-$ Doublet

In the simplest constituent quark model, the most natural − and the oldest − interpretation, is that the $\Lambda(1405)1/2^- - \Lambda(1520)3/2^-$ doublet is a low-lying flavor singlet of three quarks (*uds*). Dynamical versions of this model, with two-body interactions between the quarks can describe the low mean energy of this multiplet, but not the 115 MeV splitting between them. This has led to suggestions that there may even be two different 1/2$^-$ states − one dynamical low $\overline{K}N$ resonance at 1405 MeV, and an unresolved higher state close to 1520 MeV [26]. If so, it is high time that the "missing" 1/2$^-$ higher-energy state be empirically identified. This problem may indicate that the $\Lambda(1405)$ has a more complex multiquark structure. This issue is tested in modern theoretical approaches, including contraints from unitarity and chiral symmetry. A two pole structure of $\Lambda(1405)$ was indeed found in Ref. [27]. The narrow pole lies slightly below $\bar{K}N$ threshold, and is fixed by the scattering data rather well, see Ref. [28] for the comparison of different modern coupled-channel approaches. However, the position of the second pole is determined less precisely, and may lie much further below $\bar{K}N$ threshold and deeper in the complex plane. Recent photoproduction data on $\pi\Sigma$ by CLAS [29] may be used to reduce the theoretical ambiguity on this (second) pole of $\Lambda(1405)$ as demonstrated in Ref. [30]. Modern lattice QCD (LQCD) calculations also support the view that its structure is a $\overline{K}N$ state [31, 32]. In Skyrme's topological soliton model for the baryons, the low-lying $\Lambda(1405)$ state also appears naturally as a mainly 5-quark state [33, 34]. That model is consistent with QCD in the large color number (N_C) limit. Lattice

calculations based on the sequential Bayesian do however indicate that the multiplet may have a mainly 3-quark structure [35].

3.3 The Low-Lying Positive-Parity Resonances

In the spectra of the nucleon and the Λ and Σ hyperons, the lowest positive-parity resonances all lie below the lowest negative-parity multiplets except for the flavor singlet doublet $\Lambda(1405)1/2^- - \Lambda(1520)3/2^-$. This reversal of normal ordering cannot be achieved in the constituent quark model with purely color-spin-dependent quark interactions. These low-lying positive-parity resonances are the $N(1440)$, $\Lambda(1600)$, and the $\Sigma(1660)$ $1/2^+$ states. Their low masses do however appear naturally, if the interactions between the quarks are flavor dependent [36].

Present day LQCD calculations have not yet converged on whether these low-lying states can be described as having a mainly three-quark structure [35, 37]. This may reflect that there is a collective nature in the quark content of these resonances. As an example Skyrme's topological soliton model for the baryons, which represents one version of the large N_C limit of QCD, describes these low-lying states as collective vibrational states.

In the spectrum of the Ξ, the $\Xi(1690)$ may be such a $1/2^+$ state as well, although the quantum numbers of that state are yet to be determined.

In the corresponding decuplet spectra, a similar low-lying positive-parity state has so far only been definitely identified in the $\Delta(1232)$ spectrum: namely, the $\Delta(1600)3/2^+$. The $\Sigma(1840)3/2^+$ resonance very likely represents the corresponding positive-parity Σ^* state. It should be important to identify the corresponding $3/2^+$ state in the spectrum of the Ξ^*.

It is of course very probable that corresponding low-lying positive-parity states will be found in the spectra of the Λ_c and Λ_b hyperons, given the fact that they have low-lying negative-parity states akin to those of the Λ hyperon as described above. The experimental identification of those is an important task. Even if the still tentative resonance $\Lambda_c(2765)$ turns out to be a $1/2^+$ state, its energy appears to be too high for being the equivalent of the $\Lambda(1600)$ in the charm hyperonspectrum.

In the spectrum of the Σ_c, the decuplet state $\Sigma_c(2520)$ is well established. The tentative resonance $\Sigma_c(2800)$ may, should it turn out to be a $1/2^+$ state, correspond to the $\Sigma(1660)$ in the strange hyperon spectrum.

3.4 The Negative-Parity Hyperon Resonances

In the spectrum of the nucleon, two well-separated groups of negative-parity resonances appear above the $1/2^+$ state $N(1440)$. In the three-quark model, the symmetry of the lowest energy group is $[21]_{FS}[21]_F[21]_S$; i.e., it has mixed flavor (F) and spin (S) symmetry as well as mixed flavor-spin (FS) symmetry [36, 38]. This group consists of the $N(1535)1/2^-$ and the $N(1520)3/2^-$ resonances. There is a direct correspondence in the $\Lambda(1670)1/2^-$ and the $\Lambda(1690)3/2^-$ resonances. There is also a repeat of this group in the spectrum of the Σ hyperon in the two resonances $\Sigma(1620)1/2^-$ (tentative) and $\Sigma(1670)3/2^-$.

These spin $1/2^-$ and $3/2^-$ states in the spectrum of the nucleon have intriguing decay patterns. The $N(1535)$ resonance has a large (32-52%) decay branch to ηN, even though its energy lies very close to the ηN threshold. This pattern repeats in the case of the $\Lambda(1670)$, which also has a substantial (10-25%) decay branch to the corresponding $\eta\Lambda$ state, even though it lies even closer to the threshold for that decay. As the still uncertain $\Sigma(1620)1/2^-$ resonance is located almost exactly at the threshold for $\eta\Sigma$, there is naturally no signal for an $\eta\Sigma$ decay from it. The ratio of the η decay widths of the $N(1535)$ and the $\Lambda(1670)$ is about 6:1, which suggests that the η decay might involve a pair of quarks rather than a single constituent quark as in the π decay of the decuplet resonances.

In the spectrum of the Ξ hyperon, none of the hitherto determined negative-parity multiplets is complete. The state $\Xi(1820)3/2^-$ may be the analog in the Ξ spectrum of the states $N(1520)$, $\Lambda(1670)$, and $\Sigma(1670)$. It should be important to identify the lowest $1/2^-$ resonance in the Ξ spectrum. If that resonance lacks an η decay branch, it would demonstrate that the η decay of the $1/2^-$ resonances in the spectra of the nucleon, Λ and Σ involves two quarks.

It should also be important to determine whether the uncertain “bumps" referred to in the Particle Data Tables labelled $\Sigma(1480)$, $\Sigma(1560)$, and $\Xi(1620)$ represent true resonances.

About 120 MeV above the $1/2^- - 3/2^-$ pair of nucleon resonances $N(1535)$ and $N(1520)$, the nucleon spectrum has three negative-parity resonances close in energy to one another. This multiplet is formed of the $N(1650)1/2^-$, $N(1700)3/2^-$, and $N(1675)5/2^-$ resonances. In the three-quark model the symmetry configuration of these states are $[21]_{FS}[21]_F[21]_S$; i.e., their spin configuration is completely symmetric.

The analogs in the spectrum of the Λ of the first and last of these nucleon resonances are the $\Lambda(1800)1/2^-$ and the $\Lambda(1830)5/2^-$ resonances. This correspondence remains uncertain, however, because the missing $3/2^-$ state in this Λ resonance multiplet has not yet been identified.

A common feature of all the $1/2^-$ resonances in these multiplets is their substantial η decay branch.

Our present knowledge of the spectrum of the Ξ hyperons remains too incomplete to identify any member of the negative-parity multiplet with the symmetry structure $[21]_{FS}[21]_F[21]_S$.

3.5 Summary for the Case

This overview shows that the present empirical knowledge of the spectrum of the strange hyperons remains remarkably incomplete. As a consequence, the quark structure of even the lowest-energy resonances remains uncertain. Only an experimental determination of the lowest-energy positive- and negative-parity hyperon resonances and their decay branches would settle the main open issues.

In the spectrum of the Λ hyperon, there remains a question of the existence of a $1/2^-$ partner to the $\Lambda(1520)3/2^-$ resonance. In addition, it should be important to search for the missing $\Lambda 3/2^-$ resonance near 1700 MeV. Equally important would be the search for the apparently “missing" $3/2^-$ state near 1750 MeV in the spectrum of the Σ hyperon.

The present knowledge of the spectrum of the Σ hyperons remains too incomplete to identify any

member of the corresponding negative-parity multiplet formed of 1/2$^-$, 3/2$^-$, and 5/2$^-$ resonances.

It should also be important to determine, whether the uncertain "bumps" referred to in the Particle Data Tables labelled $\Sigma(1480)$, $\Sigma(1560)$, and $\Sigma(1620)$ represent true resonances [2].

Finally the determination of the spectrum of the strange cascade hyperon should be given high priority. This spectrum remains very poorly known. As these hyperon resonances contain only one light-flavor quark the scalings implied by heavy quark symmetry would provide a tool to predict the splittings in the corresponding spectra of the double charm and beauty hyperons.

3.6 Note on the Strange Meson Spectrum

As in the case of the strange hyperons, it is instructive to compare the spectrum of the kaons to the corresponding spectra of the D and the D_s mesons. With exception of the still uncertain spin 0 state κ or $K_0^*(800)$ the known parts of the kaon, the D and the D_s mesons are qualitatively very similar, but with somewhat different orderings [2].

The established part of spectrum of the kaon begins with the 0^- ground state, followed by the 1^- $K^*(892)$ vector meson meson state, which is followed by the two 1^+ states $K_1(1270)$, $K_1(1400)$, and then the recurrence $K^*(1410)$ of the 1^- vector meson state and the scalar meson state $K_0^*(1430)$. The spectrum of the D meson differs only in that the corresponding scalar meson state $D_0^*(2400)$ lies slighly below, rather than slightly above the two 1^+ states $D_1(2420)$ and $D_1(2430)$, and in that the analog of the second recurrence of the vector meson state in the D meson state has yet to be identified.

In the case of the charm-strange meson spectrum, the two 1^+ states $D_{s1}(2460)$ and $D_{s1}(2536)$ both lie above the scalar meson state $D_{s0}^*(2317)$, and the recurrence of the vector meson state $D_s^*(2112)$ also has yet to be found.

This comparison of the spectra of the K, D and D_s mesons reveals the key importance of settling the issue of the existence of the low lying scalar meson state κ or $K_0^*(800)$, as its existence would imply the existence of corresponding low lying scalar meson states in the spectra of the charm and charm-strange mesons. It is remarkable that in all these spectra, the first recurrence of that low scalar meson is well established by the states $K_0^*(1430)$, $D_0^*(2400)$, and $D_{s0}^*(2317)$. Given the very large width of the non-strange scalar meson $f_0(500)$ (or σ), it may be expected that the lowest scalar charm strange, charm and charm-strange mesons will have similar large widths, which would be the main reason for the absence of clear signals for their pole positions.

4 Strange Hadrons from the Lattice

Our knowledge of the excited-state spectrum of QCD through the solution of the theory on a Euclidean space-time lattice has undergone tremendous advances over the past several years. What we characterize as excited states are resonances that are unstable under the strong interaction, and their properties are encapsulated in momentum-dependent scattering amplitudes. The means of

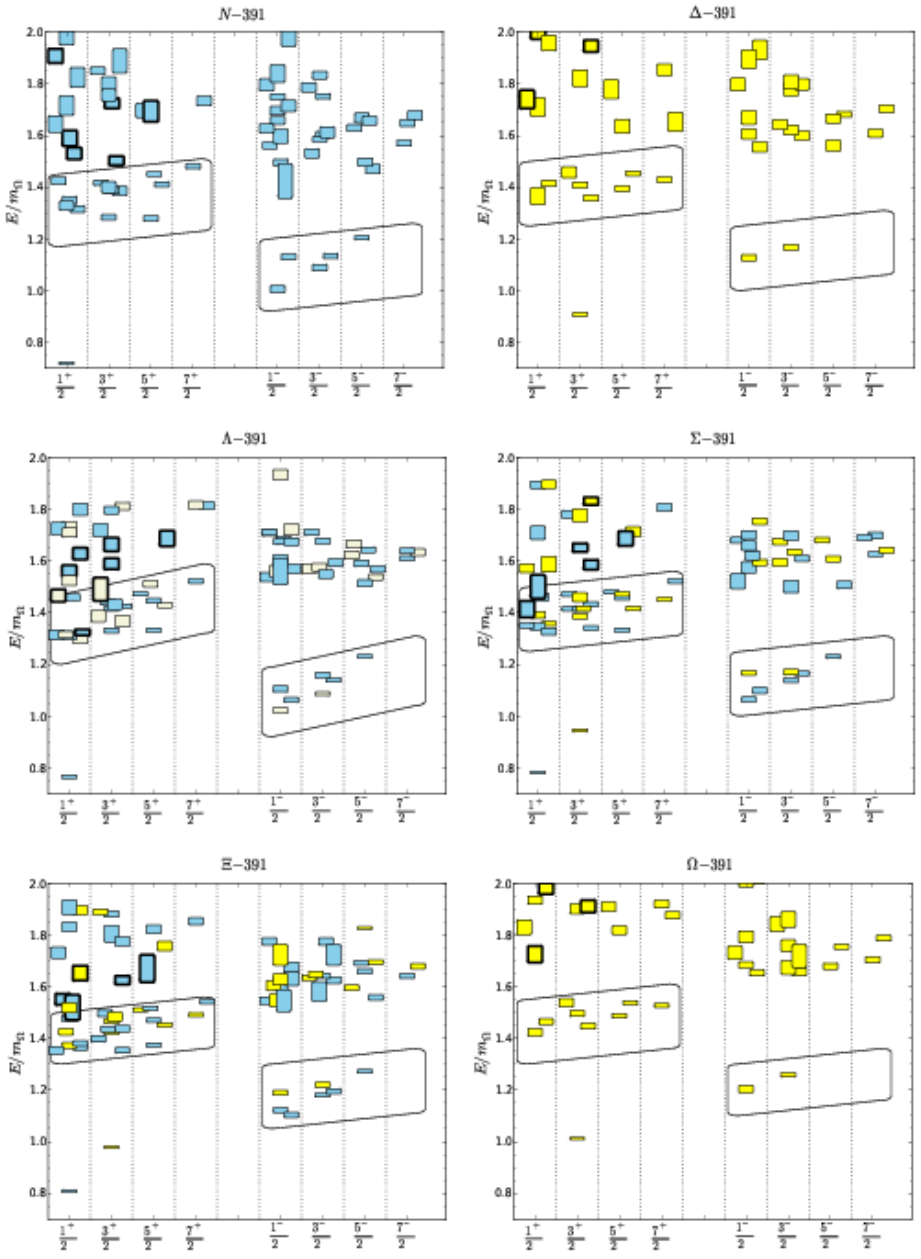

Figure 1: Results for baryon excited states using an ensemble with $m_\pi = 391$ MeV are shown versus J^P [61]. Colors are used to display the flavor symmetry of dominant operators as follows: blue for 8_F in N, Λ, Σ, and Ξ; beige for 1_F for Λ; yellow for 10_F in Δ, Σ, Ξ, and Ω. The lowest bands of positive- and negative-parity states are highlighted within slanted boxes. Hybrid states, in which the gluons play a substantive role, are shown for positive parity by symbols with thick borders.

calculating such momentum-dependent phase shifts for elastic scattering on a Euclidean lattice at finite volume was provided many years ago [39] and extended to systems in motion [40], but its implementation for QCD remained computationally elusive until recently. A combination of theoretical, algorithmic, and computational advances has changed this situation dramatically, notably in the case of mesons. There have been several lattice calculations of the momentum-dependent phase shift of the ρ mesons [41–47]. More recently, the formulation to extract amplitude information has been extended to the coupled-channel case [48–52], and applied to the case of the coupled $K\overline{K} - \pi\pi$ [53] system describing the ρ resonance to the $\eta K - \eta\pi$ system [54, 55], and recently to the emblematic isoscalar sector [56, 57].

The application to baryons is far more limited but, nonetheless, important insights have been gained. In an approach in which the excited-state hadrons are treated as stable particles, a spectrum of baryons at least as rich as that of the quark model is revealed [58, 59], and evidence has been presented for "hybrid" baryon states, beyond those of the quark model, in which gluon degrees of freedom are essential [60]. Notably, this picture extends to the spectrum of Λ, Σ, Ξ, and Ω states where the counting of states relects $SU(6) \times O(3)$ symmetry, and the presence of hybrids is common across the spectrum. As indicated above, these calculations are incomplete in that the momentum-dependent scattering amplitudes remain to be extracted. In Fig. 1, baryon spectra from [61] are presented in units of Ω mass from LQCD calculations with ensemble $m_\pi = 391$ MeV (not yet at physical m_π). However, in comparison with the case of mesons cited above, the challenges are more computational than theoretical or conceptual, and the progress made in the meson sector will be reflected for the case of baryons in the coming years.

5 The Interest of the RHIC/LHC Community in Excited Hyperon Measurements

The relativistic heavy-ion community at RHIC and the LHC has recently embarked on specific analyses to address the issue of strangeness hadronization. LQCD calculations in the QCD crossover transition region between a deconfined phase of quark and gluons and a hadronic resonance gas have revealed a potentially interesting sub-structure related to the hadronization process. Studies of flavor-dependent susceptibilities, which can be equated to experimental measurements of conserved quantum-number fluctuations, seem to indicate a slight flavor hierarchy in the three-quark sector (u,d,s) in thermalized systems. Specifically, the ratios of higher-order susceptibilities in the strange sector show a higher transition temperature than in the light sector [62]. Both pseudo-critical temperatures are still within the error bars of the quoted transition temperature based on all LQCD order parameters [63, 64], which is 154$\pm$9 MeV, but the difference of the specific susceptibilities is around 18 MeV and well outside their individual uncertainties.

This difference seems to be confirmed by statistical thermal-model calculations that try to describe the yields of emitted hadrons from a QGP based on a common chemical freeze-out temperature. Although the yields measured by ALICE at the LHC in 2.76 TeV PbPb collisions can be described by a common temperature of 156$\pm$2 MeV, with a reasonable χ^2, the fit improves markedly if one allows the light quark baryons to have a lower temperature than the strange quark baryons [65].

A similar result has been found when the thermal fluctuations of particle yields as measured by STAR Collaboration [66, 67], which can be related to the light quark dominated susceptibilities of the electric charge and the baryon number on the lattice, have been compared to statistical model calculations [68].

If one assumes that strange and light quarks indeed prefer different freeze-out temperatures, then the question arises how this could impact the hadronization mechanism and abundance of specific hadronic species. In other words, is the production of strange particles, in particular excited resonant states, enhanced in a particular temperature range in the crossover region? Strange ground-state particle production shows evidence of enhancement, but the most likely scenario is that the increased strange quark abundance will populate excited states; therefore, the emphasis of any future experimental program trying to understand hadron production is shifting towards strange baryonic resonance production. Furthermore, recent LHC measurements in small systems, down to elementary proton-proton collisions, have revealed that even in these small systems there is evidence for deconfinement, if the achieved energy density, documented by the measured charged particle multiplicity is large enough [69]. Therefore, future measurements of elementary collisions in the K-Long Facility experiment at JLab might well provide the necessary link to future analysis of strange resonance enhancements in heavy-ion collisions at RHIC and the LHC and a deeper understanding of the hadronization process.

This statement is also supported by comparisons between the aforementioned LQCD calculations and model predictions based on a non-interacting hadronic resonance gas. The Hadron Resonance Gas (HRG) model [70–73] yields a good description of most thermodynamic quantities in the hadronic phase up to the pseudo-critical temperature. The idea that strongly interacting matter in the ground state can be described in terms of a non-interacting gas of hadrons and resonances, which effectively mimics the interactions of hadrons by simply increasing the number of possible resonant states exponentially as a function of temperature, was proposed early on by Hagedorn [74]. The only input to the model is the hadronic spectrum: usually it includes all well-known hadrons in the *Review of Particle Physics* (RPP), namely the ones rated with at least two stars. Recently, it has been noticed that some more differential observables present a discrepancy between lattice and HRG model results. The inclusion of not-yet-detected states, such as the ones predicted by the original Quark Model (QM) [75, 76] has been proposed to improve the agreement [77, 78]. A systematic study based on a breakdown of contributions to the thermodynamic pressure given by particles grouped according to their quantum numbers (in particular baryon number and strangeness) enables us to infer in which hadron sector more states are needed compared to the well-known ones from the RPP [79]. In case of a flavor hierarchy in the transition region, one would expect the number of strange resonances to increase, due to a higher freeze-out temperature, compared to the number of light-quark resonances. Figure 2 shows the effect of different strange hadron input spectra to the HRG model in comparison to LQCD. Figure 2 (Upper plot) shows the number of states in PDG2016 [2], PDG2016+ (including one star states), the standard QM, and a Quark Model with enhanced quark interactions in the hadron (hyper-central model hQM [80]). Fig. 2 (Lower plot) shows a comparison of the HRG results to a leading-order LQCD calculation of μ_s/μ_B; i.e., the ratio to strange to baryon number susceptibility [79].

An interesting conclusion that arises from these studies is that the improvement in the listing of strange resonances between PDG2008 [81] and PDG2016 definitely brought the HRG calculations

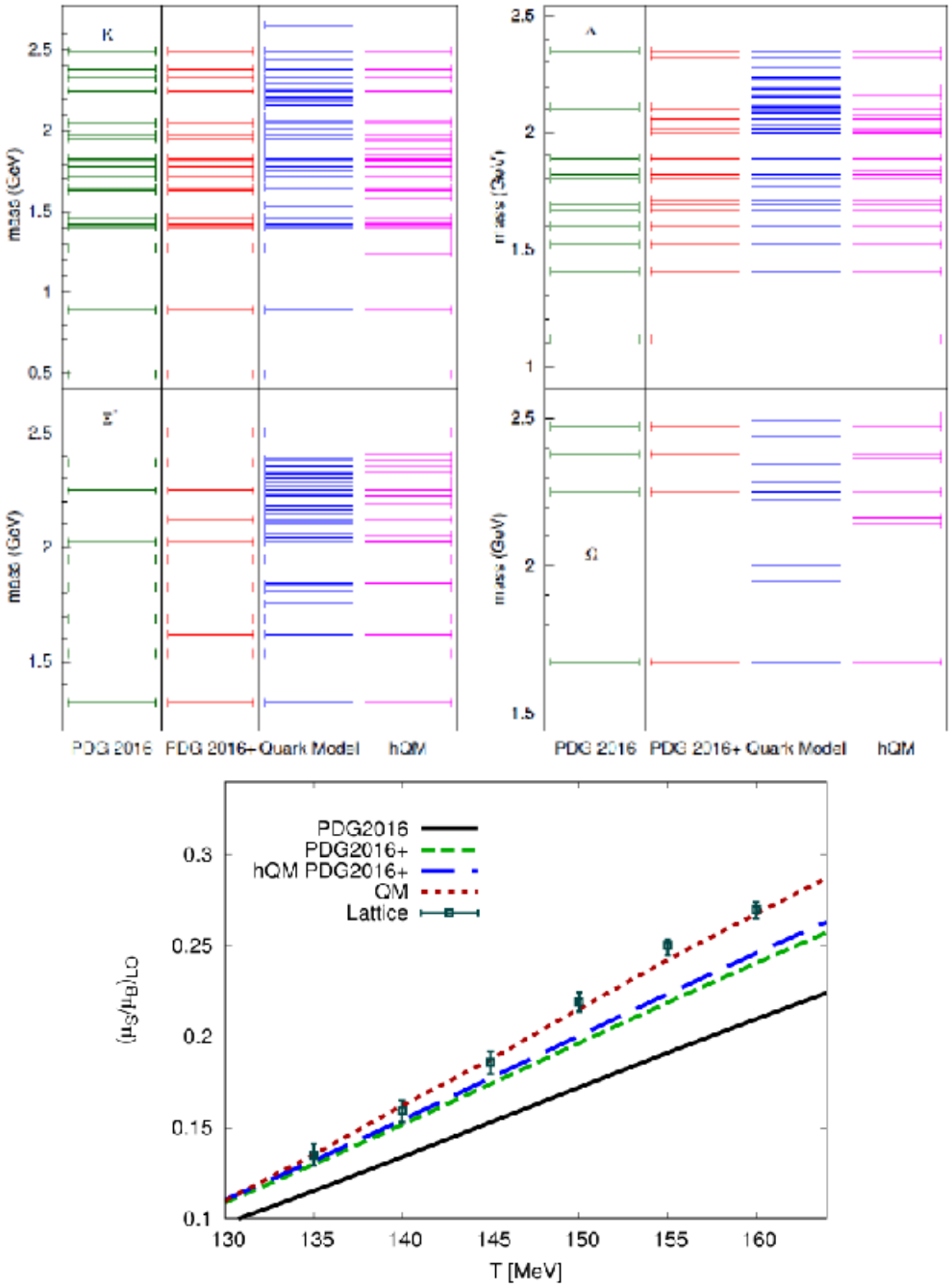

Figure 2: Upper plot: Comparison of predicted and measured excited strange hadronic states in PDG2016, PDG2016+ (including one star states), QM, and hQM. Lower plot: Lattice QCD calculation of the temperature dependence of the leading order susceptibility ratio (μ_s/μ_B) compared to results from HRG model calculations with varying number of hadronic states.

closer to the LQCD data. By looking at details in the remaining discrepancy, which is in part remedied by including one-star rated resonances in PDG2016, it seems that the effect is more carried by singly strange resonances rather than multi-strange resonances, also in light of comparisons to

quark models that include di-quark structures [82] or enhanced quark interactions in the baryon (hypercentral models [80]). This is good news for the experiments since the Λ and Σ resonances below 2 GeV/c^2 are well within reach of the KLF experiment and, to a lesser significance, the RHIC/LHC experiments. In this context it is also important to point out that the use of both hydrogen and deuterium targets in KLF is crucial since it will enable the measurement of charged and neutral hyperons. A complete spectrum of singly strange hyperon states is necessary to make a solid comparison to first-principle calculations.

In summary: Any comparisons between experimentally verified strange quark-model states from YSTAR and LQCD will shed light on a multitude of interesting questions relating to hadronization in the non-perturbative regime, exotic particle production, the interaction between quarks in baryons and a possible flavor hierarchy in the creation of confined matter.

6 Previous Measurements

While a formally complete experiment requires the measurement, at each energy, W, and angle, θ, of at least three independent observables, the current database for $K_Lp \rightarrow \pi Y$ and KY is populated mainly by unpolarized cross sections. Figure 3 illustrates this quite clearly.

The initial studies of the KLF program at GlueX will likely focus on two-body and quasi-two-body processes: elastic $K_Lp \rightarrow K_Sp$ and charge-exchange $K_Lp \rightarrow K^+n$ reactions, then two-body reactions producing $S = -1$ ($S = -2$) hyperons as $K_Lp \rightarrow \pi^+\Lambda$, $K_Lp \rightarrow \pi^+\Sigma^0$, and $K_Lp \rightarrow \pi^0\Sigma^+$ ($K_Lp \rightarrow K^+\Xi^0$). Most of the previous measurements induced by a K_L beam, were collected for $W = 1454$ MeV and with some data up to $W = 5054$ MeV. Experiments were performed between 1961 and 1982 with mostly hydrogen bubble chambers at ANL, BNL, CERN, DESY, KEK, LRL, NIMROD, NINA, PPA, and SLAC. Note that some of data were taken at EM facilities at NINA [84] (a short overview about NINA experiments is given by Albrow recently [85]) and SLAC [86]. The goal of the Manchester University group that worked at the Daresbury 5-GeV electron synchrotron NINA was CP-violation, which was a hot topic back to the mid 1960s. The main physics topics that the SLAC group addressed were studies of the systematics for particle/anti-particle processes through the intrinsic properties of the K-longs.

The first paper that discussed the possibility of creating a practical neutral kaon beam at an electron synchrotron through photoproduction was an optimistic prediction for SLAC by Drell and Jacob in 1965 [87]. With significant developments in technology, high-quality EM facilities, such as JLab [14], are now able to realize a complete hyperon spectroscopy program.

The overall systematics of previous K_Lp experiments varies between 15% and 35%, and the energy binning is much broader than hyperon widths. The previous number of K_L-induced measurements (2426 $d\sigma/d\Omega$, 348 σ^{tot}, and 115 P observables) [83] was very limited. Additionally, we are not aware of any measurements on a “neutron" target.

Our knowledge about the non-strange sector is more advanced vs. the strange one [2]. For the non-strange case, for instance, phenomenology has access to 51k data of $\pi N \rightarrow \pi N$ and 39k data of $\gamma N \rightarrow \pi N$ below $W = 2.5$ GeV [88].

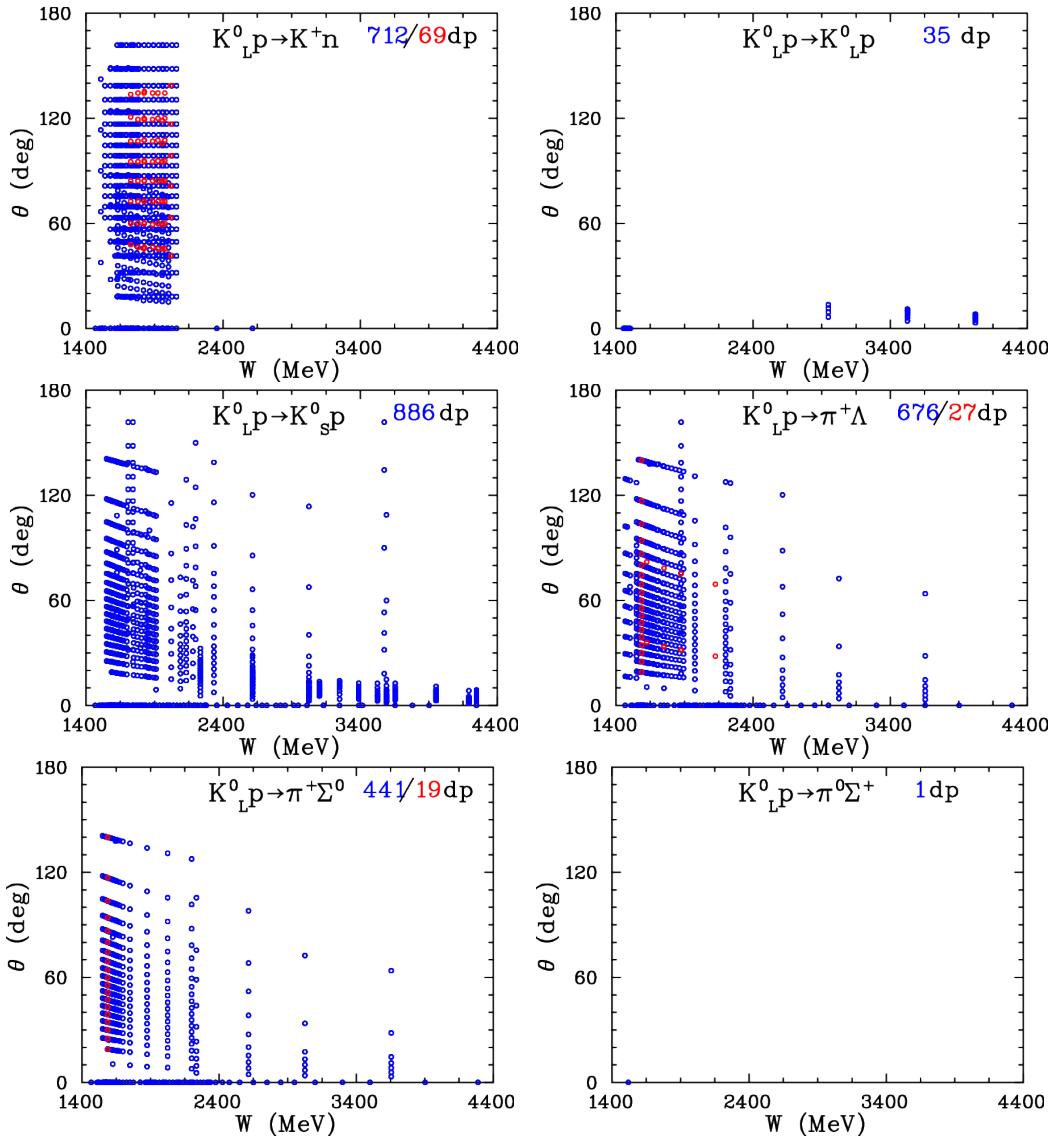

Figure 3: Experimental data available for $K_Lp \to K^+n$, $K_Lp \to K_Lp$, $K_Lp \to K_Sp$, $K_Lp \to \pi^+\Lambda$, $K_Lp \to \pi^+\Sigma^0$, and $K_Lp \to \pi^0\Sigma^+$ as a function of CM energy W [83]. The number of data points (dp) is given in the upper righthand side of each subplot [blue (red) shows the amount of unpolarized (polarized) observables]. Total cross sections are plotted at zero degrees.

7 Phenomenology / Partial-Wave Analysis

Here, we summarize some of the physics issues involved with such processes. Following Ref. [89], the differential cross section and polarization for K_Lp scattering are given by

$$\frac{d\sigma}{d\Omega} = \lambda\!\!\!^{-2}(|f|^2 + |g|^2), \tag{1}$$

$$P\frac{d\sigma}{d\Omega} = 2\lambda\!\!\!^{-2}\mathrm{Im}(fg^*), \tag{2}$$

where $\lambda\!\!\!^{-} = \hbar/k$, with k the magnitude of CM momentum for the incoming meson. Here $f = f(W,\theta)$ and $g = g(W,\theta)$ are the usual spin-nonflip and spin-flip amplitudes at CM energy W and meson CM scattering angle θ. In terms of partial waves, f and g can be expanded as

$$f(W,\theta) = \sum_{l=0}^{\infty}[(l+1)T_{l+} + lT_{l-}]P_l(\cos\theta), \tag{3}$$

$$g(W,\theta) = \sum_{l=1}^{\infty}[T_{l+} - T_{l-}]P_l^1(\cos\theta), \tag{4}$$

where l is the initial orbital angular momentum, $P_l(\cos\theta)$ is a Legendre polynomial, and $P_l^1(\cos\theta)$ is an associated Legendre function. The total angular momentum for the amplitude T_{l+} is $J = l+\frac{1}{2}$, while that for the amplitude T_{l-} is $J = l - \frac{1}{2}$. For hadronic scattering reactions, we may ignore small CP-violating terms and write

$$K_L = \frac{1}{\sqrt{2}}(K^0 - \overline{K^0}), \tag{5}$$

$$K_S = \frac{1}{\sqrt{2}}(K^0 + \overline{K^0}). \tag{6}$$

We may generally have both $I = 0$ and $I = 1$ amplitudes for KN and $\overline{K}N$ scattering, so that the amplitudes $T_{l\pm}$ can be expanded in terms of isospin amplitudes as

$$T_{l\pm} = C_0 T^0_{l\pm} + C_1 T^1_{l\pm}, \tag{7}$$

where $T^I_{l\pm}$ are partial-wave amplitudes with isospin I and total angular momentum $J = l \pm \frac{1}{2}$, with C_I the appropriate isospin Clebsch-Gordon coefficients.

We plan to do a coupled-channel PWA with new GlueX data in combination with available new J-PARC K^- measurements when they will come. Then the best fit will allow determine model-independent (data-driven) partial-wave amplitudes and associated resonance parameters (pole positions, residues, BW parameters, etc.) as the SAID group does, for instance, for the analysis of πN-elastic, charge-exchange, and $\pi^- p \to \eta n$ data [90].

7.1 KN and $\overline{K}N$ Final States

The amplitudes for reactions leading to KN and $\overline{K}N$ final states are

$$T(K^- p \to K^- p) = \frac{1}{2}T^1(\overline{K}N \to \overline{K}N) + \frac{1}{2}T^0(\overline{K}N \to \overline{K}N), \tag{8}$$

$$T(K^- p \to \overline{K^0} n) = \frac{1}{2}T^1(\overline{K}N \to \overline{K}N) - \frac{1}{2}T^0(\overline{K}N \to \overline{K}N), \tag{9}$$

$$T(K^+ p \to K^+ p) = T^1(KN \to KN), \tag{10}$$

$$T(K^+ n \to K^+ n) = \frac{1}{2}T^1(KN \to KN) + \frac{1}{2}T^0(KN \to KN), \tag{11}$$

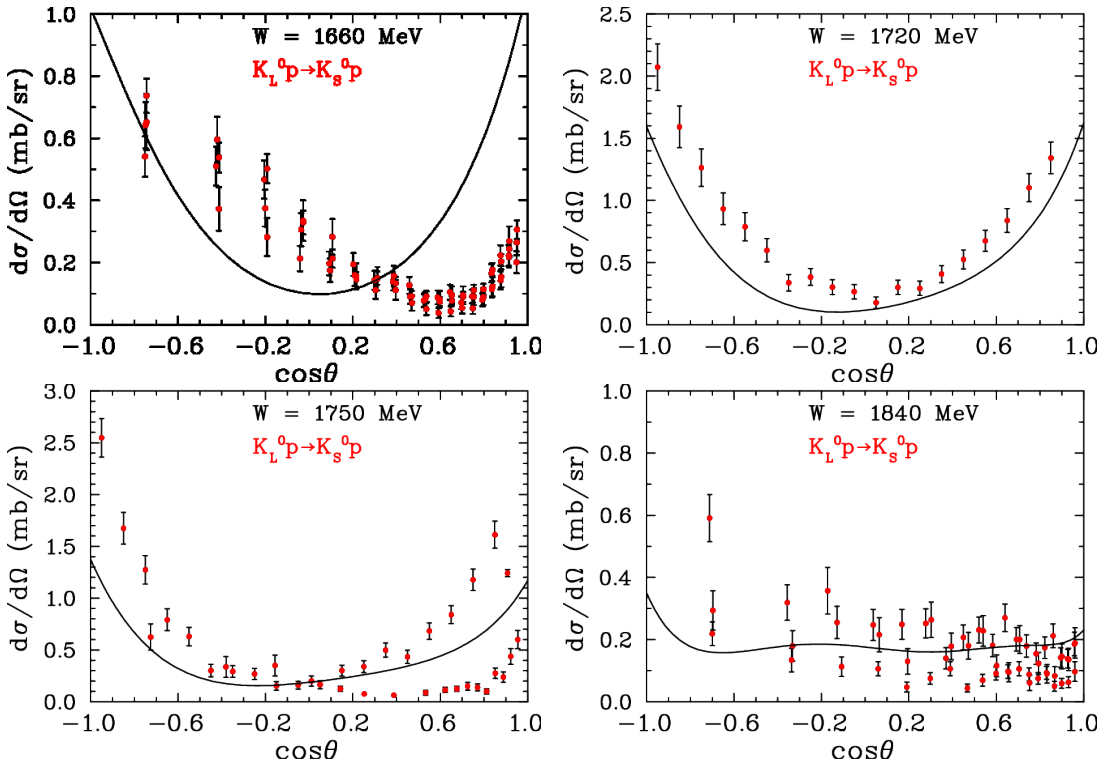

Figure 4: Selected differential cross section data for $K_L p \to K_S p$ at $W = 1660$ MeV, 1720 MeV, 1750 MeV, and 1840 MeV, from Ref. [91]. The plotted points from previously published experimental data are those data points within 20 MeV of the kaon CM energy indicated on each panel [88]. Plotted uncertainties are statistical only. The curves are predictions using amplitudes from a recent PWA of $\overline{K}N \to \overline{K}N$ data [92, 93], combined with $KN \to KN$ amplitudes from the SAID database [88].

$$T(K_L p \to K_S p) = \frac{1}{2}\left(\frac{1}{2}T^1(KN \to KN) + \frac{1}{2}T^0(KN \to KN)\right) - \frac{1}{2}T^1(\overline{K}N \to \overline{K}N), \quad (12)$$

$$T(K_L p \to K_L p) = \frac{1}{2}\left(\frac{1}{2}T^1(KN \to KN) + \frac{1}{2}T^0(KN \to KN)\right) + \frac{1}{2}T^1(\overline{K}N \to \overline{K}N), \quad (13)$$

$$T(K_L p \to K^+ n) = \frac{1}{\sqrt{2}}\left(\frac{1}{2}T^1(KN \to KN) - \frac{1}{2}T^0(KN \to KN)\right). \quad (14)$$

No differential cross-section data are available for $K_L p \to K_L p$ below $W \sim 2948$ MeV. A fair amount of data are available for the reaction, $K^+ n \to K^0 p$, measured on a deuterium target. Figure 4 shows a sample of available differential cross sections for $K_L p \to K_S p$ compared with predictions determined from a recent PWA of $\overline{K}N \to \overline{K}N$ data [92, 93], combined with $KN \to KN$ amplitudes from the SAID database [88]. The predictions at lower and higher energies tend to agree less well with the data.

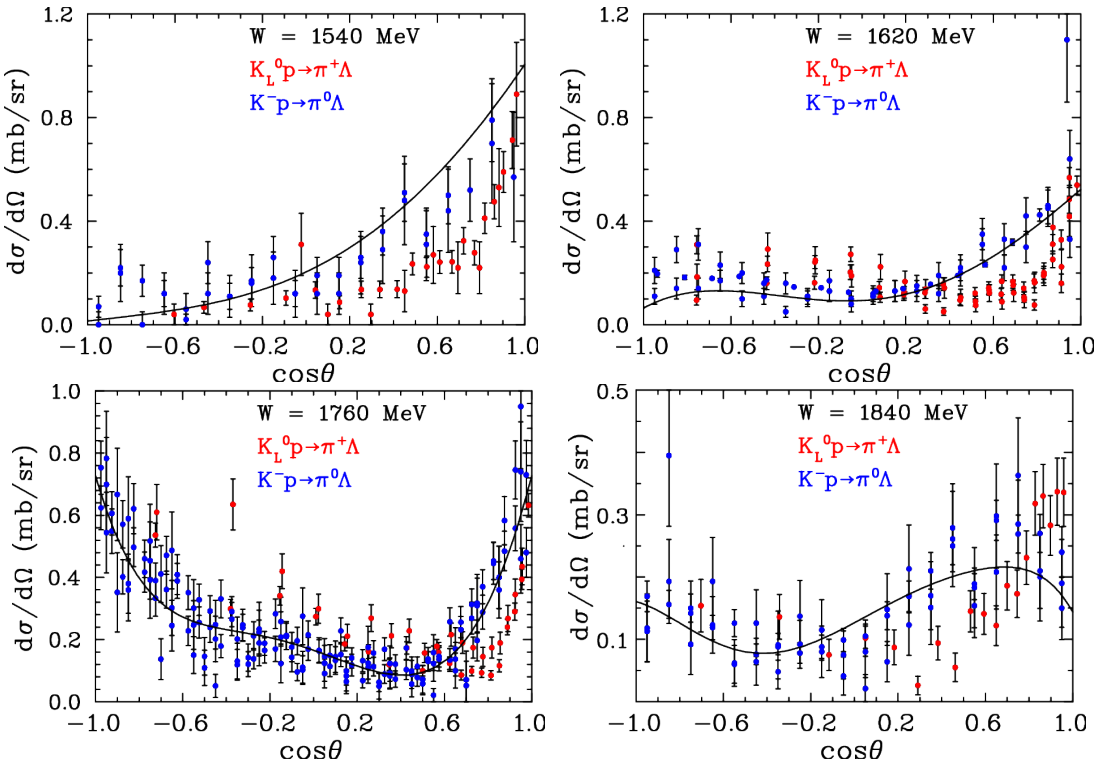

Figure 5: Comparison of selected differential cross section data for $K^- p \to \pi^0 \Lambda$ and $K_L p \to \pi^+ \Lambda$ at $W = 1540$ MeV, 1620 MeV, 1760 MeV, and 1840 MeV, from Ref. [91]. The plotted points from previously published experimental data are those data points within 20 MeV of the kaon CM energy indicated on each panel [88]. Plotted uncertainties are statistical only. The curves are from a recent PWA of $K^- p \to \pi^0 \Lambda$ data [92, 93].

7.2 $\pi\Lambda$ Final States

The amplitudes for reactions leading to $\pi\Lambda$ final states are

$$T(K^- p \to \pi^0 \Lambda) = \frac{1}{\sqrt{2}} T^1(\overline{K}N \to \pi\Lambda), \tag{15}$$

$$T(K_L p \to \pi^+ \Lambda) = -\frac{1}{\sqrt{2}} T^1(\overline{K}N \to \pi\Lambda). \tag{16}$$

The $K^- p \to \pi^0 \Lambda$ and $K_L p \to \pi^+ \Lambda$ amplitudes imply that observables for these reactions measured at the same energy should be the same except for small differences due to the isospin-violating mass differences in the hadrons. No differential cross-section data for $K^- p \to \pi^0 \Lambda$ are available at CM energies $W < 1540$ MeV, although data for $K_L p \to \pi^+ \Lambda$ are available at such energies. At 1540 MeV and higher energies, differential cross-section and polarization data for the two reactions are in fair agreement, as shown in Figs. 5 and 6. It should be stressed that polarized measurements are tolerable for any PWA solutions (Fig. 6).

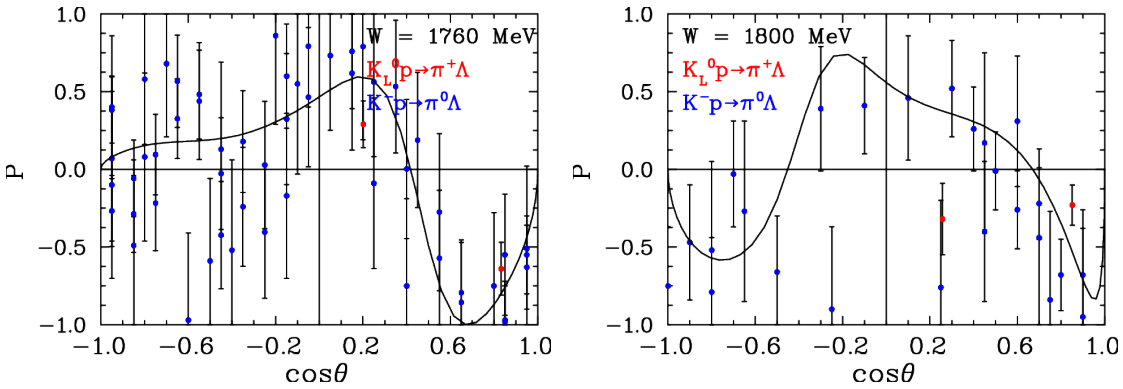

Figure 6: Comparison of selected polarization data for $K^- p \to \pi^0 \Lambda$ and $K_L p \to \pi^+ \Lambda$ at $W = 1760$ MeV and 1880 MeV, from Ref. [91]. The plotted points from previously published experimental data are those data points within 20 MeV of the kaon CM energy indicated on each panel [88]. The curves are from a recent PWA of $K^- p \to \pi^0 \Lambda$ data [92, 93].

7.3 $\pi\Sigma$ Final States

The amplitudes for reactions leading to $\pi\Sigma$ final states are

$$T(K^- p \to \pi^- \Sigma^+) = -\frac{1}{2} T^1(\overline{K}N \to \pi\Sigma) - \frac{1}{\sqrt{6}} T^0(\overline{K}N \to \pi\Sigma), \quad (17)$$

$$T(K^- p \to \pi^+ \Sigma^-) = \frac{1}{2} T^1(\overline{K}N \to \pi\Sigma) - \frac{1}{\sqrt{6}} T^0(\overline{K}N \to \pi\Sigma), \quad (18)$$

$$T(K^- p \to \pi^0 \Sigma^0) = \frac{1}{\sqrt{6}} T^0(\overline{K}N \to \pi\Sigma), \quad (19)$$

$$T(K_L^0 p \to \pi^+ \Sigma^0) = -\frac{1}{2} T^1(\overline{K}N \to \pi\Sigma), \quad (20)$$

$$T(K_L^0 p \to \pi^0 \Sigma^+) = \frac{1}{2} T^1(\overline{K}N \to \pi\Sigma). \quad (21)$$

Figure 7 shows a comparison of differential cross-section data for $K^- p$ and $K_L p$ reactions leading to $\pi\Sigma$ final states at $W = 1660$ MeV (or $P_{\rm lab} = 716$ MeV/c). The curves are based on energy-dependent isospin amplitudes from a recent PWA [92, 93]. No differential cross-section data are available for $K_L p \to \pi^0 \Sigma^+$. As this example shows, the quality of the $K_L p$ data is comparable to that for the $K^- p$ data. It would, therefore, be advantageous to combine the $K_L p$ data in a new coupled-channel PWA with available $K^- p$ data. Note that the reactions $K_L p \to \pi^+ \Sigma^0$ and $K_L p \to \pi^0 \Sigma^+$ are isospin selective (only $I = 1$ amplitudes are involved) whereas the reactions $K^- p \to \pi^- \Sigma^+$ and $K^- p \to \pi^+ \Sigma^-$ are not. New measurements with a K_L beam would lead to a better understanding of Σ^* states and would help constrain the amplitudes for $K^- p$ scattering to $\pi\Sigma$ final states

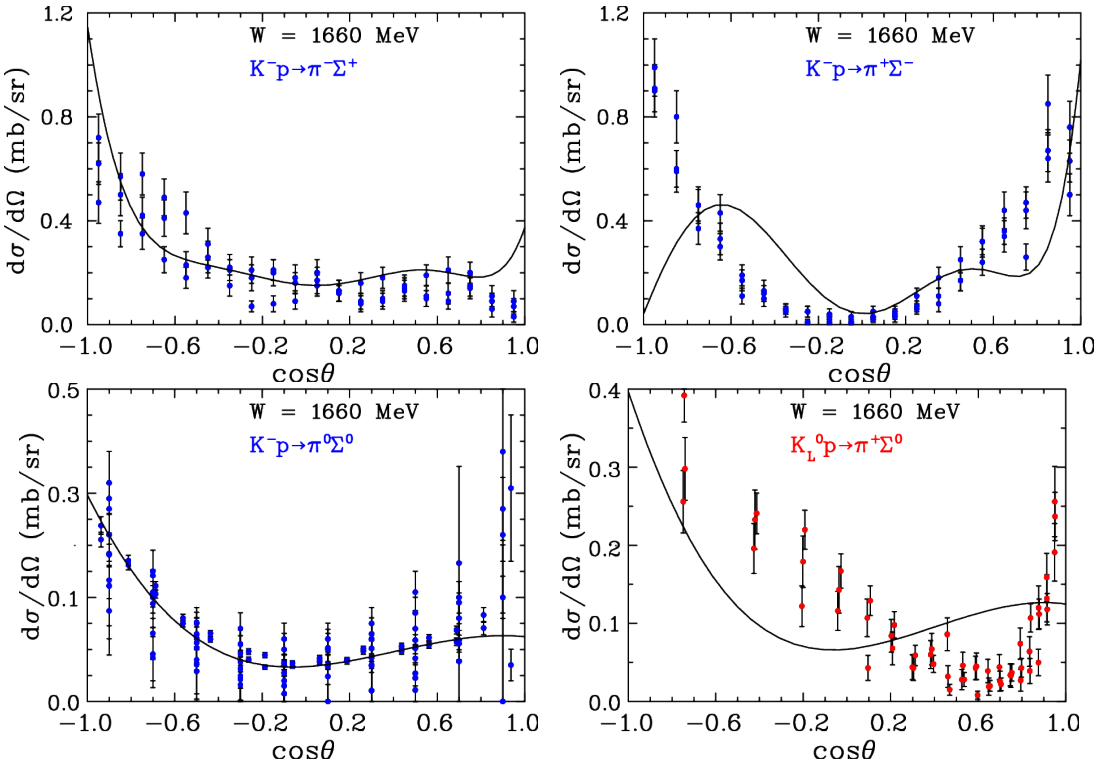

Figure 7: Comparison of selected differential cross-section data for $K^- p \to \pi^- \Sigma^+$, $K^- p \to \pi^+ \Sigma^-$, $K^- p \to \pi^0 \Sigma^0$, and $K_L p \to \pi^0 \Sigma^+$ at $W = 1660$ MeV, from Ref. [91]. The plotted points from previously published experimental data are those data points within 20 MeV of the kaon CM energy indicated on each panel [88] The curves are from a recent PWA of $K^- p \to \pi\Sigma$ data [92, 93].

7.4 $K\Xi$ Final States

The amplitudes for reactions leading to $K\Xi$ final states are

$$T(K^-p \to K^0\Xi^0) = \frac{1}{2}T^1(\overline{K}N \to K\Xi) + \frac{1}{2}T^0(\overline{K}N \to K\Xi), \quad (22)$$

$$T(K^-p \to K^+\Xi^-) = \frac{1}{2}T^1(\overline{K}N \to K\Xi) - \frac{1}{2}T^0(\overline{K}N \to K\Xi), \quad (23)$$

$$T(K_Lp \to K^+\Xi^0) = -\frac{1}{\sqrt{2}}T^1(\overline{K}N \to K\Xi). \quad (24)$$

The threshold for K^-p and K_Lp reactions leading to $K\Xi$ final states is fairly high ($W_{\rm thresh} = 1816$ MeV). In Fig. 8 (left), we present the cross section for Ξ production using a K^--beam [94]. There are no differential cross-section data available for $K_Lp \to K^+\Xi^0$ and very few (none recent) for $K^-p \to K^0\Xi^0$ or $K^-p \to K^+\Xi^-$. Measurements for these reactions would be very helpful, especially for comparing with predictions from dynamical coupled-channel (DCC) models [95,96] and other effective Lagrangian approaches [97]. The *Review of Particle Physics* [2] lists only two states with branching fractions (BF) to $K\Xi$, namely, $\Lambda(2100)7/2^-$ (BF $< 3\%$) and $\Sigma(2030)7/2^+$ (BF $< 2\%$)

7.5 Excited $S = -2$ and $S = -3$ baryons

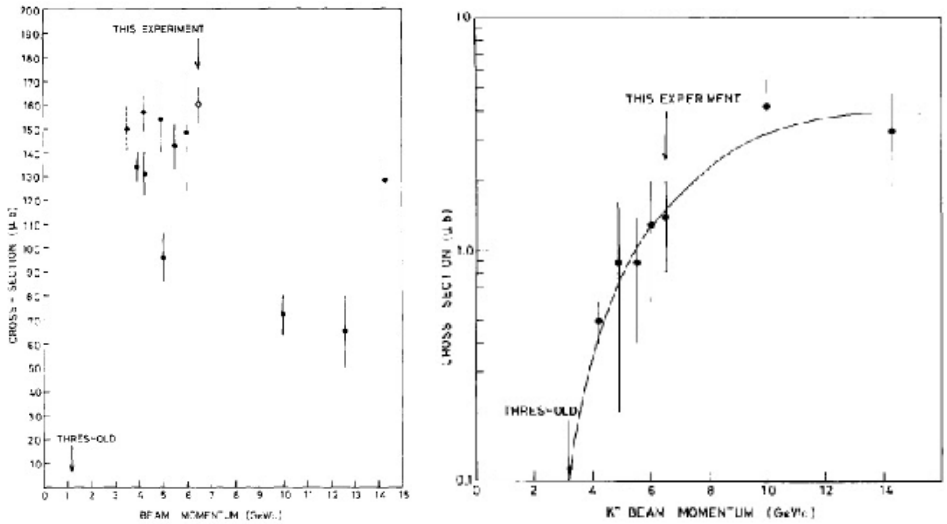

Figure 8: Left panel: Cross section of Ξ^- production, $K^-p \to \Xi^-X$, as a function of K^- momentum [94]. Right panel: Cross section of Ω^- production, $K^-p \to \Omega^-K^+K^0$, as a function of K^--momentum [94]. The curve is a fit by eye to the data.

.

$SU(3)$ flavor symmetry allows as many $S = -2$ baryon resonances as there are N and Δ resonances combined ($\sim$ 27); however, until now only three states, $\Xi(1322)1/2^+$, $\Xi(1530)3/2^+$, and $\Xi(1820)3/2^-$, have their quantum numbers assigned and only a few more states have been

observed [2]. For the discovery of excited cascade baryons, we envision a PWA similar to the $S = -1$ sector but more complicated as one is dealing with a three-body final state. See also Appendix A1 (Sec. 13) for a related discussion.

The experimental situation with Ω^{-*}s is even worse than for the Ξ^* case – there are very few data for excited states. The main reason for such a scarce dataset is the very low cross section for their indirect production with pion or photon beams. In Fig. 8 (right), we present the cross section for Ω production using a K^- beam [94].

A major effort in LQCD calculations involves the determination of inelastic and multi-hadron scattering amplitudes, and the first calculation to study an inelastic channel was recently performed [54, 55]. For lattice calculations involving baryons that contain one or more strange quarks an advantage is that the number of open decay channels is generally smaller than for baryons comprised only of the light u and d quarks.

7.6 Summary for PWA

Pole positions have been determined (no uncertainties) for several Λ^*s and Σ^*s but information about pole positions has not been determined for Ξ or Ω hyperons [2]. Our plan is to do a coupled-channel PWA with new GlueX KLF data in combination with available and new J-PARC K^-p measurements when they will be available. Then the best fit will allow the determination of data-driven (model independent) partial-wave amplitudes and associated resonance parameters (pole positions, residues, BW parameters, and so on. See Appendix A2 (Sec. 14) for a more detailed discussion. In Appendix A3 (Sec. 15), statistical tools for the reliable determination of the resonance spectrum are highlighted. Additionally, PWAs with new GlueX data will allow a search for "missing" hyperons via looking for new poles in complex plane positions. It will provide a new benchmark for comparisons with QCD-inspired models and LQCD calculations.

8 Theory for "Neutron" Target Measurements

The only systematic ways to address hadronic interactions at low energies are Chiral Perturbation Theory (ChPT) and numerical calculations of Lattice QCD. The first one is an Effective Theory to QCD at low energies, which relies on the expansion of QCD Green's functions in small momenta and quark masses. Over the years this approach has become a benchmark for a large variety of examples of hadronic systems. However, in the perturbative sense ChPT breaks down in the resonance region, and also exhibits slow convergence in three-flavor formulation or when large momenta are involved. In fact, all these obstacles are present in the antikaon-nucleon system, due to the large kaon mass, widely separated two particle thresholds and the presence of the $\Lambda(1405)1/2^-$. An extension of ChPT is required to address these issues namely the so-called coupled-channel Chiral Unitary approaches (UChPT).

These models implement unitarity exactly via a re-summation of a chiral potential to a certain chiral order. They successfully describe all available antikaon-nucleon scattering data and predict

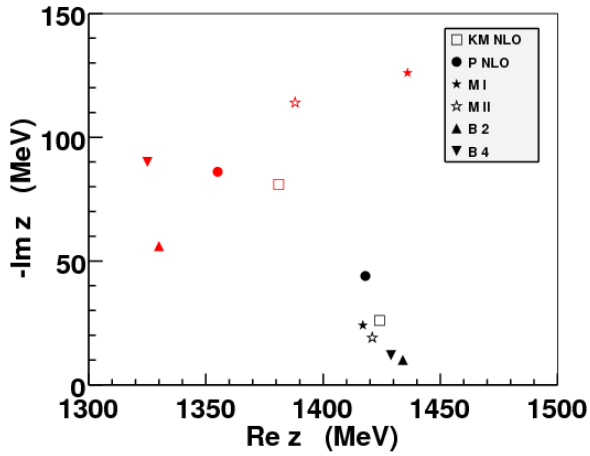

Figure 9: Pole positions for chiral unitary approaches - KM from Ref. [98], B from Ref. [30], M from Ref. [99], and P from Ref. [100] as compared in Ref. [28]. Each symbol represents the position of the first (black) and second (red) pole in each model.

the mass and width of the sub-threshold resonance in the Isospin $I = 0$ channel, the $\Lambda(1405)1/2^-$. Furthermore, such models lead to the prediction of the second pole in the complex energy plane with the same quantum numbers as $\Lambda(1405)1/2^-$. This is usually referred to as the two-pole structure of the $\Lambda(1405)$, see the current review by the Particle Data Group [2] for more details.

In the most advanced and recent formulation, the UChPT approach relies on a chiral amplitude for meson-baryon scattering up to next-to-leading chiral order. Whereas the unitarity constraint is imposed via the Bethe-Salpeter equation either in the full off-shell formulation [101, 102] or in the so-called on-shell approximation, e.g., [30, 98]. For the analysis of data the former is quite intricate, while as it was shown in Ref. [101] the off-shell effects are rather small. Recently, a direct quantitative comparison of the on-shell models [30, 98–100] was performed in Ref. [28]. It was found there that various models, which typically have many free parameters, adjusted to the same experimental data, predict very different behavior of the scattering amplitude on and off the real energy-axis. This systematic uncertainty becomes evident, when comparing the pole positions of the $\Lambda(1405)$ in these models (see Fig. 9). The position of the narrow (first) pole seems to be constraint at least in the real part rather well, while the predictions for the position broad (second) pole cover a very wide region of the complex energy-plane. This uncertainty is present even within models of the same type. This ambiguity can be traced back to the fact that the experimental data used to fix the parameters of the models is rather old and imprecise.

The K_L beam can be scattered on a neutron target, while measuring the strangeness $S = -1$ final meson-baryon states, see, e.g., Sec. 7. In such a setup, the proposed experiment will become a new and very strongly desired source of experimental data to pinpoint the properties of the antikaon-nucleon scattering amplitude. To make this statement more quantitative, we compare predictions of both solutions of the model [1] from Ref. [30]. These solutions agree with all presently

[1]The choice of this model for the present analysis is justified by the fact that it includes the p-wave interaction in the interaction-kernel of the Bethe-Salpeter equation explicitly.

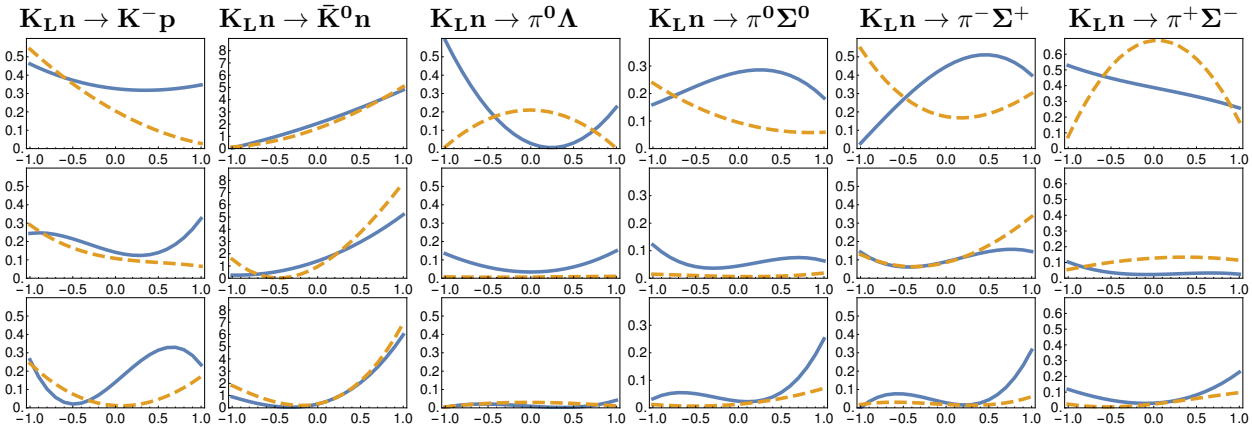

Figure 10: Theoretical predictions for differential cross sections, $d\sigma/d\Omega$ in mb as a function of CM cos of production angle. Each row associated with kaon lab-momentum of 300, 700, 1000 MeV/c of initial neutral kaon beam. Orange (dashed) and blue lines show predictions within Model-B2 and Model-B4, respectively (see text for details).

available scattering, threshold as well as the photoproduction data for the $\Sigma\pi$ line shapes by the CLAS Collaboration [29]. The predicted differential cross sections ($d\sigma/d\Omega$) as well as polarized ones ($Pd\sigma/d\Omega$) for the $K_L n$ scattering with the final states $K^- p, \bar{K}^0 n, \pi^0\Lambda, \pi^{0/+/-}\Sigma^{0/-/+}$ are presented in Figs. 10 and 11, respectively. There is no clear agreement on the prediction of these observables in the energy range aimed to study in the proposed K_L experiment. The latter is very encouraging in the sense that the actual data can sort out one (or maybe both) solutions as unphysical, which was not possible by the present experimental data.

In summary: The proposed experiment has the potential to shrink the available parameter space of the theoretical models for the antikaon-nucleon scattering. Undoubtedly, this will sharpen our understanding of the $SU(3)$ dynamics, which besides hadronic physics also has important implication for the mass-to-radius relation of neutron stars.

9 πK Scattering Amplitudes and Strange Meson Resonances

9.1 Strange Exotics

An important motivation for performing new measurements of πK scattering amplitudes comes from the need to confirm the existence of the exotic κ meson (or $K_0^*(800)$) in the $I = 1/2$ S-wave. This state would be the strange counterpart of the σ (or $f_0(500)$) meson which is now rather well established from $\pi\pi$ scattering (see the review [104]).

In this regard, improved measurements of the S-wave πK phase-shifts at low energy ($E \lesssim 1$ GeV) would be highly desirable. On the one hand, the existence of this type of resonance is linked to the fact that the phase-shift passes through 45° sufficiently close to the threshold. This, of course is in

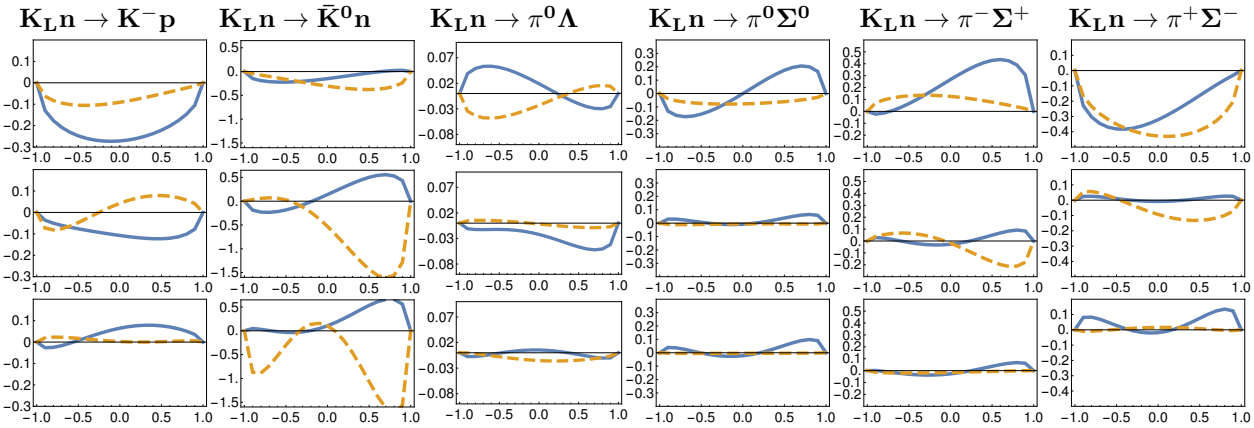

Figure 11: Theoretical predictions for polarized differential cross sections, $Pd\sigma/d\Omega$. The notation is the same as in Fig. 10.

contrast with the case of an ordinary resonance which corresponds to a fast increase of the phase-shift passing through 90°. Fig. 12 illustrate how these phase behaviors on the real axis are related to the presence of a zero of the S matrix on the first Riemann sheet (corresponding to a resonance pole on the second Riemann sheet). The figure, which is based on amplitudes generated from the Roy-Steiner equations (to be discussed below) suggests that the $I = 1/2$ S-wave displays both an exotic resonance and an ordinary one. On a more quantitative side precision measurements of the S-wave phase-shifts would allow application of the Padé approximant method for determining the positions of the resonances (see, e.g., [194]).

Alternatively, the resonance poles can be determined from Roy-Steiner (RS) type equations [106, 107]. These equations provide a suitable framework for performing extrapolations in the low energy region, $E < 1$ GeV, of the S and P partial waves given sufficiently precise inputs at higher energies, essentially in the range $[1-2]$ GeV. Extrapolations for complex values of the energies can be performed with the same accuracy as on the real axis. Unlike the Padé approximant approach, the extrapolation of the $I = 1/2$ S-wave from the RS equations requires inputs from other partial waves as well since the equations form a coupled system. Based on the existing data set, an estimate of the κ pole position from the RS equations was performed in Ref. [108] and more recently in Ref. [109] using forward dispersion relations.

In the P-wave, finally, the studies by the LASS Collaboration [110, 111] have identified besides the well known $K^*(892)$ a new meson, the $K^*(1410)$. This meson has an unexpectedly low mass as it appears to be essentially degenerate with the non-strange $\rho(1450)$ or $\omega(1420)$ vector mesons. Its properties are not very precisely known at present.

9.2 Status of πK Scattering Measurements

The traditional method for measuring $\pi K \to \pi K$ amplitudes is from production measurements

$$Kp \to K\pi p, \quad Kp \to K\pi n, , \quad Kp \to K\pi\Delta \tag{25}$$

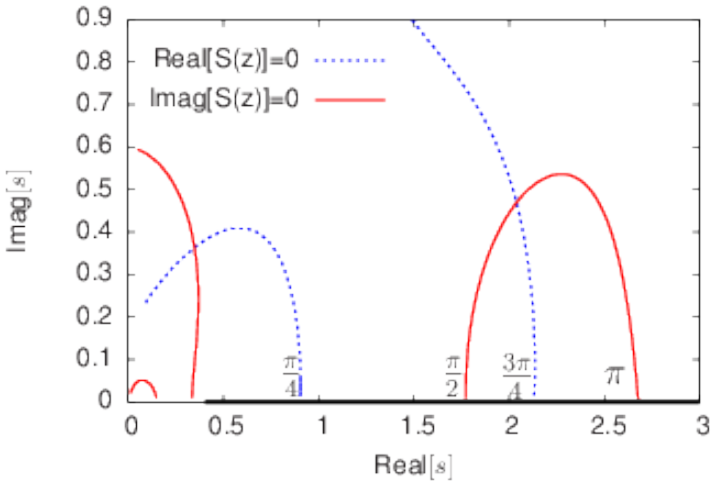

Figure 12: Zeros of the S-matrix, for the $I = 1/2, J = 0$ πK partial-wave on the first Riemann sheet. The figure shows the lines which correspond to $Re[S] = 0$ and $Im[S] = 0$ (intersection of the two lines, obviously, corresponds to a zero of S) and some important phase-shift values on the real axis.

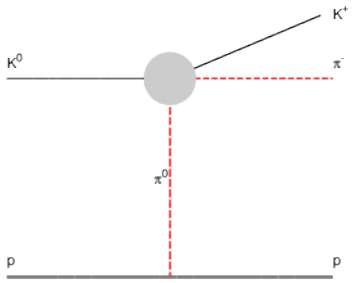

Figure 13: Illustration of the contribution from one-pion exchange, which is dominant at small momentum transfer, to the production amplitude $K_L p \to K^+ \pi^- p$.

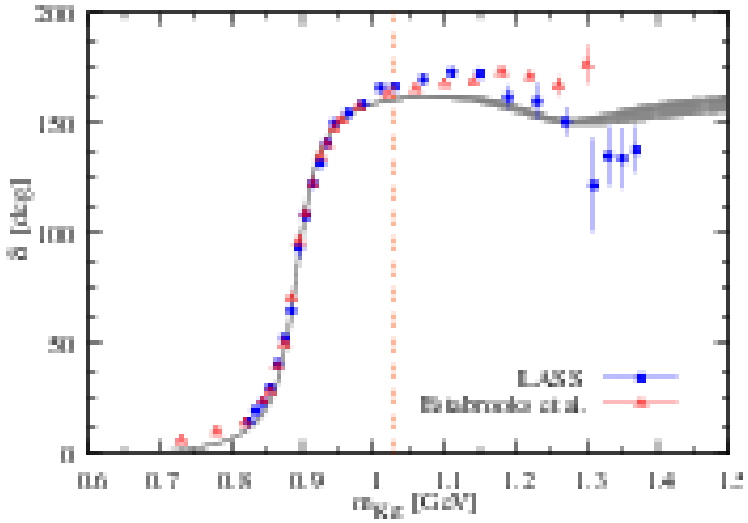

Figure 14: Phase of the πK vector form factor as determined in Ref. [115] and compared with the P-wave phase shifts from Refs. [111, 113]. The two phases should be identical, by Watson's theorem, in the elastic scattering energy region.

focusing on the region of small momentum transfers $|t| < 0.1 - 0.2$ GeV, which is accessible with kaon beams of a few GeV. In this region, the amplitude is dominated by the one pion exchange contribution, see Fig. 13. The same method was used for measuring $\pi\pi \to \pi\pi$ amplitudes, details can be found in the book [112]. The two experiments performed at SLAC [111, 113] have the largest statistics and provide the best determinations of the πK scattering amplitudes at present. They cover the energy ranges $0.73 \leq E \leq 1.85$ GeV (Ref. [113]) and $0.83 \leq E \leq 2.52$ GeV (Ref. [111]), respectively. References to earlier work can be found in the review [114].

A completely different approach to measuring the πK phase-shifts makes use of Watson's theorem for weak decay form factors. In this manner, the phase-shift difference $\delta_S - \delta_P$ was determined from analyzing the $D^+ \to K^-\pi^+e^+\nu$ by the BaBar Collaboration [116]. The results are in agreement with the LASS determination but more statistics are needed before one reaches a comparable precision. Similarly, from the measurement of the energy distribution in the decay $\tau^- \to K_S\pi^-\nu$ by the Belle Collaboration [117] the P-wave phase has been determined [115], relying on the analyticity properties of the form factor. Their result is shown in Fig. 14. Since Watson's theorem is valid in the energy region of elastic scattering, these alternative phase determinations provide important information on the effective onset of inelastic scattering in the various partial waves. The figure also shows that the determination of the phase shift in the region of the $K^*(1410)$ resonance is not very precise and could be improved.

The same form factors which appear in the $\tau \to K\pi\nu$ decays are also involved in the K_{l3} decay amplitudes: $K \to \pi e\nu$, $K \to \pi\mu\nu$. A series of new K_{l3} experiments were undertaken recently in order to improve the determination of V_{us} (see Ref. [118]). As shown in Ref. [118], an optimal analysis of the K_{l3} data is achieved by using a description of the two form factors involved based on phase dispersive representations rather than phenomenological polynomial or pole forms as done previously.

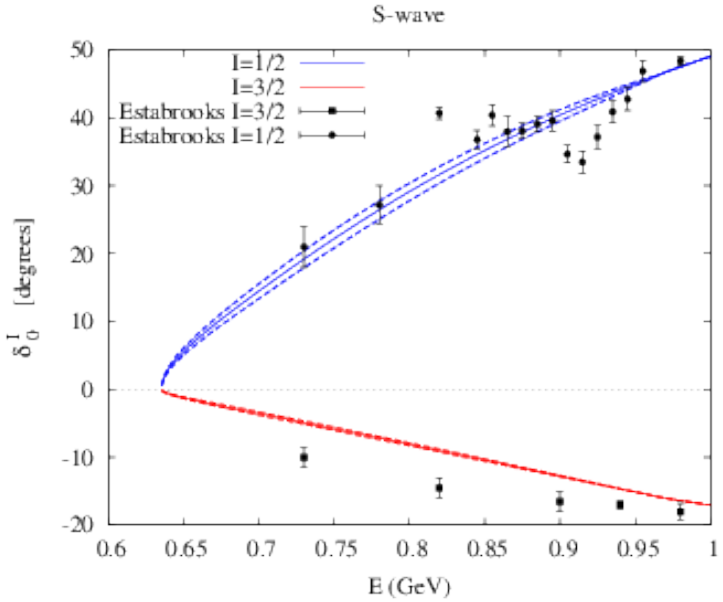

Figure 15: Results for the S-wave phase shifts extrapolated below 1 GeV based on the Roy-Steiner dispersive equations (from Ref. [137]) compared with the experimental data from Ref. [113].

πK scattering also plays an important role in a number of three-body decays, like $D \to K\pi\pi$. Recently, a method was developped [119] which allows to compute the effect of the three-body rescattering in terms of the known two-body $\pi\pi$ and πK T-matrices. This could be useful for identifying small CP violatingeffects in the charm sector.

9.3 Theory

Pions and kaons are QCD pseudo-Goldstone bosons, therefore the πK amplitudes at low energy can be expressed as a chiral expansion. The NLO calculation was performed in ref. [120] who predict the following results for the scattering lengths,

$$a_0^{1/2} = 0.19 \pm 0.02, \quad a_0^{3/2} = -0.05 \pm 0.02 \tag{26}$$

(in units of m_π^{-1}). Verifying these predictions would provide an important check of the three-flavor chiral expansion. Based on experimental phase-shift measurements this is possible, in principle, using dispersion relations for extrapolating down to the threshold. The Roy-Steiner equations provide a suitable framework for that. This is illustrated in Fig. 15 which shows the extrapolated results for the S-waves in the region $E \leq 1$ GeV, based on experimental inputs from Refs. [111, 113] in the region $E > 1$ GeV. It is clear that the availability of more precise data in the range $E \leq 1$ GeV would greatly strengthen the efficiency of this method. We note that a direct experimental estimate of the scattering length difference was performed recently [121] based on the lifetime of the $\pi^+ K^-$ atom.

Finally, scattering phase shifts can be computed in lattice QCD using Lüscher's method [39]. Results for πK phase shifts were first obtained in Refs. [122,123] and in Ref. [54]. In this last work,

the influence of one inelastic scattering two-body channel is accounted for and $m_\pi = 391$ MeV. Very recently, results for $m_\pi = 230$ MeV have been presented [124]. Once physical values for m_π are reached, these lattice QCD results can be compared directly to experimental measurements of the πK phase shifts which provides a direct probe of the quality of the numerical QCD solution.

10 Proposed Measurements

We propose to use the KL Facility with the GlueX spectrometer, in JLab Hall D, to perform precision measurements of $K_L N \to KY^*$ and $K_L N \to Y^* \to \pi Y, KN, K\Xi$ from liquid hydrogen and deuterium cryogenic targets (LH_2/LD_2) in the resonance region, W = 1490 – 2500 MeV and CM $\cos\theta$ from -0.95 to 0.95. It will operate at a neutral kaon flux of 1×10^4 K_L/s (that is by a factor of three order of magnitude higher than SLAC had in the past [168]). The ability of GlueX to measure over wide ranges in θ and ϕ with good coverage for both charged and neutral particles, together with the K_L energy information from the KL Facility, provide an ideal environment for these measurements.

10.1 K_L Beam at Hall D

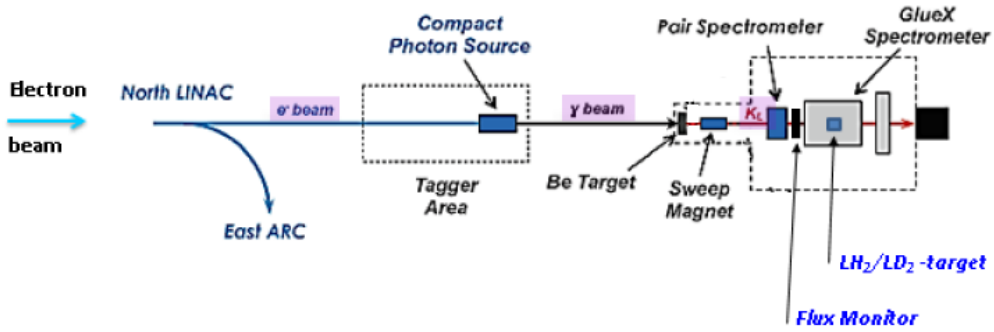

Figure 16: Schematic view of Hall D beamline on the way $e \to \gamma \to K_L$. Electrons first hit the copper radiator inside of CPS, then photons hit the Be target, and finally, neutral kaons hit the LH_2/LD_2 cryogenic target. The main components are CPS, Be target assembly, sweep magnet, and neutral kaons FM (see the text for details).

A schematic view of the Hall D beamline for KLF is presented in Figure 16. At the first stage, $E = 12$ GeV electrons, produced at CEBAF, will scatter in the copper radiator (10 R.L.) inside the Compact Photon Source (CPS) generating an intense beam of untagged bremsstrahlung photons. The CPS will be located downstream of the tagger magnet. The tagger alcove has more space than that available in Halls A/C, so positioning and shielding placement are simpler. The Hall D tagger magnet and detectors will not be used. More details about CPS are in Section 10.1.2. At the second stage, bremsstrahlung photons, created by electrons at a distance about 67 m (photon beamline) upstream, hit the Be target assembly located at the beginning of the collimator cave (Fig. 26), and produce neutral kaons along with neutrons, photons, and charged particles. More details about

a Be target assembly are in Section 10.1.3. The GlueX wiki [269] is a source of the collimator cave geometry. Additional shielding inside of the collimator cave was optimized to minimaize the neutron and gamma background in the experimental Hall D and to satisfy a RadCon requirement establishing the radiation dose rate limit in the experimental hall (1 mrem/h).

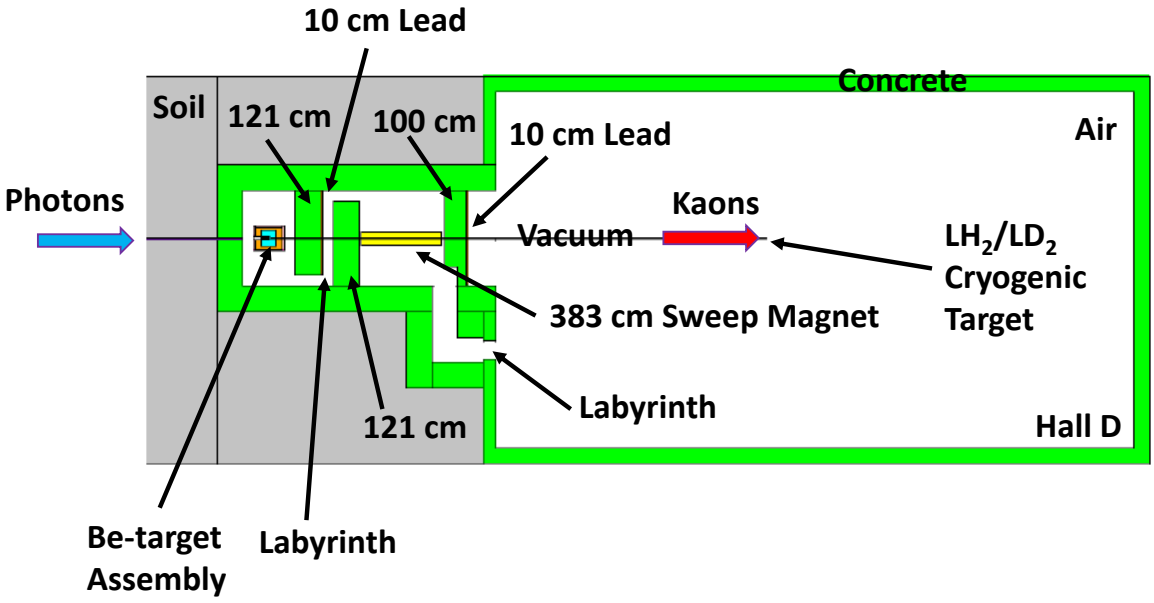

Figure 17: Schematic view of the collimator cave with the Be-target assemply (more details on Fig. 19) concrete wals, and sweeping magnet. Beam goes from left to right.

The beam tungsten plug is placed right after beryllium. Two concrete walls, carried out the first labyrinth upstream, will reduce neutron and photon background and allow access to the Be-target from the experimental hall are both 1.21 m thick and have 0.5 m gap between them (Fig. 17). The first concrete wall has additional 0.10 m lead. The permanent sweeping magnet (3.83 m length) is placed right after the second concrete wall. It cleans up the charged component of the beam and has a field integral of 0.8 Tm, which is enough to remove all charged background coming out of the Be-target assembly.

Table 1: Expected electron/photon/kaon beam conditions at the K_L experiment.

Property	Value
Electron beam current (μA)	5
Electron flux at CPS (s^{-1})	$3.1 \cdot 10^{13}$
Photon flux at Be-target $E_\gamma > 1500$ MeV (s^{-1})	$2.6 \cdot 10^{11}$
K_L beam flux at cryogenic target (s^{-1})	$1 \cdot 10^4$
K_L beam $\Delta p/p$ @ 1 GeV/c (%)	~ 1.5
K_L beam $\Delta p/p$ @ 2 GeV/c (%)	~ 5
K_L beam nonuniformity (%)	< 2
K_L beam divergence ($^\circ$)	< 0.15
$K^0/\overline{K^0}$ ratio at cryogenic target	2:1
Background gamma flux at cryogenic target, $E_\gamma > 50$ MeV (s^{-1})	$\sim 10^5$
Background gamma flux at cryogenic target, $E_\gamma > 500$ MeV (s^{-1})	$\sim 10^3$
Background neutron flux at cryogenic target (s^{-1})	$6 \cdot 10^4$

Table 2: Expected targets properties at the K_L experiment.

Property	Value
Copper radiator in CPS (R.L.)	10
$\varnothing$Be-target (m)	0.06
Be-target length (m)	0.40
$\varnothing LH_2/LD_2$ cryogenic target (m)	0.06
LH_2/LD_2 cryogenic target length (m)	0.40
Photon beamline length (m)	67
Kaon beamline length (m)	24

The vacuum beam pipe has a $\varnothing$0.07 m and prevents neutron rescattering in air. Finally, K_L mesons will reach the LH_2/LD_2 cryogenic target located inside the GlueX spectrometer. The distance between the primary Be and cryogenic targets is 24 m. The flux of K_L mesons will be measured by a Flux Monitor [270] (1.2 m length) located in the experimental hall just in 2 m (it would utilize the K_L in-flight decays) behind the Pair Spectrometer [159]. More details bout FM are in Section 10.1.4.

Our MC calculations have been performed for the JLab Hall D beamline geometry. Tables 1 and 2 summarize beam properties and dimensions of targets, respectively.

10.1.1 Electron Beam Parameters

xxxxxxx–64 ns–xxxxxxxxxxxxxxxxxxxxxxxxxxxxxxxxxxxxxxxxxx

10.1.2 Compact Photon Source: Conceptual Design

An intense high-energy gamma source is a prerequisite for the production of the K_L beam needed for the new experiments described in this proposal. In 2014, Hall A Collaboration has been discussed a novel concept of a CPS [138]. It was developed for a *Wide-Angle Compton Experiment* proposed to PAC43 [139]. Based on these ideas, we suggested (see Ref. [140]) to use the new concept in this experiment. A possible practical implementation adjusted to the parameters and limitations of the available infrastructure is discussed below. The vertical cut of the CPS model design, and the horizontal plane view of the present Tagger vault area with CPS installed are shown in Fig. 18.

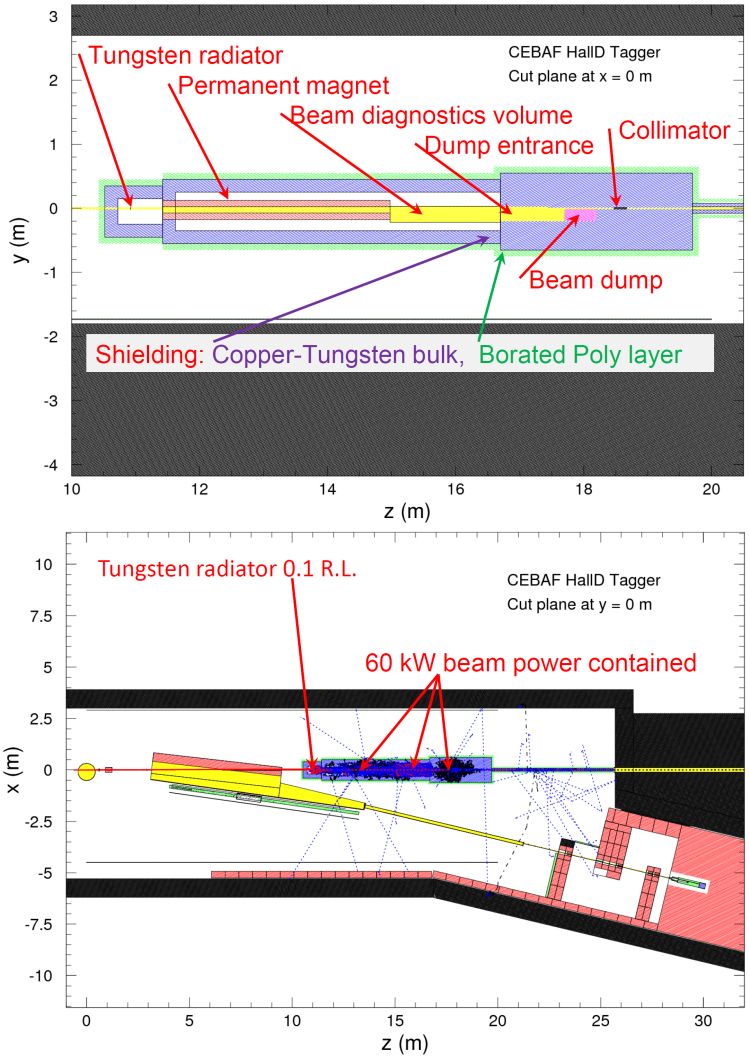

Figure 18: Top panel: Elements of the design (vertical cut plane of the DINREG/Geant3 model of the CPS). Bottom panel: The CPS assembly in the Tagger vault and simulations of 2000 beam electrons at 12 GeV.

The CPS design combines in a single properly shielded assembly all elements necessary for the

production of the intense photon beam, such that the overall dimensions of the setup are limited and the operational radiation dose rates around it are acceptable. Compared to the alternative, the proposed CPS solution presents several advantages: much lower radiation levels, both prompt and post-operational due to the beamline elements' radio-activation at the vault. The new design provides much less disturbance of the available infrastructure at the Tagger Area, and better flexibility in achieving high-intensity photon beam delivery to Hall D. The new CPS solution will satisfy the proposed K_L beam production parameters; we do not envision any significant technical or organizational difficulties in the implementation of the conceptual design.

The new setup utilizes the Hall D Tagger vault, properly shielded by design to accomodate the medium power beam dump capable of accepting up to 60 kW of 12 GeV e^- beam, assuming that proper local shielding is set around the dump. The presently installed dump is placed behind the iron labyrinth walls, and is surrounded by a massive iron shielding, made of iron blocks available at the time of construction. The standard GlueX setup is optimized for operations using very thin radiators producing relatively low intensity photon beam such that the beam electrons losing energy to photon production in the radiator may be detected and counted in the tagger hodoscope counters. The present setup is not suitable for production of massively more intense photon beams needed for the K_L production, due to the expected overwhelming radiation and activation levels in the vault.

The new proposed CPS solution solves the problem by incorporating the new thick radiator and the new beam dump in one assembly installed along the straight beamline exiting from the tagger magnet (presently the line is used as the photon beamline). The new CPS device should be capable of taking the same beam power of 60 kW, using optimized shielding made of high-Z material, which would make the necessary equivalent shielding compact, requiring less total weight of the shielding. Qualitatively, if one needs a sphere of iron (8000 kg/m^3) of 2 m radius for the shielding, it may be roughly replaced by a sphere of 1 m radius made of tungsten-copper (16000 kg/m^3), with its weight actually four times smaller. The optimized design is able to limit the prompt radiation dose rates around the CPS to the present operational levels, while significantly limiting the post-operational doses around the heavily shielded assembly. Of course, the inner parts of the CPS device will be activated to high levels, preventing immediate access and disassembly, so the engineering requirements to the reliability of all parts inside must be strict. The overhead shielding at the CPS location in the tagger vault is about the same thickness (4 m) of concrete and berm as at the present dump location. It will keep the radiation doses outside and at the CEBAF boundary within the design limits for the site.

The proposed CPS solution is just conceptual, and a full cycle of engineering design is required before the final optimized solution is found. The cost and space limitations will determine the choice of shielding materials for the CPS. Details of the dump and magnet design will also be included in the overall optimization process, taking into account the considerations of cost and reliability of the final device. We are considering a possible joint development of the more universal CPS solutions in collaboration with other experimental projects at JLab interested in implementing similar designs for their experiments [141].

10.1.3 Be Target Assembly: Conceptual Design

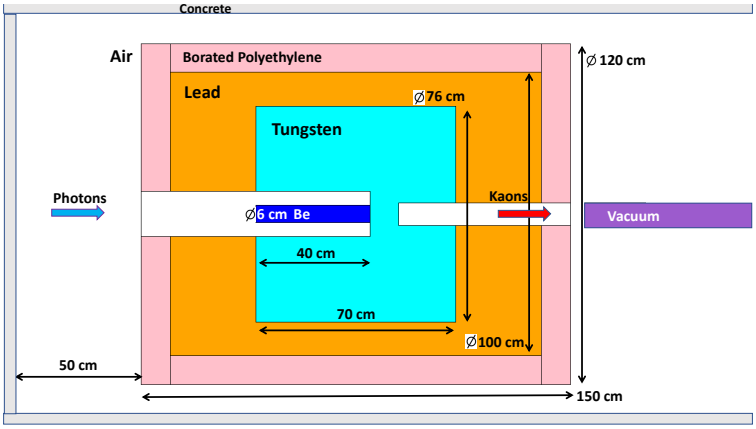

Figure 19: Schematic view of the Be-target (K_L production target) assembly. Concrete, borated polyethylene, lead, tungsten, beryllium, vacuum beam pipe, and air shown by grey, pink, brown, light blue, blue, violet, and white color, respectively. Beam goes from left to right.

A conceptual design of the Be target assembly for neutral kaon experiments to be used with the GlueX experimental setup is given in Ref. [263] (See Appendix A4 (Sec. 16) for further details of elements of the Be-target assembly). Schematic view of the Be-target assembly is given on Fig. 19. For the target material, we selected beryllium because at the same radiation length it has higher number of atoms compared to other materials with the large atomic masses. This justifies the choice of beryllium as a K_L production target was done at SLAC [86] and NINA [84]. The beam tungsten plug of a 0.10 m thick (30 R.L.) is connected to the beryllium (Fig. 19).

Elements of the Be-target assembly are presented in Table 4 (Appendix A4 (Sec. 16)). The weight of the construction is 14.5 ton. Changeover from the photon to K_L beamline and from the K_L beamline to photon is expected to take less or about 6 months (after the radiological cooldown). This break fits current the CEBAF Accelerator schedule well and the beam collimator cave has enough space (4.52 m width) for the Be-target assembly out of the beamline.

Water cooling would be required around the Be target and in the selected tungsten (much higher melting point vs lead, for instance) plug. Cooling water is available in the experimental hall that can be used to dissipate 6 kW of power delivered by the photon beam.

10.1.4 K_L Flux Monitor

An accurate determination of the K_L beam flux is necessary to maximize the physics impact of the resulting data. To reach an accuracy of <5% in the determination of the flux, we plan to build a dedicated Flux Monitor (FM). This will provide a significant improvement over the typical 10% accuracy achievable from normalization of the data to previously measured reactions, for instance, for $K_L p \to K_S p$ [83]. The operation of a K_L flux monitor could employ the regeneration of $K_L \to K_S$ and detection of $\pi^+\pi^-$ pairs in Pair Spectrometer as done at Daresbury (see Ref. [85]

and references therein). However, this technique affects the quality of the resulting K_L beam. Therefore, a more effective choice for the FM at JLab would utilize in-flight decays of the K_L.

The K_L has four dominant decay modes [2]:

1. $K_L \to \pi^+\pi^-\pi^0, BR = 12.54 \pm 0.05\%$.
2. $K_L \to \pi^0\pi^0\pi^0, BR = 19.52 \pm 0.12\%$.
3. $K_L \to \pi^\pm e^\mp \nu_e, BR = 40.55 \pm 0.11\%$.
4. $K_L \to \pi^\pm \mu^\mp \nu_\mu, BR = 27.04 \pm 0.07\%$.

All K_L decay modes with two charged particles in the final state (1,3,4) can be used for flux determination, with a simplest one being $K_L \to \pi^+\pi^-\pi^0$, where both charged particles have the same mass.

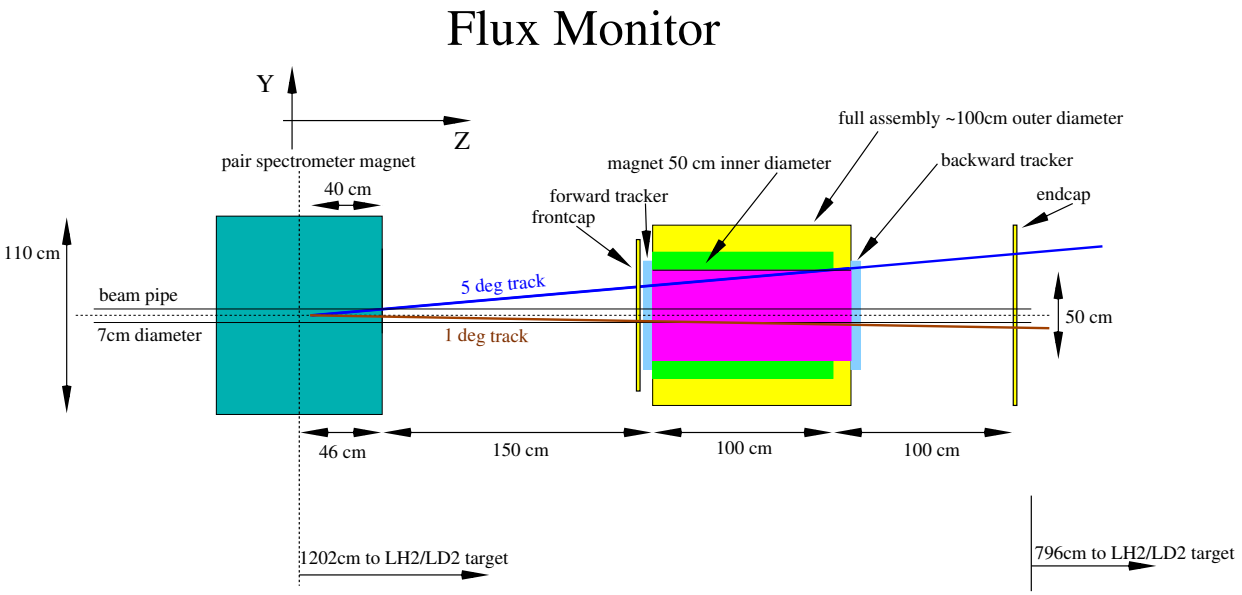

Figure 20: Schematic view of the Flux monitor setup.

To account for various possible acceptance effects during K_L beam propagation from the Be-target, we plan to measure the K_L flux upstream of the GlueX detector, utilizing the Hall D Pair Spectrometer [159] as a shielding against K_L which have decayed further upstream.

The FM design proposed and described in this section will measure a small fraction of decayed K_L's, concentrating on the portion decaying within a distance of 2 m downstream of the Pair Spectrometer magnet centre (see Fig. 20). The FM consists of the following major parts: the front cap, the forward tracker, the backward tracker, the endcap and a solenoidal magnet. The FM can be further equipped with a plastic scintillator barrel, covering inner part of a magnet and a start

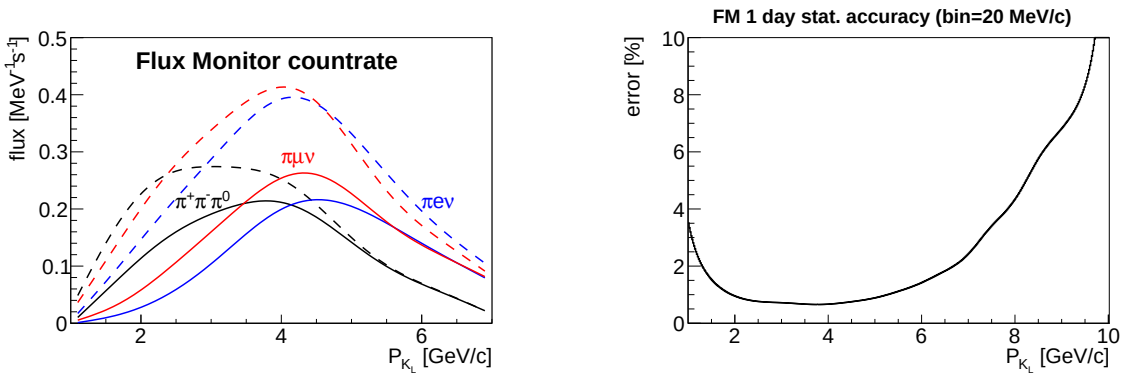

Figure 21: The Flux Monitor performance. Left panel: Visible K_L flux for various decay channels within the FM acceptance. Solid lines correspond to a system with front/end-caps only. Dashed lines show the improvement one can obtain with the additional barrel part extension to the FM. Right panel: Expected statistical accuracy for 1 day FM measurement ($\pi^+\pi^-\pi^0$ branch only) in 20 MeV/c momentum bin.

counter (FMSC), comprising plastic scintillator bars covering the beampipe, from the location of the Pair Spectrometer magnet to the FM magnet.

The front- and end-caps are pizza-piece shaped segmented plastic scintillator used to provide start and stop timing signals for time-of-flight (ToF) as well as signals for the trigger electronics. Each cap is proposed to have double-layer design to improve the time resolution and equipped with Hamamatsu R4998 PMTs (H6533 assemblies). The endcap would be located around 1 m downstream of the FM magnet to improve the achievable ToF resolution. Two trackers will be installed outside the magnetic field covering the downstream and upstream needs of the FM.

To be measured by the FM, both charged particles from the kaon decay need to be incident within the FM acceptance. Taking into account the different branching ratios, we expect to reconstruct the following number of K_L from various decay channels (see Fig. 21(left)). One can quantify the expected rate in terms of the achievable statistical error within a one day measurement (see Fig. 21(right)).

For the kaon beam momenta range appropriate for the hyperon programme a 1% statistical error of the K_L flux determination is achievable in less than a day.

An accurate flux monitoring requires determination of the kaon flux as both a function of transversal position within the beampipe and kaon energy. The most inner 3 cm of the transverse beam profile at the position of the FM would correspond to a 6 cm profile at the cryogenic target. A 7 cm beam pipe diameter allows sufficient margins and the clean definition of a fiducial regions of the transverse beam profile at the FM position. All in all we expect to measure about 1.1k kaon/s in the FM. In the Fig. 23, one can see the kaon flux experienced by the FM and by the cryogenic target, respectively. The increased low momentum yield of kaons observed in the FM compared to the target position arises because these low momenta particles have a larger possibility of decaying in the region between the FM and cryogenic target.

An achievable FM resolution/performance for various case scenarios can be illustrated by Fig. 22.

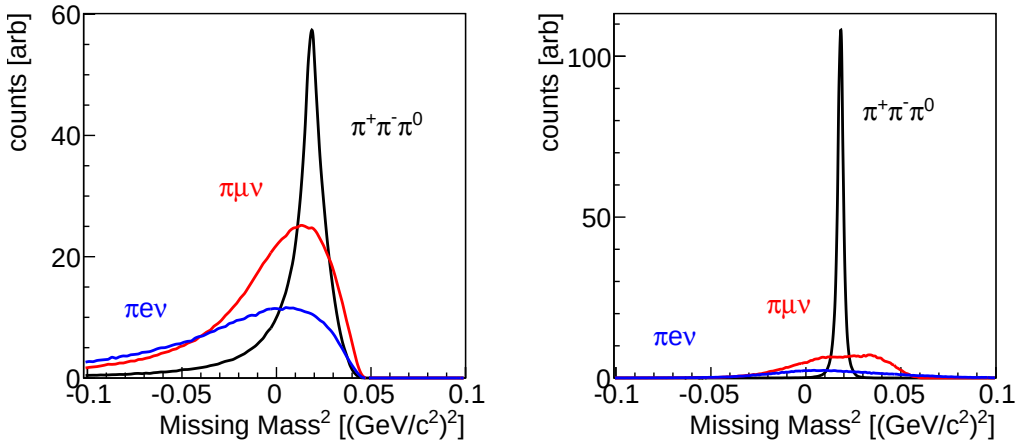

Figure 22: The Flux Monitor missing mass resolution (All charged particles in all decay channels are assumed to have mass of pion). Left panel: based on ToF system. Right panel: based on magnetic system.

Correct mass assignment for the $K_L \rightarrow \pi^+\pi^-\pi^0$ branch give a much narrower missing mass distribution.

The ratio between different branches is fixed. As expected, the magnetic field provides more precise event reconstruction. The flux determination with proposed Flux Monitor and accuracy better than 5% over the full range of energies seems to be feasible. The construction is straightforward and can be completed within 1 year. No prototyping is necessary. No interference with existing Hall-D equipment is expected. For further details about the FM design and performance, see Ref. [142].

10.1.5 K_L Beam Parameters

1. **Simulations Study of K_L Beam Production**

   Neutral kaon production was simulated for a photon bremsstrahlung beam produced by the 12 GeV electron beam in the Hall D CPS. The main mechanism of K_L production in our energy range is via ϕ-meson photoproduction, which yields the same number of K^0 and $\overline{K^0}$. We have taken as a model the Pythia generator [143], which includes hyperon production. Total and differential cross sections for the ϕ-meson photoproduction on proton and complex nuclei (coherent and incoherent) data were taken from Refs. [144, 145]. The angular distributions that we used for $\phi \rightarrow K_L K_S$ decay are from Refs. [144, 146, 147]. Our calculations show that the ϕ decay in its rest frame is mostly perpendicular to the axis of ϕ-momentum. Since K_Ls need to stay along the original photon beam direction to get to the LH_2/LD_2 cryogenic target, this condition requires that the ϕ production and decay angles in the laboratory frame be about the same. That means that we will have only K_Ls from ϕ-mesons produced at relatively high momentum transfer t at the Be target. It suppresses the number of "useful" K_Ls by a factor of ~ 3 or more (in comparison with the case if K_L and K_S momenta

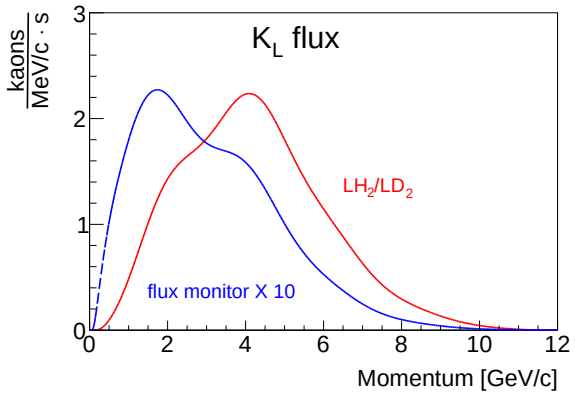

Figure 23: K_L-momentum spectra originating from all sources simulated using Pythia generator [143] for the kaons reached cryotarget (red) and decayed within the Flux Monitor acceptance (blue).

are parallel to the ϕ-momentum). K_L absorption, used in our calculations, was studied in Ref. [148] very well. More than 80% of the produced K_Ls will be absorbed in the Be target and following tungsten beam plug.

One of the main K_L-beam parameters is the momentum distribution (momentum spectrum as a function of the distance and angle) [149]. Results of our simulations for the K_L momentum spectrum for those K_L reaching the LH_2/LD_2 cryogenic target is shown in Fig. 23. The spectrum first increases with K_L momentum up to ~ 4 GeV/c since the ϕ decay cone angle decreases at higher γ-beam and K_L-momenta. This selects lower ϕ production t values, which are more favorable according to the ϕ differential cross section. At a certain point, the highest possible γ-beam momentum is reached and the K_L-momentum spectrum decreases to the endpoint. Pythia calculations show that ϕ decays yield roughly 70% of the K_L flux with the rest originating from hyperon decays. The number of K^0 exceeds the number of $\overline{K^0}$ by 30% points according to this generator for our conditions.

To estimate the expected rate of K_Ls at the LH_2/LD_2 cryogenic target, we used the conditions listed in Tables 1 and 2 which results in a beam flux of about $\mathbf{1 \times 10^4\ K_L/s}$ from all production mechanisms at the cryogenic target (Fig. 24). We simulated the K_L and neutron production from 12-GeV electrons under these conditions for the GlueX K_L Facility and the results (Fig. 24 (left)) are in reasonable agreement with the K_L spectrum measured by SLAC at 16 GeV (Fig. 24 (right)).

2. K_L **Beam Background: Muons, Neutrons, and Gammas**

Background radiation conditions are one of the most important parameters of the K_L beam for the JLab GlueX KL Facility [149].

(a) **Muon Background**

Following Keller [151], our Geant4 [152] simulations included Bethe-Heitler muon background from the Be-production target and photon dump at CPS, both background into the detector and muon dose rate outside Hall D. Obviously, most of the muons are

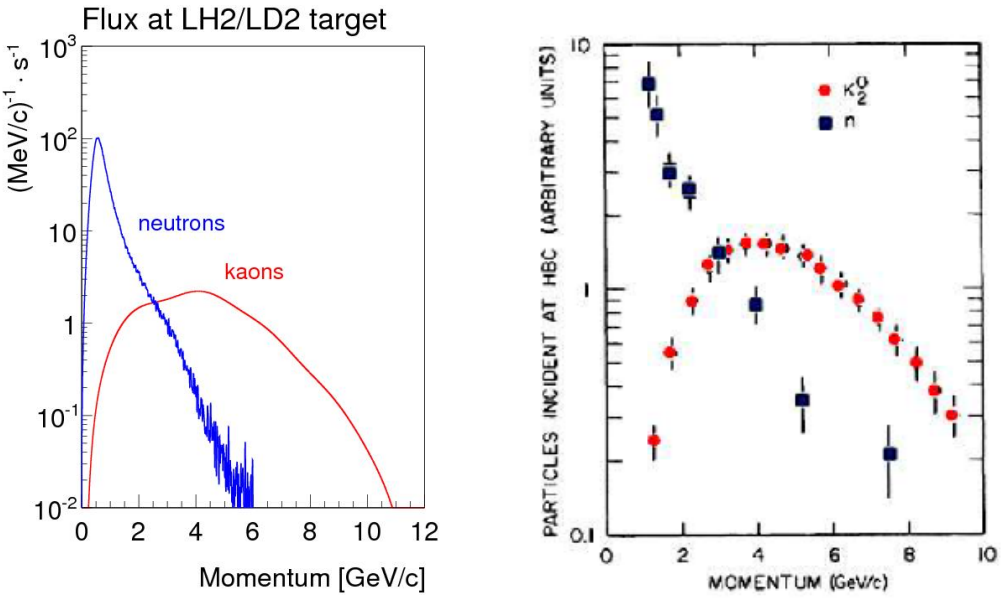

Figure 24: K_L and neutron momentum spectra on the cryogenic target. Left panel: The rate of K_L (red) and neutrons (blue) on the LH_2/LD_2 cryogenic target of Hall D as a function of their generated momentum, with a total rate of $1 \times 10^4 K_L$/s and $6 \times 10^4 n$/s. Kaon calculations were performed using Pythia generator [143] while neutron calculations were performed using the MCNP transport code [154]. Right panel: Experimental data from SLAC measurements using a 16 GeV/c electron beam from Ref. [86]. The rate of K_L (red filled circles) and neutrons (black filled squares).

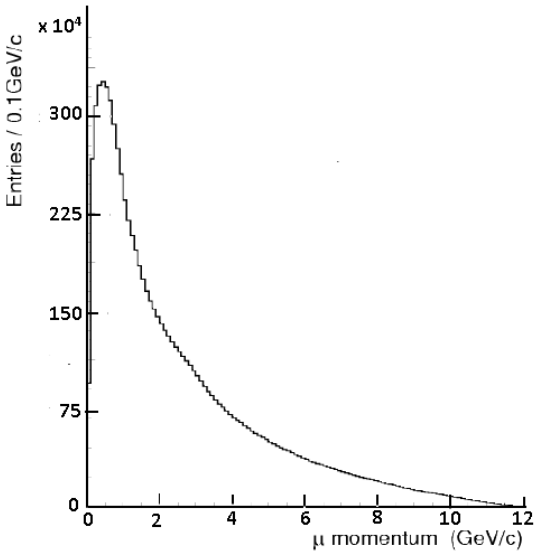

Figure 25: Muon momentum spectrum for Bethe-Heitler production.

produced in the photon dump. Our calculations show that muons will be swept out of the K_L beamline; thus, they are not inherently a significant background. However, due to their high penetration ability, it might be important for purposes of the shielding. We

have taken into account only the Bethe-Heitler muon production process. Muons from pion decays and other production mechanisms will increase the total muon yield only slightly. They were not included in our model. The number of produced muon in the Be target and tunsten beam plug is about the same, but muons originating in tungsten have a much softer momentum spectrum. The estimated number of produced muons is $\sim 6 \times 10^6$ s^{-1}. Their momentum spectrum is shown in Fig. 25.

To summarize: Half of muons will have momenta higher than 2 GeV/c, $\sim$ 10% of muons will have momenta higher than 6 GeV/c, and $\sim$ 1% of muons with have momenta above 10 GeV/c. Overall, the muon flux for the KLF experiment is tolerable.

(b) **Neutron and Gamma Background**

To estimate the neutron and gamma flux in a beam and neutron dose rate in the experimental hall from scattered neutrons and gamma, we used the MCNP6 N-Particle (MCNP) Transport code [154]. The realism of MCNP simulations is based on the advanced nuclear cross section libraries created and maintained in national laboratories of DOE complex. The physical models implemented in the MCNP6 code take into account bremsstrahlung photon production, photonuclear reactions, neutron and photons multiple scattering processes. The experimental hall, collimator cave, and photon beam resulted from copper radiator were modeled using the specifications from the layout presented in Figure 26 shown as a 3D graphic model of the experimental setup.

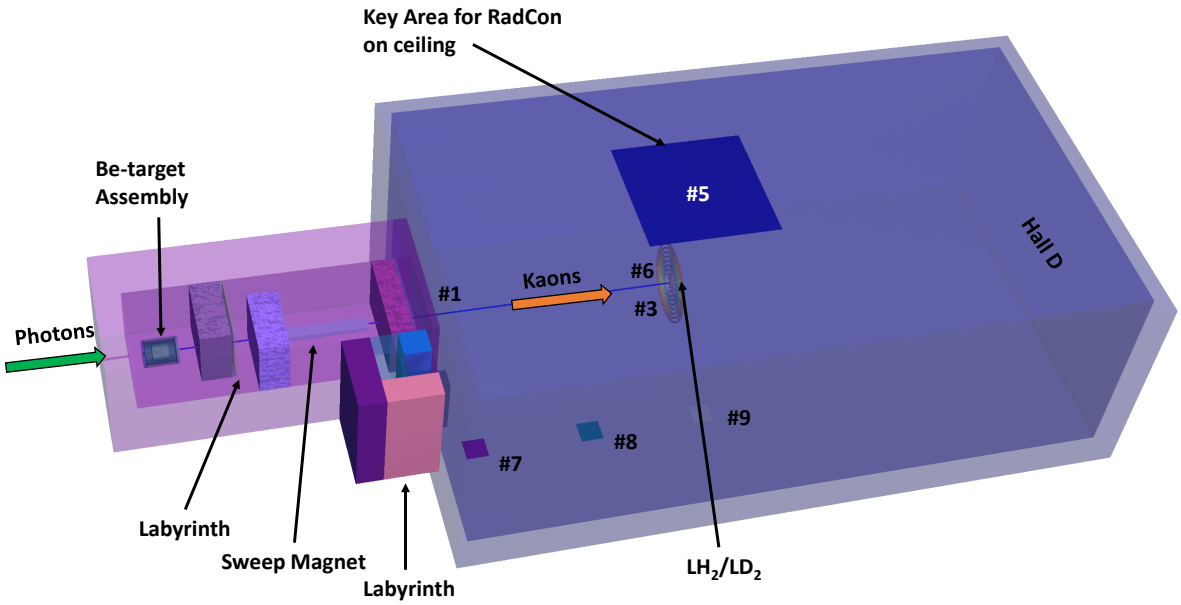

Figure 26: Schematic view of Hall D setting for MCNP transport code [154] calculations. Beam goes from left to right. The model is presented as semi-transparent for demonstration purposes. This 3D plot is a part of Hall D beamline as Fig. 16 and some tallies are shown.

The MCNP model simulates a 12 GeV 5μA electron beam hitting the copper radiator

inside the CPS. Electron transport was traced in tungsten radiator, vacuum beam pipe for bremsstrahlung photons, and Be-target. Neutrons and photons were traced in all components of the used MCNP model. The media outside concrete walls of the collimator cave and bremsstrahlung photon beam pipe was excluded from consideration to facilitate the calculations.

For MCNP calculations (in terms of flux [part/s/cm^2] or biological dose rate [mrem/h]), several tallies (as Tables 5 and 6 will show below) were placed along the beam and at the experimental hall for neutron and gamma fluence estimation Tally descriptions are given in Appendix A4 (Sec. 16). Fluence-to-Effective Dose conversion factors from ICRP 116 [155] were implemented to convert neutron fluence to effective dose rate.

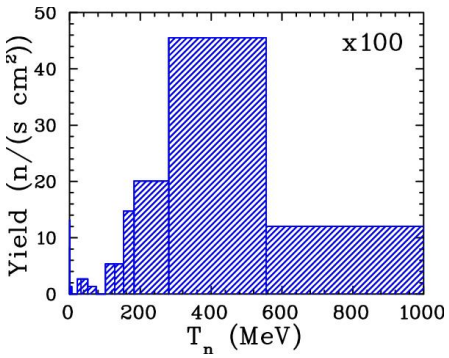

Figure 27: Neutron energy spectrum on the beam and face of the cryogenic target, tally #3.

The tally #5 (Table 6) was selected by the RadCon to estimate neutron fluence at the experimental hall ceiling just above the GlueX detector. That is the Key Area for RadCon shown on Fig. 26. The neutron dose rate calculated for the layouts from Fig. 58 on tally #5 is 0.02$\pm$0.01 mrem/h. It is acceptable by RadCon.

The neutron flux on the face of the LH_2/LD_2 cryogenic target (tally #3) is 1.6×10^4 n/(s·cm^2). The spectrum of neutrons at the face of the cryogenic target is shown on Fig. 27. The neutron energy on the cryogenic target varied between 0.1 – 1 GeV and flux is not enough to provide a significant background in the case of np or nd interactions in the cryogenic target.

The neutron dose rate (Table 6) for the silicon photomultipliers (SiPM) of the start counter [153, 264, 266] and BCAL [265, 266] is given on Fig. 28 (left). There is an issue for SiPM and low level of BCAL. Previous studies stand that the dose rate of 30 mreh/h increases a dark current at SiPM by a factor of 5 after 75 days of running period [271].

In our calculations, we ignored Pair Spectrometer and FM magnets. In new calcluations, we will take them into account plus 4 SEG-blocks around the beam and a concrete block (same size as SEG-block) with a steel collimator for the beam pipe (outer $\varnothing$13 cm and inner $\varnothing$8 cm). Our hope is that will reduce a radiation damage for SiPM and BCAL.

To estimate the photon flux in a beam and gamma dose rate in the experimental hall from scattered neutrons, we used the same MCNP Transport code [154]. After passing

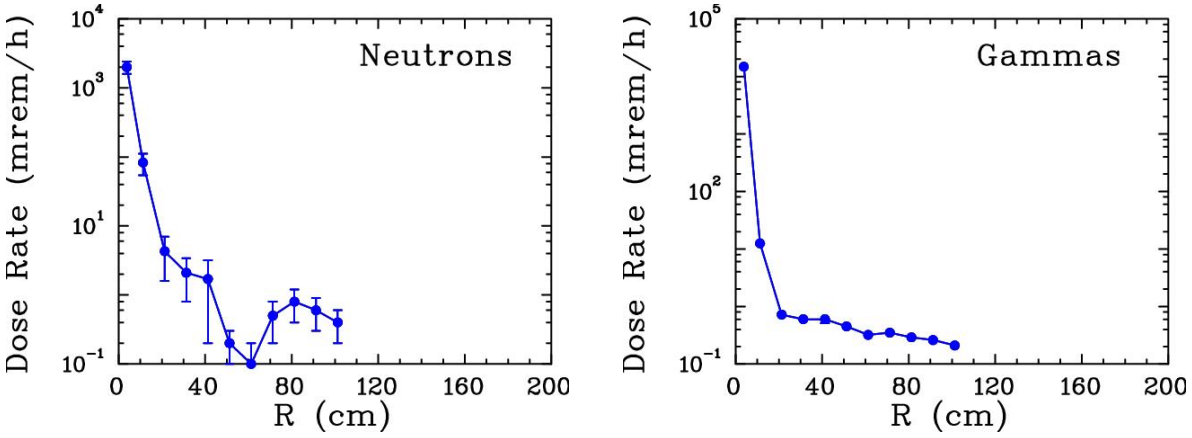

Figure 28: Neutron (left) and gamma (right) dose rate background calculated for SipM (tally #6) and BCAL (tallies #10-19) on the face of the cryogenic target.

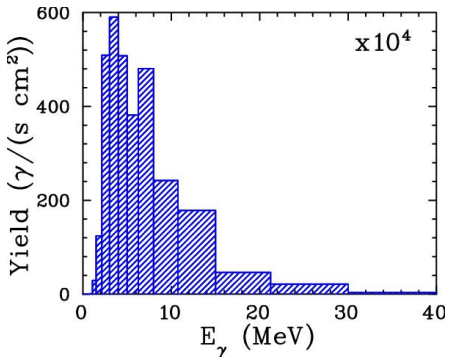

Figure 29: Gamma energy spectrum at tally #1.

through 30 R.L. tungsten beam plug and the charged background component removed by the sweep magnet, we will have some residual γ background produced by EM showers. The energy spectrum of residual γs is shown in Fig. 29. It decreases exponentially with increasing energy of photons and cannot exceed 30 MeV. The gamma dose calculeted on tally #5 is $(2.1\pm0.1)\times10^{-2}$ mrem/h which is acceptable by RadCon.

To summarize, the neutron and gamma flux and dose rate for the KLF experiment is below the RadCon limit as Tables 5 and 6 show. Overall, the Be-target assembly conceptual design satisfies the RadCon requirement establishing the radiation dose rate limit in the Hall D. The full engineering design is in progress.

3. K_L **Momentum Determination and Beam Resolution**

The mean lifetime of the K_L is 51.16 ns ($c\tau = 15.3$ m) whereas the mean lifetime of the K^- is 12.38 ns ($c\tau = 3.7$ m) [2]. For this reason, it is much easier to perform measurements of K_Lp scattering at low beam energies compared with K^-p scattering.

The momentum of a K_L beam can be measured using time-of-flight (TOF) - the time between the accelerator bunch (RF signal from CEBAF) and the reaction in the LH_2/LD_2 target as detected by the GlueX spectrometer. Thus the TOF resolution is a quadratic sum of acceler-

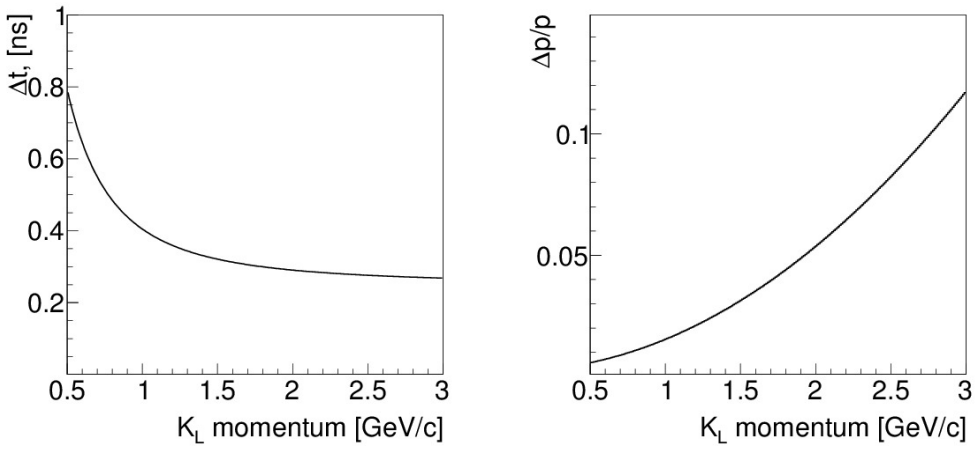

Figure 30: Left panel: Time resolution, Δt, for K_L beam as a function of K_L-momentum. Right panel: Momentum resolution, $\Delta p/p$, as a function of momentum.

ator time and GlueX spectrometer time resolutions. Since the accelerator signal has a very good time resolution (~ 150 ps or better), TOF resolution will be defined by GlueX detector. The time resolution of the GlueX detectors are discussed in Sec. 4. In our calculations, we used time resolutions of 250 ps to show the dependence of the beam momentum and W resolution.

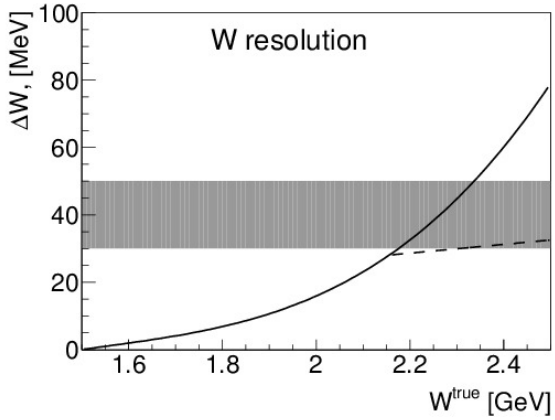

Figure 31: Energy resolution, Δ_W/W, as a function of energy. Dashed line shows approximate W resolution from reconstruction of final-state particles. Shaded area corresponds to typical hyperon width.

Of course, to get TOF information, the electron beam needs to have a narrow bunch time structure. As discussed in Sec. 10.1.1, the electron beam can be delivered with predetermined repetition rate. For the K_L experiment, the 64 ns bunch spacing structure is an optimal choice. It allows no cross-bunch overlap for the full range of kaon beam momentum from $p_{K_L} > 320\ MeV/c$.

The uncertainty in a neutral kaon production position at lower momenta (p < 0.5 GeV/c) affects timing resolution caused by the TOF difference between the photon and kaon time traversing the Be target, however, as $\Delta p/p = \gamma^2 \Delta t/t$ momentum resolution is below 1% at lower momenta. Figure 30 shows TOF, Δt, (left) and beam momentum resolution, $\Delta p/p$ (right) as a function of the K_L beam momentum, respectively. The TOF resolution is flat for momenta higher than 1 GeV/c. The momentum resolution decreases with momentum: for 1 GeV/c it is $\sim$1.5% and for 2 GeV/c it is $\sim$5%. Figure 31 shows that for $W < 2.18$ GeV, $\Delta W < 30$ MeV, which is suitable for studying low-lying hyperons with widths of $\Gamma = 30$ – 50 MeV [2]. For fully reconstructed final states W can be reconstructed directly, providing a better resolution in the region where the TOF method deteriorates, $W > 2.2$ GeV (see dashed curve in Fig. 31).

4. **GlueX Detector Time Resolution**

   The K_L beam momentum and time resolution is governed by the time resolution provided by the GLUEX detector from the reconstruction of charged particles produced in the LH_2/LD_2 target. There are three detector systems that can provide precision timing information for reconstructed charged particles in GLUEX: the Start Counter (ST) [264], Barrel Calorimeter (BCAL) [265], and Time of Flight (TOF) detectors. The aforementioned detectors, and the charged particle time resolutions they provide, are discussed in this section.

   The GLUEX ST is a cylindrical plastic scintillator detector surrounding the LH_2/LD_2 target, with 3 mm thick scintillator bars and a tapered nose region that bends toward the beamline at the downstream end. The scintillation light from each of the 30 scintillator bars is detected by an array of 4, 3×3 mm^2 Hamamatsu S10931-050P surface mount silicon photomultipliers (SiPMs) [158]. The time resolution of the ST was determined to be 250 ps during the 2016 and 2017 GLUEX run periods, as shown in Fig. 32, and thus provided adequate separation of the 250 MHz photon beam bunch structure delivered to Hall D during that time. This performance was achieved using the recommended operating gain and bias voltages supplied by Hamamatsu to provide both the FADC 250 analog signals and precision F1TDC discriminator signals used in the GLUEX reconstruction.

   To summarize: The simulation studies in this proposal (See Sec. 11) have assumed a time resolution of 250 ps, which is adequate for the proposed physics program. With the current detector, the overall K_L-momentum resolution will be determined by utilizing the timing information from the ST, BCAL, and TOF detectors and will probably overshoot a very conservative 250 ps specification. Finally, we are exploring potential upgrades to improve the ST time resolution significantly; however, such improvements would not influence much on the resonance parameters extracted by the partial wave analysis, hence have low priority for the proposed hyperon spectroscopy program.

10.2 LH_2/LD_2 Cryogenic Target for Neutral Kaon Beam at Hall D

The proposed experiment will utilize the existing GlueX liquid hydrogen cryogenic target (Fig. 33) modified to accept a larger diameter target cell [162]. The GlueX target is comprised of a kapton

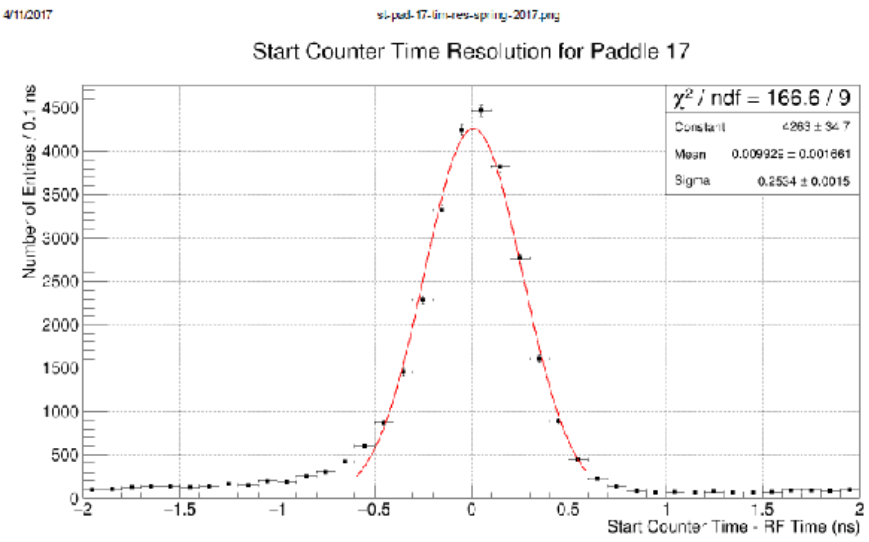

Figure 32: Time difference between the measured and expected ST time from the Spring 2017 GLUEX run period. The data were fitted with a Gaussian to determine the current time resolution of $\sim$ 250 ps.

cell containing liquid hydrogen at a temperature and pressure of about 20 K and 19 psia, respectively The 100 ml cell is filled through a pair of 1.5 m long stainless steel tubes (fill and return) connected to a small container where hydrogen gas is condensed from two room-temperature storage tanks. This condenser is cooled by a pulse tube refrigerator with a base temperature of 3 K and cooling power of about 20 W at 20 K. A 100 W temperature controller regulates the condenser at 18 K.

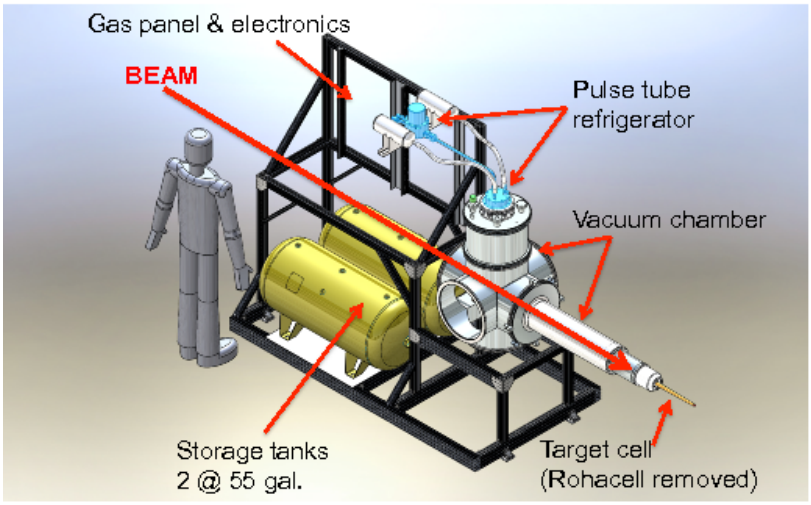

Figure 33: The GlueX liquid hydrogen target.

The entire target assembly is contained within an “L"-shaped stainless steel and aluminum vacuum chamber with a Rohacell extension surrounding the target cell. The ST for the GlueX experiment fits snugly over this extension. The vacuum chamber, along with the hydrogen storage tanks, gas

handling system, and control electronics, is mounted on a custom-built beamline cart for easy insertion into the Hall D solenoid. A compact I/O system monitors and controls the performance of the target, while hardware interlocks on the target temperature and pressure and on the chamber vacuum ensure the system's safety and integrity. The target can be cooled from room temperature and filled with liquid hydrogen in about 5 hours. For empty target runs, the liquid can be boiled from the cell in about 20 minutes (the cell remains filled with cold hydrogen gas), and then refilled with liquid in about 40 minutes.

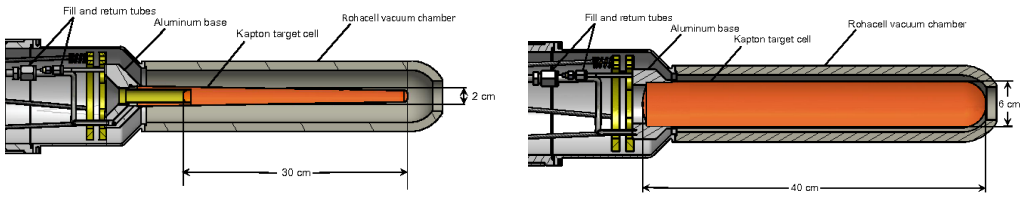

Figure 34: Left: Kapton target cell for the GlueX LH_2/LD_2 cryogenic target. Right: Conceptual design for a larger target cell for the proposed K_L beam at Hall D experiment.

The GlueX cell (Fig. 34) is closely modeled on those utilized at Hall B for more than a decade and is a horizontal, tapered cylinder about 0.38 m long with a mean diameter of 0.02 m. The cell walls are 130 μm kapton glued to an aluminum base. A $\varnothing$0.02 m reentrant beam window defines the length of LH_2/LD_2 in the beam to be about 0.30 m. Both entrance and exit windows on the cell are 75 μm kapton. In normal operation, the cell, the condenser, and the pipes between them are all filled with liquid hydrogen. In this manner, the liquid can be subcooled a few degrees below the vapor pressure curve, greatly suppressing bubble formation in the cell. In total, about 0.4 liter of LH_2 is condensed from the storage tanks, and the system is engineered to recover this quantity of hydrogen safely back into the tanks during a sudden loss of insulating vacuum, with a maximum allowed cell pressure of 49 psia [163].

A conceptual design for the neutral kaon beam target is also shown in Fig. 34. The proposed target cell has a $\varnothing$0.06 m and a 0.40 m length from entrance to exit windows, corresponding to a volume of about 1.1 liter, which will require filling the existing tanks on the target cart to about 50 psia. The collaboration will work with the JLab Target Group to investigate alternative materials and construction techniques to increase the strength of the cell. As an example, the LH_2 target cell recently developed for Hall A is $\varnothing$0.063 m, 0.18 m long and has a wall thickness of approximately 0.2 mm. The cell is machined from a high-strength aluminum alloy, AL7075-T6, and has a maximum allowed pressure of about 100 psia. It is expected that minor modifications to the cryogenic target's piping systems will also be required to satisfy the increased volume of condensed hydrogen.

The proposed system is expected to work equally well with liquid deuterium, which condenses at a slightly higher temperature than hydrogen (23.3 K versus 20.3 K at atmospheric pressure). The expansion ratio of LD_2 is 13% higher, which implies a storage pressure of about 60 psia. Therefore, the new target cell must be engineered and constructed to work with both LH_2 and LD_2.

11 Running Condition

11.1 Event Identification, Reconstruction, Acceptances

The K_L beam is generated by sampling the momentum distribution of K_L particles coming from the decays of ϕ mesons produced by interactions of a photon beam with a beryllium target 24 m upstream of the LH_2/LD_2 cryogenic target. The K_L beam profile was simulated to be uniform within a $\varnothing$0.06 m at the LH_2/LD_2 cryogenic target. The expected K_L beam nonuniformity is below 2%, beam divergence $< 0.15^\circ$ (see Table 1). Due to the very strong t-dependence in the ϕ photoproduction cross section [164] and the P-wave origin of the $\phi \to K_L K_S$ decay, the majority of kaons will be produced at very small angles. In the simulation studies discussed in this section, we assume a flux of $1 \times 10^4 K_L$/s on a 0.40 m long LH_2 target for a beamtime of 100 PAC days.

11.1.1 Simulations and Reconstruction of Various Channels Using GlueX Detector

The GlueX detector is a large acceptance detector based on a solenoid design with good coverage for both neutral and charged particles. The detector consists of a solenoid magnet enclosing devices for tracking charged particles and detecting neutral particles, and a forward region consisting of two layers of scintillators (TOF) and a lead-glass EM calorimeter (FCAL). A schematic view of the GlueX detector is shown in Fig. 35. The magnetic field at the center of the bore of the magnet for standard running conditions is about 2 T. The trajectories of charged particles produced by interactions of the beam with the 0.40-m LH_2/LD_2 cryogenic target at the center of the bore of the magnet are measured using the Central Drift Chamber (CDC) for angles greater than $\approx 20^\circ$ with respect to the beamline Forward-going tracks are reconstructed using the Forward Drift Chambers (FDC). The timing of the interaction of the kaon beam with the LH_2 cryogenic target is determined using signals from the ST, an array of 30 mm thin (3 mm thick) scintillators enclosing the target region. Photons are registered in the central region by the BCAL. Detector performance and reconstructions techniques were evaluated during the main GlueX program. Details can be found elsewhere [165].

This section describes some simulations of events generated by K_L beam particles interacting with a LH_2/LD_2 cryogenic target at the center of the solenoid [166]. All simulations assumed standard beam/target conditions listed in Tables 1 and 2. The GlueX detector is used to detect one or all of the final-state particles. We will be focusing on a few of the simple two-body reactions, namely

1. $K_L p \to K_S p$,
2. $K_L p \to \pi^+ \Lambda$,
3. $K_L p \to K^+ \Xi^0$
4. $K_L p \to K^+ n$.
5. $K_L p \to K^+ \pi^+ p$.

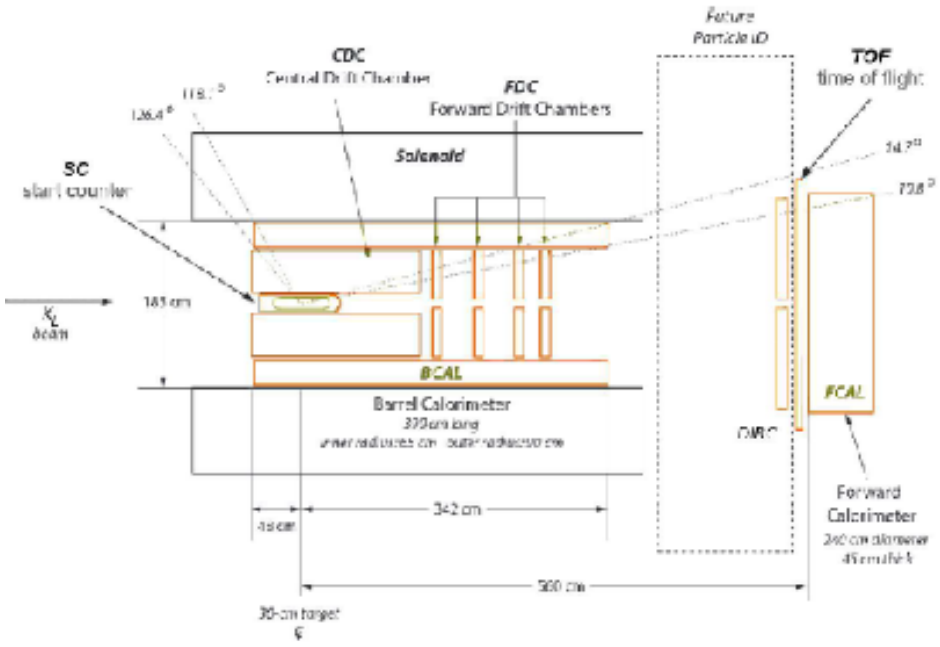

Figure 35: Schematic view of the GlueX detector.

For each topology, one particle (the proton for the $K_S p$ channel, the π^+ for the $\pi^+\Lambda$ channel and the K^+ for the $K^+\Xi^0/K^+n$ channels) provides a rough determination for the position of the primary vertex along the beamline that is used in conjunction with the ST to determine the flight time of the K_L from the Be target to the hydrogen target. Protons, pions, and kaons are distinguished using a combination of dE/dx in the chambers and time-of-flight to the outer detectors (the BCAL and two layers of scintillators (TOF)). See Appendix A4 (Sec. 16) for further details.

11.1.2 $K_L p \to K_S p$ Reaction

The total production cross section, shown in Fig. 36, is reasonably large; however, for the differential cross section there is a fair amount of tension in the existing data sets between different measurements, and the angular coverage in some bins is sparse. Figure 37 shows the existing differential cross-section data for several bins in W. The cross section as a function of $\cos\theta_{CM}$ was parametrized using a set of Legendre polynomials (blue curves in Fig. 37); the weights of each polynomial in the set depended on W. This parametrization was used to generate $K_L p \to K_S p$ events that were passed through a full Geant3-based Monte Carlo (MC) of the GlueX detector. The final-state particles were constructed using the standard GlueX reconstruction code. We reconstructed the K_S in its $\pi^+\pi^-$ channel. More details about the reconstruction of this channel can be found in Appendix A5 (Sec. 17.1.1). Estimates for statistical errors in the measured cross section for 100 days of running as a function of $\cos\theta_{CM}$ for several values of W are shown in Fig. 38. We estimate that for $W < 3$ GeV, we will detect on the order of 2.7M $K_S p$ events in the $\pi^+\pi^-$ channel.

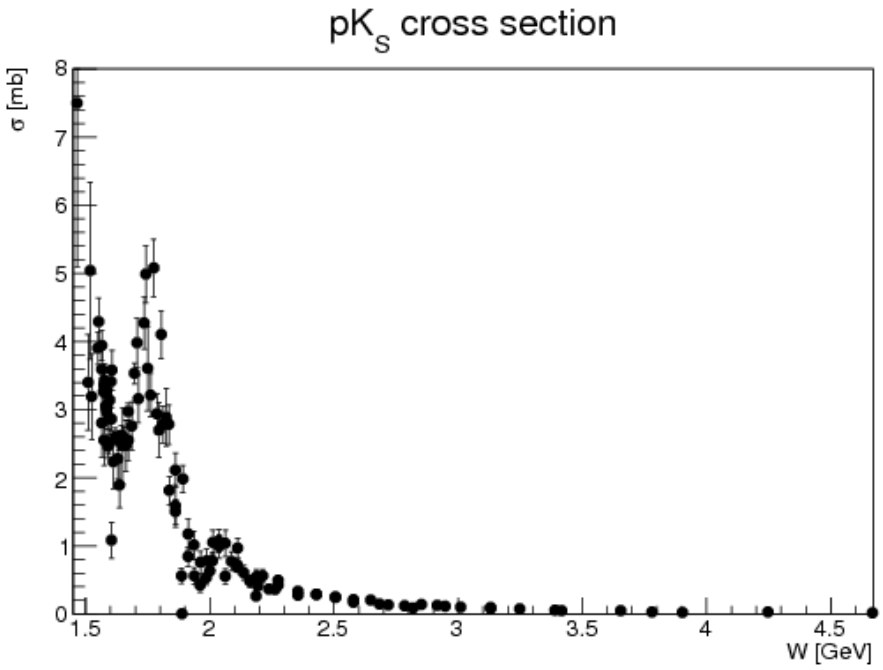

Figure 36: Total cross section for $K_Lp \rightarrow K_Sp$ as a function of W. The measured points are from [167] and references therein.

11.1.3 $K_Lp \rightarrow \pi^+\Lambda$ Reaction

The $K_Lp \rightarrow \pi^+\Lambda$ and $K_Lp \rightarrow \pi^+\Sigma^0$ reactions are key to studying hyperon resonances - an analog of $N\pi$ reactions for the N^* spectra. They are also the key reaction to disentangling the weak exchange degeneracy of the $K^*(892)$ and $K^*(1420)$ trajectories. (A general discussion is given in Appendix A1 (Sec. 13 and 9). The first measurement of this reaction was performed at SLAC in 1974 [168] for K_0 beam momentum range between 1 GeV/c to 12 GeV/c. The total number of $\pi^+\Lambda$ events was about 2500 events, which statistically limits the measurement.

Through the MC simulation, we show our estimate of the statistical uncertainty of the $\pi^+\Lambda$ total cross section as a function K_L beam momentum with GlueX detector in Hall-D as shown in Fig. 39 (left). We kept the same momentum bin size as the one from the SLAC data. The box-shaped error bars in the MC points (red triangles) were increased by a factor of 10 for comparison with the SLAC data. The proposed measurements will provide unprecedented statistical accuracy to determine the cross section for a wide range of K_L-momentum. In Fig. 39 (right), the t-dependent cross-sections were shown in three beam momentum bins same as SLAC data sets: p_{K^0}=1.5-2.5 GeV/c (solid bullets), p_{K^0}=2.5-3.5 GeV/c (solid rectangles)and p_{K^0}=3.5-5.0 GeV/c (solid triangles). As it shows, a strong forward peaking in t-channel for all momenta was observed, which appears to move out $\langle -t \rangle$ = 0.4-0.5 GeV^2 at higher momenta.

Parity violation in the weak decay of Λ makes it possible to measure the induced polarization. The induced Λ polarization (P_Λ) can be observed by measuring the angular distribution of the proton with respect to the normal vector to the production plane. As one can learn from Section 6 the recoil

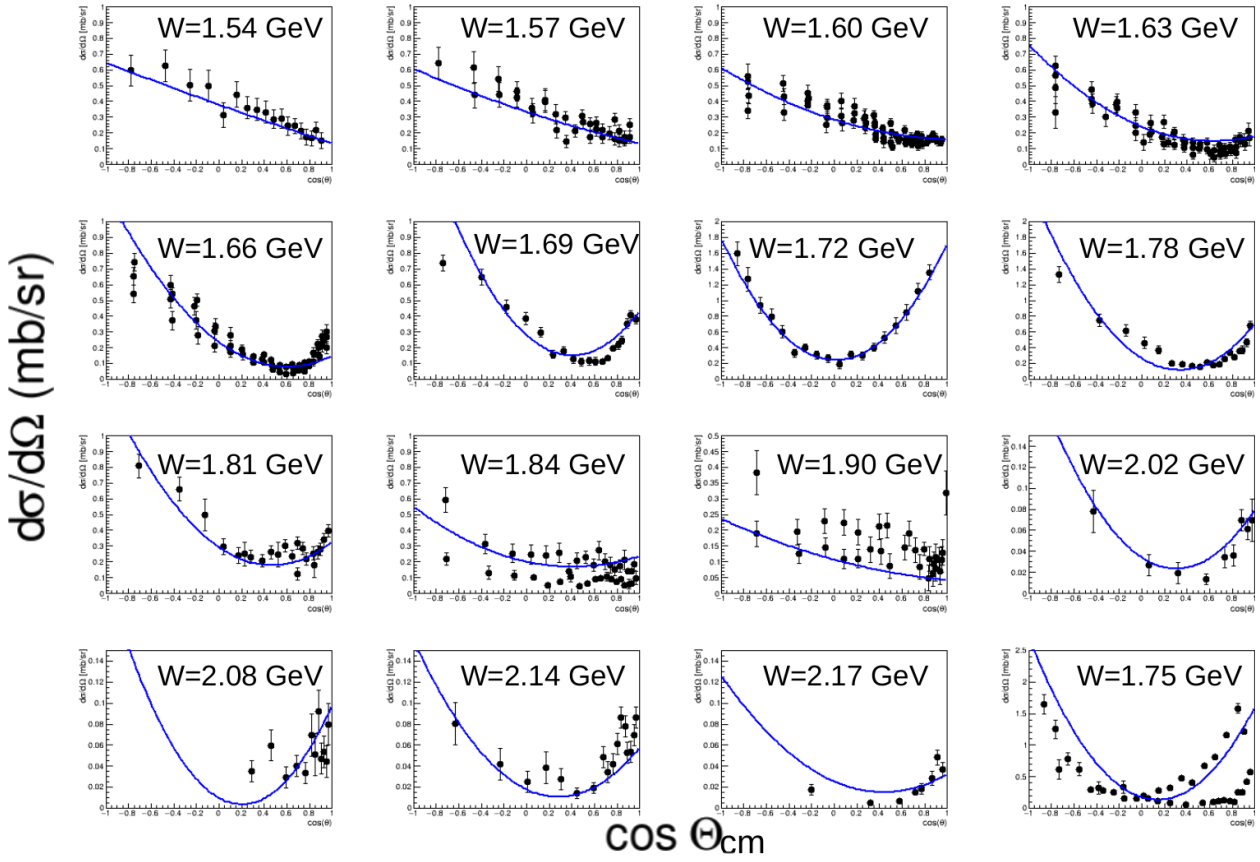

Figure 37: Differential cross-section plots for $K_L p \to K_S p$ as a function of W. The blue curves are the result of a parametrization of the cross section in terms of Legendre polynomials. The measured points are from [167].

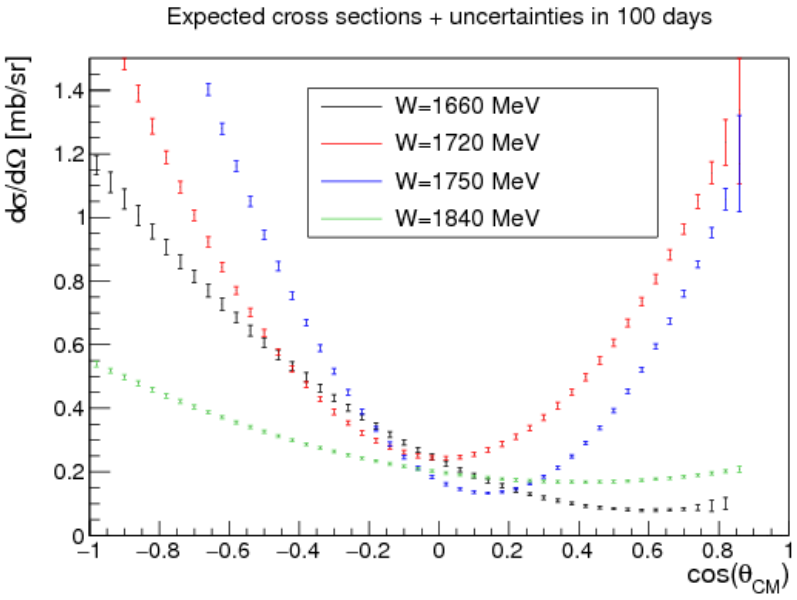

Figure 38: Reconstructed $K_L p \to K_S p$ differential cross sections for various values of W for 100 days of running.

polarisation is extremely sensitive and valuable tool to constrain PWA amplitudes. Our simulations show that existing SLAC data can be improved a lot by K_L facility at JLab (see Fig. 40).

11.1.4 Cascade Reactions on Proton and Neutron Targets: $K_L p \to K^+\Xi^0$ and $K_L n \to K^+\Xi^-$

The study of cascade data will allow us to place stringent constraints on dynamical coupled-channel models. It was recently found in N^* spectroscopy that many N^* resonances do not couple strongly to a $N\pi$ channel, but are nicely seen in $K\Lambda$ and $K\Sigma$ channels. The corresponding situation in hyperon spectroscopy lead to many Λ^* and Σ^* resonances decaying preferably to a $K\Xi$ channel, see Appendix A1 (Sec. 13 for details. In addition, cascade data will provide us with long-sought information on missing excited Ξ states and the possibility to measure the quantum numbers of the already established $\Xi(1690)$ and $\Xi(1820)$ from a double-moments analysis. The expected large data sample will allow us to determine the induced polarization transfer of the cascade with unprecedented precision, which will place stringent constraints on the underlying dynamics of the reaction. Polarization measurements of hyperons shed light on the contribution from individual quarks to the overall polarization of these states. The polarization of the ground-state cascade can be measured from its weak decay in a straightforward way. With a K_L beam, the study of the reactions $K_L p \to K^+\Xi^0$ and $K_L n \to K^+\Xi^-$ is quite simple and an unprecedented statistical sample can be easily obtained. The statistical uncertainty obtained for 2-fold differential polarization observables with 100 days of beam time ($\sim 1 \times 10^5$ reconstructed events) is of the order of 0.05-0.1, which is more than an order of magnitude smaller from existing measurements, allowing precision tests on the underlying dynamics to be performed.

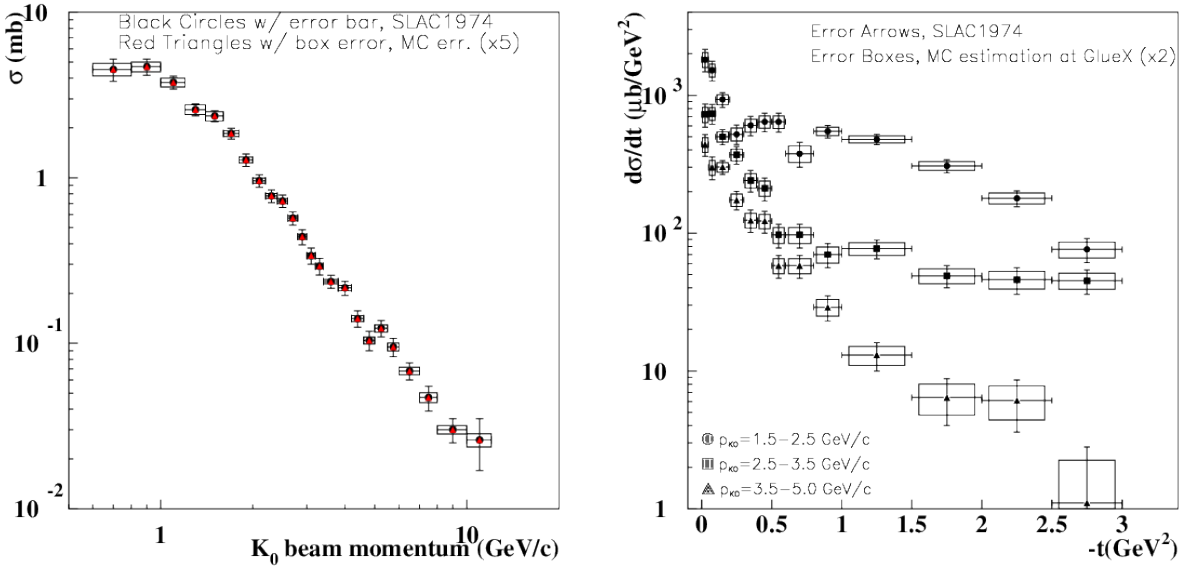

Figure 39: Left panel: The total cross-section uncertainty estimate (statistical uncertainty only) for $K_Lp \to \pi^+\overline{\Lambda}$ reaction as a function of K_L beam momentum in comparison with SLAC data [168]. The experimental uncertainties have tick marks at the end of the error bars. The box-shaped error bars in the MC points from K_L beam at GlueX were increased by a factor of 5.The differential cross-section as a function of t for three beam momentum bins from SLAC data. The box-shaped error bars in the MC points from K_L beam at GlueX detector were increased by a factor of 2. Right panel: The t-dependent cross-sections in three beam momentum bins (same as SLAC data sets): p_{K^0}=1.5-2.5 GeV/c (solid bullets), p_{K^0}=2.5-3.5 GeV/c (solid rectangles)and p_{K^0}=3.5-5.0 GeV/c (solid triangles).

1. $K_Lp \to K^+\Xi^0$ Reaction

   Several topologies can be used to reconstruct $K_Lp \to K^+\Xi^0$ events, thereby enhancing the available statistics. The biggest contribution results from requiring the reconstruction of only the K^+ in the final state and reconstructing the reaction using the missing-mass technique. The Ξ^0 decays almost 100% of the time to $\pi^0\Lambda$. By utilizing the large branching ratios for $\Lambda \to \pi^-p$ and $\pi^0 \to \gamma\gamma$ decays, we can also fully reconstruct the Ξ^0s in the final state using the four-momenta of the detected final-state particles. Figure 41 shows the expected W resolution for this reaction with the ToF-method (black) and when W is determined from all detected final-state particles (blue).

   In 100 days of beamtime, we expect 3×10^6 $K_Lp \to K^+\Xi^0$ events. From this, the available reconstructed events expected is 2×10^6 for Topology 1 $K_Lp \to K^+X$, 1×10^5 for Topology 2 $K_Lp \to K^+\Lambda X$, and 2×10^4 for Topology 3 $K_Lp \to K^+\Xi^0$. Figure 42 compares the statistical uncertainties of the total and differential cross sections for the reaction $K_Lp \to K^+\Xi^0$ with existing data taken from [169] for the three different topologies (column 1: only K^+ reconstructed, column 2: $K^+\Lambda$ reconstructed, and column 3: $K^+\Xi^0$ reconstructed).

   These statistics also allow us to determine the cascade induced polarization by utilizing the

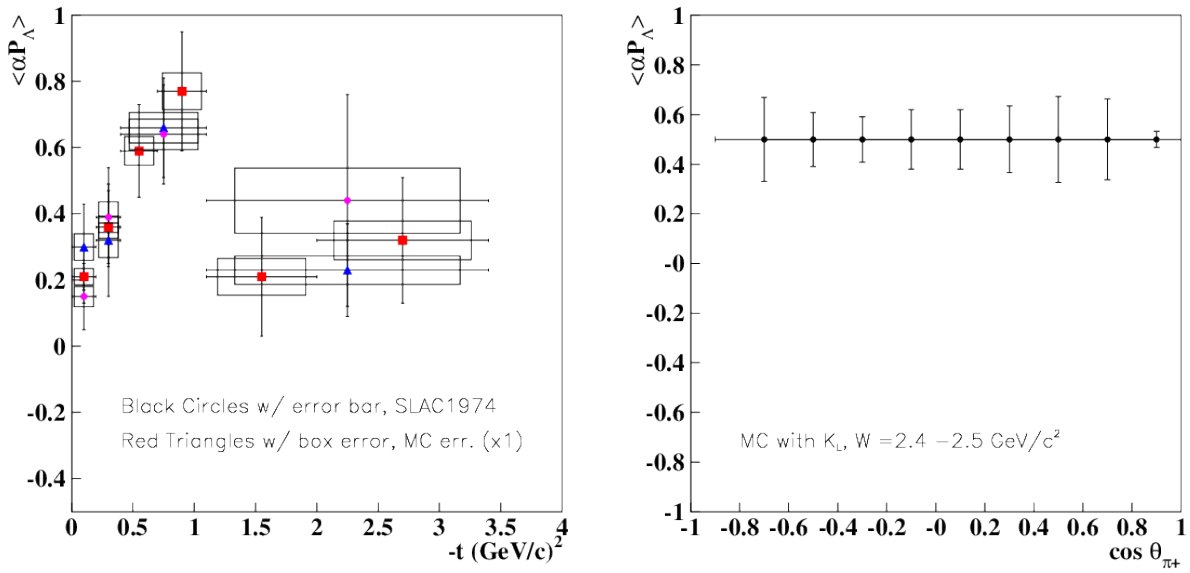

Figure 40: Left panel: The averaged polarization, $\langle \alpha P_\Lambda \rangle$ as a function of the beam momentum, p_{BEAM} from Ref. [168], $p_{K^0} > 2.5$ GeV/c (red boxes), $p_{K^0} = 2.5 - 3.8$ GeV/c (blue triangles) and $p_{K^0} > 3.8$ GeV/c (purple bullets). The experimental uncertainties have tick marks at the end of the error bars. The box-shaped error bars from the MC for the K_L beam at GlueX, assuming 100 days beamtime. $\alpha = 0.645$ is Λ analysing power. Right panel: Estimates of the statistical uncertainties of the Λ polarization as a function of $\cos\Theta_{\pi^+}$ for the $W = 2.4 - 2.5\ GeV/c^2$ energy bin.

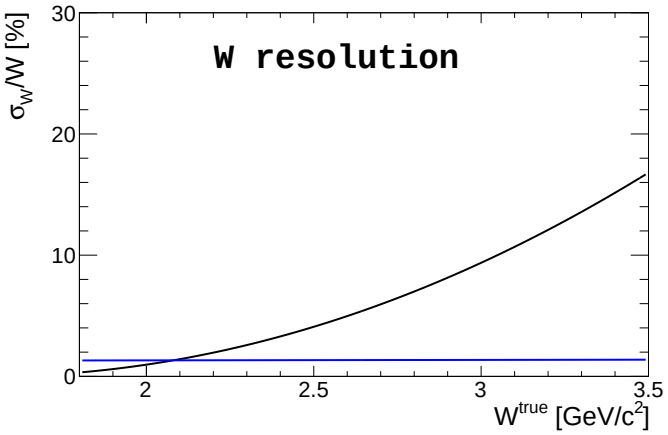

Figure 41: W resolution of $\sigma W/W$, for the time-of-flight method (black) and when W is determined from all detected final-state particles (blue).

fact that the cascade is self-analyzing with an analyzing power of -0.406 [2]. Figure 43 shows the statistical uncertainty estimates of the induced polarization of the cascade by simple fits to the acceptance-corrected yields of the pion angular distribution in the Ξ^0 rest frame.

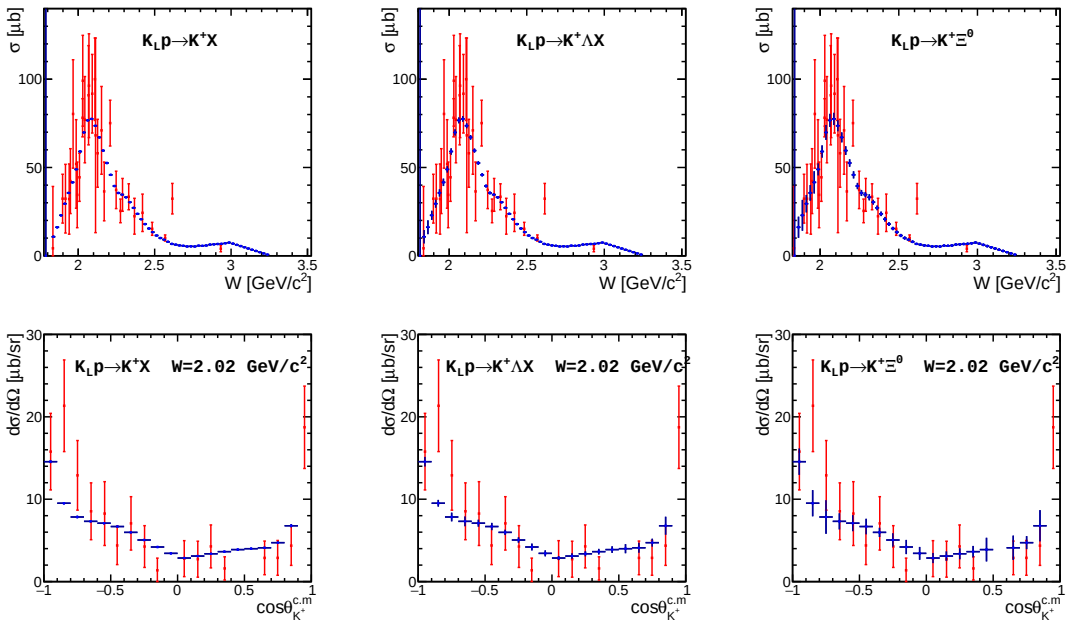

Figure 42: Total and differential cross section statistical uncertainty estimates (blue points) for the three topologies (column 1: only K^+ reconstructed, column 2: $K^+\Lambda$ reconstructed, and column 3: $K^+\Xi^0$ reconstructed) in comparison with data taken from Ref. [169] (red points).

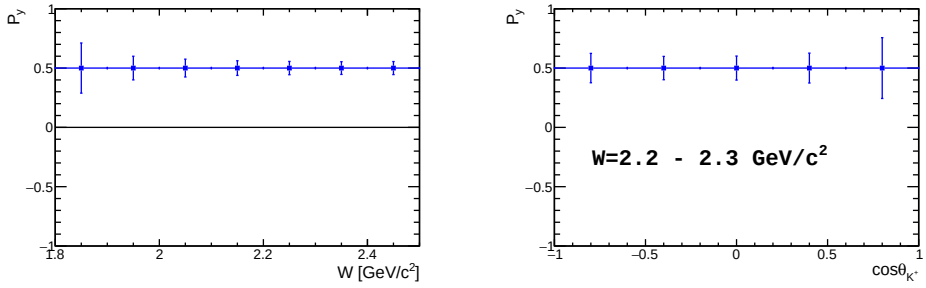

Figure 43: Estimates of the statistical uncertainties of the induced polarization of the cascade as a Left panel: function of W (one-fold differential) and Right panel: function of $\cos\theta_{K^+}$ (two-fold differential).

The main background for this reaction would come from the reactions $K_Lp \to K^+n$ and $K_Lp \to \pi^+\Lambda$, where the π^+ is misidentified as a kaon. The former reaction has an order-of-magnitude higher cross section than $K_Lp \to K^+\Xi^0$; however, the W resolution below 2.5 GeV/c^2 allows a clean separation of these two reactions. Detection and reconstruction of the Λ places additional constraints that reduce any background contributions significantly. Neutron-induced reactions are not expected to contribute significantly to background and, with missing-mass, invariant-mass, and time-of-flight cuts, such background contributions can be eliminated.

The KL Facility can be utilized to study excited cascade states $K_Lp \to K^+\Xi^*$ with $\Xi^* \to$

$\pi\Xi$ and $\Xi^* \rightarrow \gamma\Xi$. These excited states should be easily identified and isolated using the missing-mass and invariant-mass techniques. A double-moment analysis can be employed by reconstructing the entire decay chain and establish the spin and parity of these excited states [170].

2. $K_L n \rightarrow K^+\Xi^-$ Reaction

The analysis of reaction on the neutron is based on the same approach as the one described above for $K_L p \rightarrow K^+\Xi^0$. The main difference comes from the momentum distribution of the target nucleon. This can be easily addressed by selecting exclusive events; that is requiring the detection of all final state particles, and namely the positive kaon, the negative pion from the cascade decay and the proton and negative pion from the Λ decay. Even though this reduces the available statistics, the W resolution is kept at small values.

Based on the models described in Sec. 8, polarized data on the reaction $K_L n \rightarrow K^+\Xi^-$ were generated. In 100 days of beamtime, we expect several million events (between 3 and 10) depending on the two available solutions, which give very different predictions. From this, the reconstructed events expected is 7×10^4 or 3×10^5 for the fully exclusive reaction. In the same manner as the reaction on the proton ($K_L p \rightarrow K^+\Xi^0$), we will utilize the fact the the cascade is self-analyzing with an analyzing power of -0.458 [2]. The statistical uncertainties obtained over a period of 100 days for the induced cascade polarization are illustrated in Fig. 44.

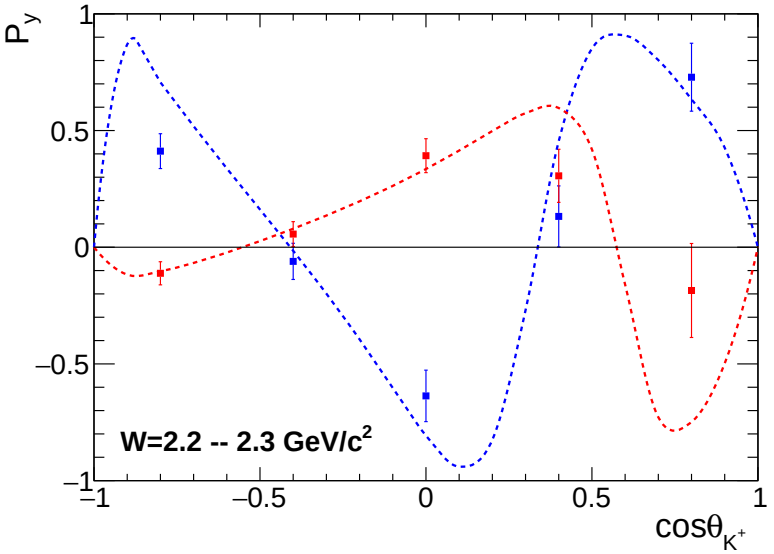

Figure 44: Estimates of the statistical uncertainties of the induced polarization of the Ξ^- as a function of $\cos\theta_{K^+}$ (two-fold differential). The curves show the theoretical predictions based on two solutions as described in Sec. 8.

It is evident that the determination of P_y will place very stringent constraints on the available models. The statistical uncertainties obtained over a period of 100 days are sufficient to investigate the underlying dynamics and cleanly differentiate between leading theoretical predictions.

The exclusivity of the reaction allows us to obtain a much cleaner sample of events with minimal background contributions. This will be done by requiring the invariant mass of the proton and the two negative pions to be consistent with the mass of Ξ^-. An additional requirement on the invariant mass of the proton-pion pair to be consistent with the mass of the Λ will eliminate any background contributions other than the excited cascade channels. Contributions from excited cascade states can also be identified and removed by the application of coplanarity cuts between the strange meson and reconstructed cascade. Excited cascade states $K_L n \to K^+ \Xi^{-*}$ can also be identified, isolated, and studied in detail, using the missing-mass technique assuming the target nucleon at rest. The requirement of detection of an additional neutral pion or photon in the final state (along with the detection of the strange meson and negative cascade), allows the full reconstruction of the final state of excited cascade states and an in-depth analysis of this reaction.

11.1.5 $K_L p \to K^+ n$ Reaction

The $K_L^0 p \to K^+ n$ reaction is a very special case in kaon-nucleon scattering. Due to strangeness conservation, formation of intermediate resonances is forbidden for this reaction. The main contribution comes from various non-resonant processes, which can be studied in a clean and controlled way. Similar non-resonant processes can be seen in other reactions where they can interfere with hyperon production amplitudes, causing distortion of the hyperon signals. That is why knowledge of the non-resonant physical background is important not only for the kaon-induced reactions but for all reactions with strangeness. The non-resonant nature of the reaction does not guarantee the absence of bumps in the total cross section: kaons and/or nucleons can be excited in the intermediate stage, producing bumps in the total cross section.

The reaction $K_L^0 p \to K^+ n$ is simple and it has a very high production cross section (see Fig. 45); nevertheless, the data on this reaction are scarce. It is a bit simpler to perform a positive kaon beam scattering for the inverse reaction, but the necessity of a neutron target with unavoidable many-body and FSI effects complicates the data analysis. That is why the inverse reaction is also not so well known. A fair amount of differential cross-section data are available in the range $0.5 < p_{K_L} < 1.5$ GeV/c, predominantly from bubble chambers, see Ref. [171], and there are a few measurements at high momenta: $p_K = 5.5$ GeV/c [172], $p_K = 10$ GeV/c [173]. In the energy range $2 < W < 3.5$ GeV, which can be covered by the KLF experiment with very high statistics, there are no data on this reaction at all.

It is enough to detect charged kaon to reconstruct the reaction fully via the missing mass technique. If the beam energy is determined by TOF method utilizing the 24 m flight path between the kaon production Be target and the reaction hydrogen target, the beam resolution is driven by the ST time resolution (Sec. 3).

In addition to a kaon, one could also detect a neutron; however, due to poor neutron detection efficiency and the large systematic uncertainties associated with neutron detection we do not expect any improvement in reaction reconstruction in this case.

In 100 days of beamtime we expect to detect around 60M $K_L p \to K^+ n$ events. A typical example of the expected statistics in comparison to previous data can be seen in Fig. 46 (left). The highest

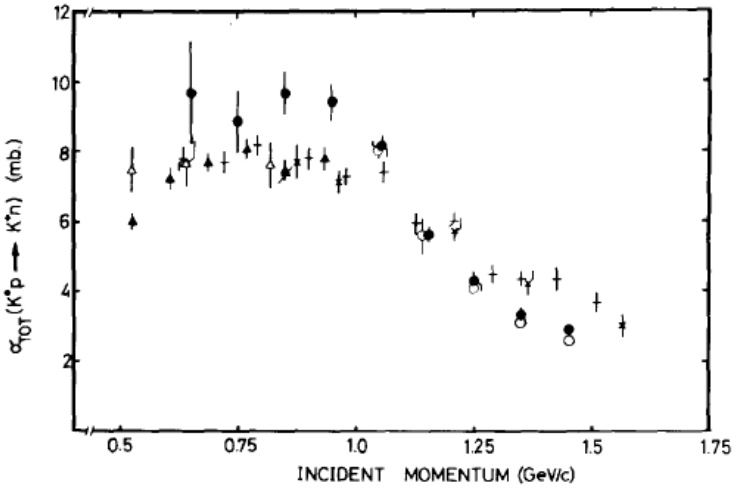

Figure 45: The total cross section for $K_L p \to K^+ n$ reaction as a function of K_L-momentum from Ref. [171]

flux is expected around $W = 3$ GeV, where we had to increase statistical errors by a factor of 10 to make them visible (see Fig. 46 (right)).

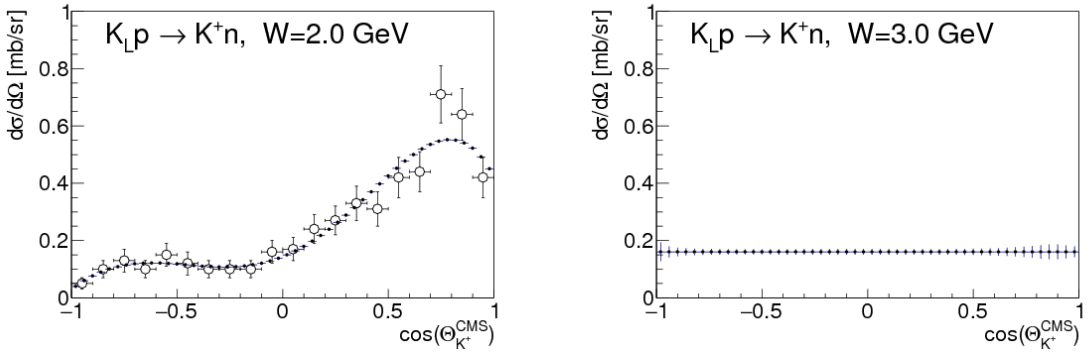

Figure 46: Left panel: The cross-section uncertainty estimates (statistical only) for $K_L p \to K^+ n$ reaction for the $W = 2$ GeV. Right panel: In comparison with data from Ref. [171] and $W = 3$ GeV. The error bars for the right plot were increased by factor of 10 to make them visible.

There are three major sources of background: $np \to K^+ nn$, $np \to \pi^+ nn$, and $K_L p \to K^+ \Xi^0$. Neutron flux drops exponentially with energy (see Appendix A4 (Sec. 16) for details) and generally the high-energy neutron flux is tiny. A detailed description of various backgrounds can be found in Appendix A5 (Sec. 17).

11.1.6 Reaction $K_L p \to K^- \pi^+ p$

1. **I=1/2 P-wave Phase Shift Analysis**

The $K\pi$ S-wave scattering, below 2 GeV, has two possible isospin channels, $I = 1/2$ and $I = 3/2$. In the same range of mass, the P-wave has one isospin, $I = 1/2$. The P-wave is a narrow elastic wave peaking at 892 MeV and interpreted as $K^*(892)$. The $I = 3/2$ S-wave is elastic and repulsive up to 1.7 GeV and contains no known resonances. In the $I = 1/2$ S-wave, a peaking broad resonance appears above 1350 MeV. Moreover, some phenomenological studies [174–178] predict the presence of a resonance with a very large width in the region close to the $K\pi$ threshold. The hadroproduction of the $K\pi$, using the K_L facility, provides an adequate environment for studying the K^* states.

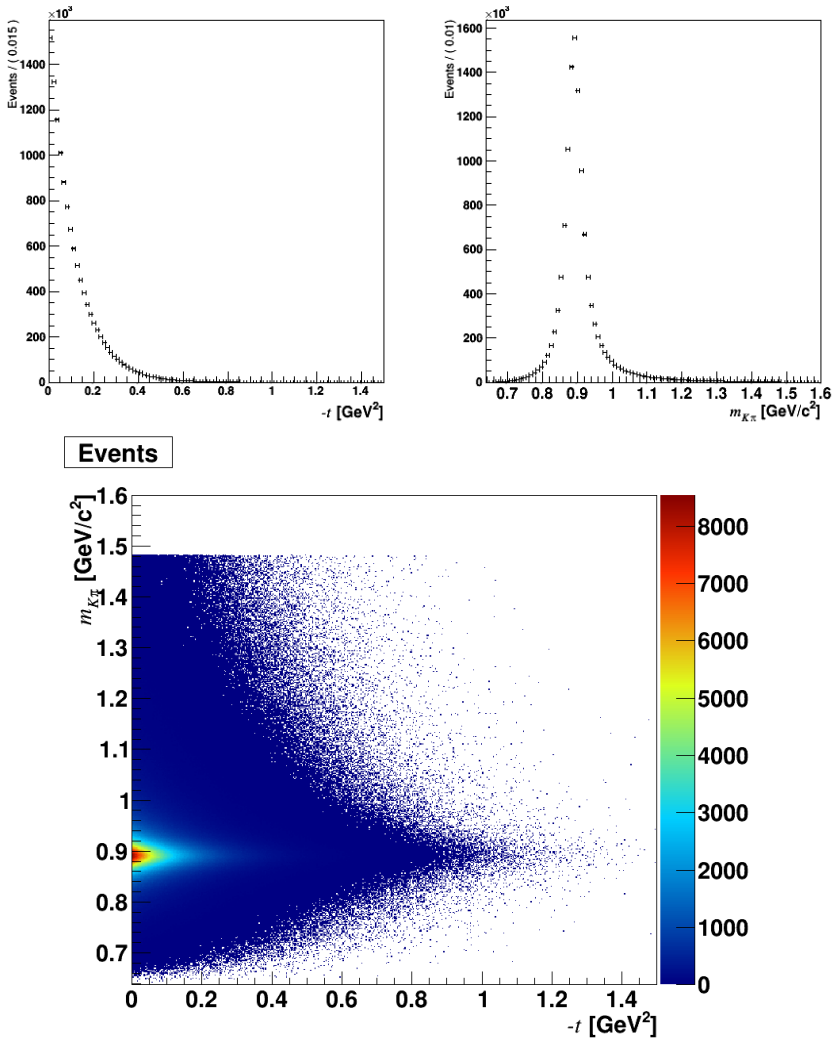

Figure 47: Top left panel: The generated MC events distribution function of $-t$. Top right panel: $m_{K\pi}$. Low panel: $m_{K\pi}$ vs $-t$.

We made MC simulations to study the phase-shift of the $K\pi$ P-wave in the K_L facility. The $K\pi$ production simulation is based on the model given by Estabrooks et al. [113]. The model describes the charged kaon reaction $K^-p \to K^-\pi^+n$. Therefore in this simulation we assume that the cross-section of $K^0_Lp \to K^-\pi^+p$ is similar to the previous reaction. The

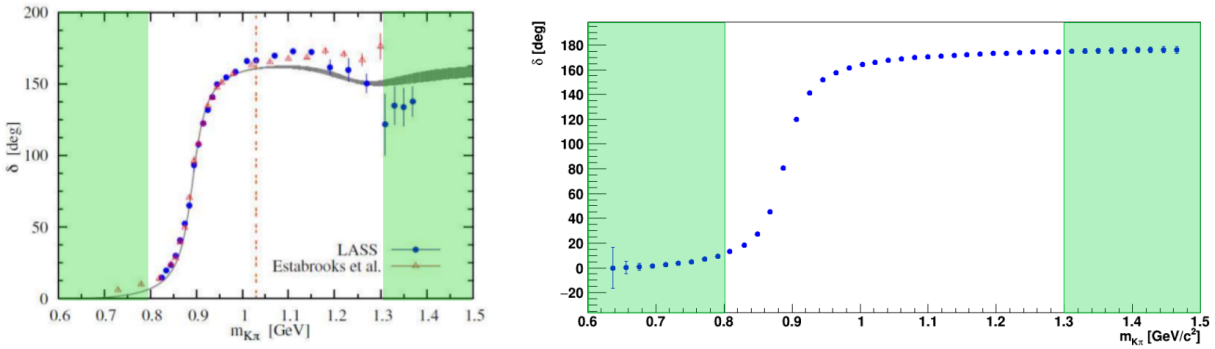

Figure 48: The $I = 1/2$ $K\pi$ scattering P-wave phase-shift function of $m_{K\pi}$. Left panel: Experimental results from LASS [111] and Estabrooks *et al.* [113]. The gray band represents the fit to the τ decay data by Boito *et al.* [115] Right panel: Results of expected measurement for 100 days of running. The statistical errors on the right panel are increased by factor of 10 for a better visibility.

model describes the production mechanism in terms of strongly degenerate π-B and ρ-$A2$ Regge exchanges and Regge "cuts" that have simple structure in the t-channel helicity frame. The t-dependent parametrization of the naturality amplitudes $L^{\pm}_{\lambda}$ for production of a $K^-\pi^+$ state of invariant mass $m_{K\pi}$, center-of-mass (CM) momentum q, angular momentum L, and t-channel helicity λ, by natural $(+)$ and unatural $(-)$ parity exchange, according to [113], is as follows

$$L_0 = \frac{\sqrt{-t}}{m_\pi^2 - t} G^L_{K\pi}(m_{K\pi}, t) \,, \tag{27}$$

$$L^-_1 = \sqrt{\frac{1}{2}L(L+1)}\, G^L_{K\pi}(m_{K\pi}, t)\gamma_c(m_{K\pi}) \exp(b_c(m_{K\pi})(t - m_\pi^2)) \,, \tag{28}$$

$$\begin{aligned} L^+_1 &= \sqrt{\frac{1}{2}L(L+1)}\, G^L_{K\pi}(m_{K\pi}, t)[\gamma_c(m_{K\pi}) \exp(b_c(m_{K\pi})(t - m_\pi^2)) \\ &- 2i\gamma_a(m_{K\pi}) \exp(b_a(m_{K\pi})|t'|(t - m_\pi^2))] \,, \end{aligned} \tag{29}$$

$$L^{\pm}_{\lambda} = 0 \,, \qquad \lambda \geq 2 \,, \tag{30}$$

where $G^L_{K\pi}$ is related to the $K\pi$ elastic scattering amplitude a_L by

$$G^L_{K\pi}(m_{K\pi}, t) = N \frac{m_{K\pi}}{\sqrt{q}} a_L(m_{K\pi}) \exp(b_L(m_{K\pi})(t - m_\pi^2)). \tag{31}$$

The parameters γ_a, γ_c, b_a, b_c and b_L were determined by fitting the LASS $K^-p \to K^-\pi^+n$ data. The $K\pi$ scattering amplitudes are the sum of an isospin-$1/2$ and $3/2$ component,

$$a_L = a_L^{I=1/2} + \frac{1}{2} a_L^{I=3/2} \,, \tag{32}$$

where a^I_L is described by a relativistic BW.

In this study, we include only the P-wave component $K^*(892)$ in the simulation. The number of events for 100 days of running in the range of mass $m_{K\pi} < 1.5$ GeV and negative

transfer 4-momentum $-t < 0.8$ GeV^2, is expected to be around 2 million events. The K_L beam energy used in this simulation is equal to 7 GeV. The generated MC events, function of the transfer 4-momentum $-t$ and the invariant mass $m_{K\pi}$, is illustrated in Fig. 47, and the phase-shift function of $m_{K\pi}$ with mass bin width of 10 MeV and $|t| < 0.5$ GeV^2 is illustrated in Fig. 48.

As one can see experimental data produced by LASS experiment [111] in the mass regions close to the threshold and above 1.3 GeV are poorly measured and therefore do not provide constrains in these regions. However, according to this simulation study, the proposed K_L facility can provide statistically high precision data, which will significanlty constrain the uncertainty of the phase motion in the full range of $m_{K\pi}$ from the threshold up to 1.5 GeV.

11.2 Toy PWA for Spectroscopy of Hyperons

Our strategy is not a naive "hunting for bumps". Instead, we will perform coupled-channel partial-wave analyses (PWAs) using measured differential cross sections and recoil observables (see Sec. 7). Then we will look for poles in the complex energy plane to identify hyperon resonances (see Appendix A2 (Sec. 14)).

The existing K_Lp database is so poor that PWAs of individual K_Lp induced reactions may not be possible based on currently available data. In particular, there are no $K_Lp \to K^+\Xi^0$ polarization data available and there is only one energy for $K_Lp \to \pi^+\Lambda$ at which there are $d\sigma/d\Omega$ and polarization data. Our proposal does not consider the use of a polarized target and, for that reason, we will be able to measure polarization data for recoil observables only. Overall, one certainly cannot perform a reliable PWA for reactions in which only $d\sigma/d\Omega$ data are available. The existing K_Ln database is nonexistent.

To estimate the impact that new K_L measurements will have on fits, we have carried out a study using a toy model based on a PWA of π^+p elastic scattering. This reaction was chosen in part because it is isospin selective as are most of the K_Lp reactions we propose to measure. Our method is similar to that used by the GW group in the FROST proposal for pion photoproduction [267]. Using the recent SAID WI14 solution [268], we generated pseudodata for $\pi^+p \to \pi^+p$ $d\sigma/d\Omega$ and recoil polarization P. The pseudodata were generated for our worse case of statistics and for a $K_Lp \to K^+\Xi^0$ binning of 20 MeV in c.m. energy W in the second resonance region W = 1400 - 1800 MeV and θ = 5 (10) 175° for $d\sigma/d\Omega$ and $\cos\theta = -0.80$ (0.4) 0.8 for P. A series of single-energy solutions (SES) were then fitted using settings associated with 100 days of running time: $\sigma(d\sigma/d\Omega)$ = 1% with $\sigma(P)$ = 0.1. We also carried out a series of SES using settings associated with 20 days of running time: $\sigma(d\sigma/d\Omega)$ = 5% with $\sigma(P)$ = 0.5.

To facilitate the comparisons, we have summarized the effect on individual partial-wave amplitudes by computing the ratio of uncertainties for 20 and 100 days data vs. SES associated with WI14 [268]. A plot of the average ratios (SES for 20 and 100 days vs. SES associated with WI14 (a fit of the world database) is presented in Fig. 49. Here we see a particular improvement through the inclusion statistics from 20 to 100 days. The greatest effect naturally requires a measurement of all available quantities, but the 100 days provides a great benefit for partial waves with $l > 1$.

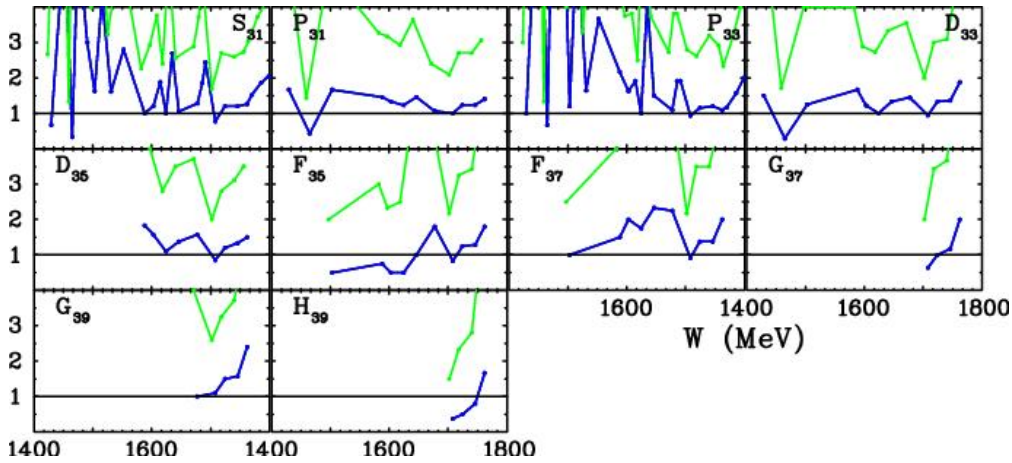

Figure 49: Average ratio of the uncertainties of partial-wave amplitudes of the proposed data individually for the two settings 20 days (green) and 100 days (blue) (SES for 20 and 100 days vs. SES associated with WI14 (a fit of the world database).

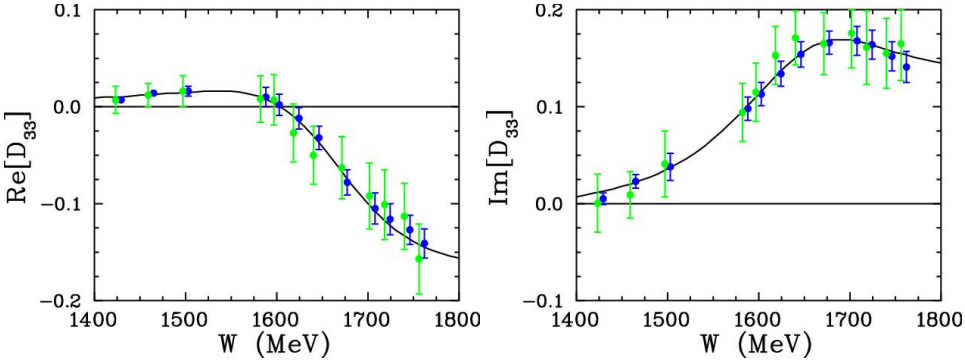

Figure 50: Real (left) and imaginary (right) part of the D_{33} amplitude. Comparison between SAID WI14 (black solid curve) along with 100 days SES (blue filled circles) and 20 days SES (green filled circles).

We employed both single-energy and energy-dependent solutions over a variety of energy ranges to estimate uncertainties. In Fig. 50, we present a specific example for the D_{33} partial wave that shows how the proposed measurements can reduce uncertainties. The proposed measurements will clearly have a greater sensitivity to structures that might be missed by lower statistics data. Figures 51 and 52 show the impact of the proposed data on the SAID SES. The new measurements will significantly reduce the uncertainties of the observables. The total angular resolution will therefore be greatly improved, which will enhance the possibility of determining the number of amplitudes that are involved. With this greater understanding of these observables, effects of higher-spin resonances can be investigated.

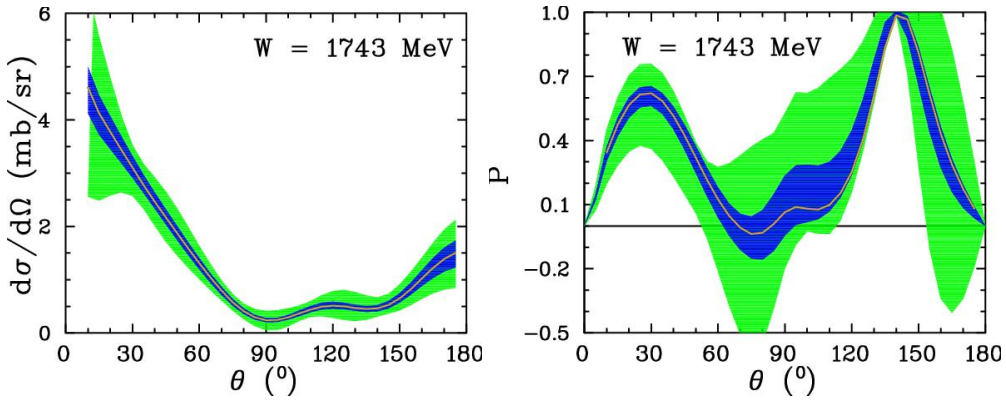

Figure 51: Two examples (W = 1743 MeV) showing the impact of the proposed data on the SAID SES. The green (blue) hatched band indicates the present uncertainties in the SES for 20 (100) days. The yellow solid curve corresponds to the SAID WI14 solution.

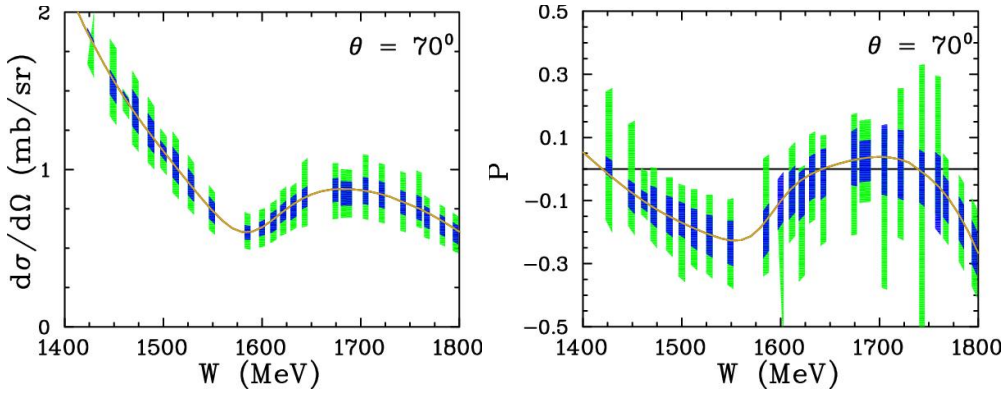

Figure 52: Two more examples (θ = 70°) showing the impact of the proposed data on the SAID SES. The green (blue) hatched band indicates the present uncertainties in the SES for 20 (100) days. The yellow solid curve corresponds to the SAID WI14 solution.

11.3 Summary and Beam Time Request

We propose to perform strange hadron spectroscopy with a secondary K_L beam in the GlueX setup at JLab. Precise new experimental data (both differential cross sections and recoil polarization of hyperons) for K_Lp scattering with good kinematic coverage will be obtained. This will allow predictions from CQM and LQCD to be checked for all families of excited Λ^*, Σ^*, Ξ^*, and Ω^* hyperon resonances for the first time. In addition, it will permit a search for the possible existence of hybrids in the hyperon sector as predicted by the lattice calculations [60].

A complete understanding of three-quark bound states requires accurate measurements of the full spectra of hyperons with their spin-parity assignments, pole positions, and branching ratios. An important impact of these strange hyperon spectroscopy measurements is their significance for the thermodynamic properties of the early universe at freeze-out, which is one of the main physics topics at heavy-ion colliders.

Besides hyperon spectroscopy, the experimental data obtained in the strange meson sector in the reactions $K_L p \to K^{\pm}\pi^{\mp}p$ and $K_L p \to K_S\pi^{\pm}n(p)$ will provide precise and statistically significant data for experimental studies of the $K\pi$ system. This will allow a determination of quantum numbers of strange meson resonances in S- (including $\kappa(800)$), P-, D-, and higher-wave states. It will also allow a determination of phase shifts to account for final-state $K\pi$ interactions. Measurements of $K\pi$ form factors will be important input for Dalitz-plot analyses of D-meson and charmless B mesons with $K\pi$ in final state. These will be important inputs for obtaining accurate an value of the CP-violating CKM matrix element V_{us} and testing the unitarity relation, in particular through the measurement of the $\tau \to K\pi\nu_\tau$ decay rate.

The approval and construction of the proposed facility at JLab will be *unique in the world*. The high-intensity secondary beam of K_L (1×10^4 K_L/s) would be produced in electromagnetic interactions using the high-intensity and high-duty-factor CEBAF electron beam with very low neutron contamination as was done at SLAC in the 1970s; but now, with three orders of magnitude higher intensity [168]. The possibility to perform similar studies with charged kaon beams is under discussion at J-PARC with intensities similar to those proposed for the K_L beam at JLab. If these proposals are approved, the experimental data from J-PARC will be complementary to those of the proposed K_L measurements.

Below in Table 3, we present the expected statistics for 100 days of running with a LH_2 target in the GlueX setup at JLab. The expected statistics for the 5 major reactions are very large. There are however, two words of cautions at this stage. These numbers correspond to an inclusive reaction reconstruction, which is enough to identify the resonance, but might not be enough to uncover its nature. The need for exclusive reconstruction to extract polarization observables further decrease the expected statistics, e.g., from 2M to **200k** events in the $K\Xi$ case. These statistics, however, would allow a precise measurement of the double-differential polarization observables with statistical uncertainties on the order of 10%. Secondly, kaon flux has a maximum around $W = 3$ GeV, which decreases rapidly towards high/low W's. Thus, the 100 days of beam time on the LH_2 are essential to maximize the discovery potential of the K_L Facility and cover the densely populated hyperon regime at low-W. Fig. 53 shows how polarisation observables uncertainty develops for various W and experimental lengths.

Table 3: Expected statistics for differential cross sections of different reactions with LH_2 and below $W = 3.5$ GeV for 100 days of beam time.

Reaction	Statistics (events)
$K_L p \to K_S p$	2.7M
$K_L p \to \pi^+\Lambda$	7M
$K_L p \to K^+\Xi^0$	2M
$K_L p \to K^+ n$	60M
$K_L p \to K^-\pi^+ p$	0.7M

There are no data on “neutron" targets and, and for this reason, it is hard to make a realistic estimate of the statistics for $K_L n$ reactions. If we assume similar statistics as on a proton target, the full program will be completed after running 100 days with LH_2 and 100 days with LD_2 targets.

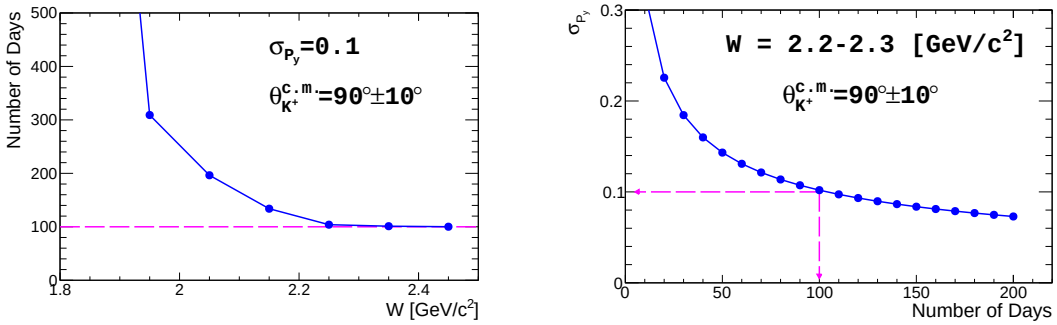

Figure 53: Required length of experiment for the $K_L p \to K^+ \Xi$ reaction. Left panel: to reach 10% polarization uncertainty as a function of W. Right panel: Reachable polarization uncertainty at $W = 2.2$ GeV and $\theta^{CM}_{K+} = 90°$.

12 Cover Letter for KLF Proposal Submission to PAC46

This Proposal follows the Proposal PR12–17–001, *Strange Hadron Spectroscopy with a Secondary K_L beam at GlueX* presented to PAC45 in 2017. The Issues and Recommendations included in the PAC45 Final Report document read as follow:

Issues: *Mounting this experiment will transform the existing Hall D beamline, so it represents an almost irreversible change in direction for the GlueX apparatus. As such, the physics driver must be compelling, and the PAC doesn't feel that a sufficiently convincing physics case has been made. A broad program is suggested, so the PAC would welcome a larger presentation format along the lines of a run group proposal.*

The CPS design is progressing but details on the KL target and shielding for the detector need to be fleshed out. The 64 ns beam structure will also require study to ensure that other halls are not adversely affected.

The beam time request is dominated by the hyperon polarimetry measurements. A simulated example of a PWA, and how it would feed into the proposed spectroscopy measurements, will be needed in a future proposal.

The LOI included doubly strange baryons but this topic was not much expanded upon in the proposal. This topic remains of considerable interest.

Summary: *This experiment would introduce a new and interesting area of physics at JLAB. The PAC recommends that the collaboration work with the lattice and theoretical nuclear physics community to sharpen the physics case. In addition, more details on the KL production target and shielding will be needed before we can fully assess the feasibility of the experiment. Despite the progress made in delineating the expanded physics possibilities, the very substantial beam time request would be better motivated if more details could be provided on its impact on the proposed spectroscopic measurements.*

The KLF Collaboration for the GlueX Collaboration believes that the current proposal addresses

all the concerns following the recommendations expressed by the PAC45:

1. **Q1:** *Mounting this experiment will transform the existing Hall D beamline, so it represents an almost irreversible change in direction for the GlueX apparatus.*
   A1: According to our preliminary studies, switching from KL to photon beam mode may take from 4 to 5 months depending on the details of realization of the beamline as the TAC Physics Report for PAC45 said. Changeover from the photon to K_L beamline and from the K_L beamline to photon is expected to take less or about 6 months (after the radiological cooldown). This break fits current the CEBAF Accelerator schedule well and the beam collimator cave has enough space (4.52 m width) for the Be-target assembly out of the beamline.

2. **Q2:** *As such, the physics driver must be compelling, and the PAC doesn't feel that a sufficiently convincing physics case has been made. A broad program is suggested, so the PAC would welcome a larger presentation format along the lines of a run group proposal.*
   A2: With the current proposal, we aim to show broad range of outstanding problems related to the strange hadron spectroscopy, which can be solved and improve existing database by orders of magnitude. We believe, the run group proposals may naturally occur when the proposed facility is approved. In particular, we are focusing on doubly strange baryons studies and pion-kaon interactions. Following Robert McKeown's suggestion, we plan to have three presentations on the PAC46 meeting:

   (a) *K_L Beam Facility at GlueX;*

   (b) *Hyperon Spectroscopy with a K_L Beam;*

   (c) *Strange Mesons with a K_L Beam.*

3. **Q3:** *The CPS design is progressing but details on the KL target and shielding for the detector need to be fleshed out.*
   A3: Following to that, we improve a conceptual design of both the CPS (Sec. 10.1.2) and KL (Be) target (Sec. 10.1.3).

   (a) The JLab CPS Working Group has considered the CPS case for Halls C in detail. The recent HIPS2017 Workshop (February 2017) aimed at producing an optimized photon source concept with potential increase of scientific output at Jefferson Lab, and at refining the science for hadron physics experiments benefitting from such a high-intensity photon source. A 30 kW CPS has been designed by an CPS working group for Halls C/A. The group intends to provide the design for a 60 kW device for Hall D. The latter device has to be somewhat larger, but the Tagger hall provides more available space than the Hall C location.

   (b) Our MC studies show that the Be-target assembly conceptual design satisfies the RadCon requirement. The full engineering design is pending approval.

4. **Q4:** *The 64 ns beam structure will also require study to ensure that other halls are not adversely affected.*
   A4: According to our discussions with accelerator experts (Geoff Krafft, Matt Poelker, Todd Satogata, and Jay Benisch) following the iTAC Report for PAC45 it has been explicitly

stated that no problems are expected for a 64 ns beam structure from beam delivery point of view. Geoff is a member of our team and we do have a Section 10.1.1 addressed to this task. Let us add what Matt Poelker's (polarized electron source expert at CEBAF) already noted in our responce to the TAC Physics Report *...it is rather challenging to generate a 15.6 MHz repetition rate beam for the required 64 ns bunch spacing. Specifically, our fiber laser amplifiers that produce the light delivered to the photocathode become damaged at this low repetition rate. We learned this through painful experience, damaging $\sim$ equipment that cost about \$50k to replace. On the bright side, fiber amplifiers can be purchased that are designed to operate at low repetition rate (i.e., higher peak power), but he just wanted to tell us that we don't presently have them. We would need to purchase some optical equipment to generate your requested bunch repetition rate. I don't know the exact cost but probably less than $\sim$\$100k. So just a speed bump, not a show-stopper.*

5. **Q5:** *A simulated example of a partial wave analysis, and how it would feed into the proposed spectroscopy measurements, will be needed in a future proposal.*
   A5: We generated quasi-data for the toy PWA model for spectroscopy of hyperons to demonstrate impact of the proposed experiment on the world knowledge (Sec. 11.2).

6. **Q6:** *The LOI included doubly strange baryons but this topic was not much expanded upon in the proposal. This topic remains of considerable interest.*
   A6: We made two cases with doubly strange baryons (Sec. 3.1) and pion-kaon interactions (Sec. 9) more compelling.

7. **Q7:** *The PAC recommends that the collaboration work with the lattice and theoretical nuclear physics community to sharpen the physics case.*
   A7: We are collaborating closely with the lattice and theory community. In addition, we had the forth Workshop PKI2018 (February 2018) hosted at JLab recently and dedicated to the physics of strange mesons produced by the neutral kaon beam. Meanwhile, many lattice and theory researchers are co-authors of our proposal and our proposal has a significant contribution from them.

8. **Q8:** *In addition, more details on the KL production target and shielding will be needed before we can fully assess the feasibility of the experiment.*
   A8: All is done (see **A3**).

9. **Q9:** *Despite the progress made in delineating the expanded physics possibilities, the very substantial beam time request would be better motivated if more details could be provided on its impact on the proposed spectroscopic measurements.*
   A9: We believe that the current proposal addresses all the concerns following the recommendations expressed by the PAC45.

13 Appendix A1: Analysis of Three-Body Final States

The understanding of baryon properties is hardly possible without an analysis of reactions with two mesons in the final state. Already in the mass region above 1600 MeV, the excited Λ hyperons

decay strongly into the $\pi\Sigma(1385)$ [179, 180] final state while the Σ-hyperons decay strongly into the $\pi\Sigma(1385)$ [179] and $\pi\Lambda(1405)$ [181] channels. Above 1800 MeV almost all known Λ and Σ hyperons have a dominant decay mode defined by production of the vector meson $K^*(892)$ [180]. In the Σ-sector, a number of resonances were seen in an analysis of the $\overline{K}\Delta(1230)$ final state. It is natural to expect the decay of $J^P = 3/2^+$ states into the $\pi\Lambda(1520)$ [182] channel.

Reactions with two-meson final states provide vital information for the analysis of single-meson production reactions. The singularities that correspond to the opening of the resonance-meson threshold (branching points) can produce structures in other channels that can simulate a resonance-like signal [183, 184]. The situation is notably more severe in the hyperon sector than in the sector of non-strange baryons. Due to the rather small widths of low-mass excited hyperons and meson resonances with an s-quark, such singularities are situated much closer to the physical region and can notably influence the data. Therefore, a combined analysis of the channels with single and two mesons in the final state is a must in the search for the missing resonances.

Two- and three-body channel approach for the strangeness sector have already been formulated by the Jülich [185] and ANL-Osaka [95, 96] groups. Note the recent progress in the understanding of three-body unitarity that can be used to formulate conceptually improved partial-wave amplitudes [186].

The combined analysis should help us to understand the structure of resonances with masses up to 2.5 GeV and their decay properties. One of the important tasks is to find nonet partners of the nucleon states observed in the photo-production reactions in the mass region around 1900 MeV [187]. These states have strong couplings to the $\rho(770)N$ final state and it is natural to expect that their hyperon partners can be found in an analysis of the $K^*(892)N$ channel.

The analysis of the three-body final state should be done in the framework of the event-by-event maximum likelihood method, which allows us to take into account all amplitude correlations in the multidimensional phase space. It is very important to extract the polarization observables from the decay of the final hyperons in the $KN \to \pi\pi\Lambda$ and $KN \to \pi\pi\Sigma$ reactions. One possible simplification is connected with an extraction of the $K^*(892)N$ state from the $KN \to K\pi N$ data, where the analysis can be performed in the framework of the density-matrix-elements approach. However, the analysis should take into account the rescattering of the particles in the final state; e.g., triangle diagrams that lead to logarithmic singularities in the scattering amplitude. Due to the small widths of intermediate states, such singularities can play a more important role than in the case of nucleon and Δ excitations. It would be also very important to include in the analysis the CLAS photoproduction data with $K\pi\Lambda$ and $K\pi\Sigma$ final states because there is a chance that states with a small KN coupling could be observed in these reactions.

14 Appendix A2: Determination of Pole Positions

In spite of their model dependence, partial-wave BW parameters have for quite some time been the preferred connection between experiment and QCD in hadronic spectroscopy. More recently, however, pole parameters (e.g., pole positions and residues) have justifiably become the preferred connection, and this fact has also been recognized by the Particle Data Group in recent editions of

the *Review of Particle Physics* [2]. Therefore, the extraction of pole parameters from experimental data becomes a procedure of utmost importance.

Extraction of pole parameters is usually performed in two ways: (a) in an energy-dependent way (ED) or (b) in an energy-independent procedure through single-energy PWAs (SE). In an ED procedure, one measures as many observables as possible to be close to the complete set and then fits the observables with parameters of a well-founded theoretical model that describes the reaction in question. Continuity in energy is enforced by the features of the theoretical model. In a SE procedure, one again measures as many observables as possible but attempts to extract partial waves by fitting energy-binned data independently, therefore, reducing the theoretical input. A discrete set of partial waves is obtained, and the issues of achieving continuity in energy have recently been extensively discussed either by introducing the constraints in analyticity [188] or through angle- and energy-dependent phase ambiguity [189].

In energy-dependent models, pole parameters have been extracted in various ways. The most natural way is the analytic continuation of theoretical model solutions into the complex-energy plane. Simpler single-channel pole extraction methods have been developed such as the speed plot [190], time delay [191], the N/D method [192], regularization procedures [193], and Pade approximants [194], but their success has been limited. In single-energy analyses, the situation is even worse: until recently no adequate method has been available for the extraction of pole parameters. All single-channel methods involve first- or higher-order derivatives, so partial-wave data had to be either interpolated or fitted with an unknown function, and that introduced additional and, very often, uncontrolled model dependencies.

That situation has recently been overcame when a new Laurent+Pietarinen (L+P) method applicable to both, ED and SE models, has been introduced [195–199]. The driving concept behind the single-channel (and later multichannel) L+P approach was to replace solving an elaborate theoretical model and analytically continuing its solution into the full complex-energy plane, with a local power-series representation of partial-wave amplitudes having well-defined analytic properties on the real energy axis, and fitting it to the given input. In such a way, the global complexity of a model is replaced by a much simpler model-independent expansion limited to the regions near the real-energy axis, which is sufficient to obtain poles and their residues. This procedure gives the simplest function with known analytic structure that fits the data. Formally, the introduced L+P method is based on the Mittag-Leffler expansion[2] of partial-wave amplitudes near the real-energy axis, representing the regular, but unknown, background term by a conformal-mapping-generated, rapidly converging power series called a Pietarinen expansion [3]. In practice, the regular background part is usually fitted with three Pietarinen expansion series, each representing the most general function having a branch point at x_{bp}, and all free parameters are then fitted to the chosen channel input. The first Pietarinen expansion with branch-point x_P is restricted to an unphysical energy range and represents all left-hand cut contributions. The next two Pietarinen expansions describe background in the physical range with branch points x_Q and x_R defined by the analytic properties of the ana-

[2]Mittag-Leffler expansion [200] is the generalization of a Laurent expansion to a more-than-one pole situation. For simplicity, we will simply refer to this as a Laurent expansion.

[3]A conformal mapping expansion of this particular type was introduced by Ciulli and Fisher [201, 202], was described in detail and used in pion-nucleon scattering by Pietarinen [203, 204]. The procedure was denoted as a Pietarinen expansion by Höhler in [89].

lyzed partial wave. A second branch point is usually fixed to the elastic channel branch point, and the third one is either fixed to the dominant channel threshold value.

Thus, solely on the basis of general physical assumptions about the analytic properties of the fitted process (number of poles and number and position of conformal mapping branch-points) the pole parameters in the complex energy plane are obtained. In such a way, the simplest analytic function with a set of poles and branch points that fits the input is constructed. This method is equally applicable to both theoretical and experimental input[4]

The transition amplitude of the multichannel L+P model is parametrized as

$$T^a(W) = \sum_{j=1}^{N_{pole}} \frac{g_j^a}{W_j - W} + \sum_{i=1}^{3} \sum_{k_i=0}^{K_i^a} c_{k_i}^a \left(\frac{\alpha_i^a - \sqrt{x_i^a - W}}{\alpha_i^a + \sqrt{x_i^a - W}} \right)^{k_i}, \tag{33}$$

where a is a channel index, W_j are pole positions in the complex W (energy) plane, g_i^a coupling constants. The x_i^a define the branch points, $c_{k_i}^a$, and α_i^a are real coefficients. K_i^a, $i = 1, 2, 3$ are Pietarinen coefficients in channel a. The first part represents the poles and the second term three branch points. The first branch point is chosen at a negative energy (determined by the fit), the second is fixed at the dominant production threshold, and the third branch point is adjusted to the analytic properties of fitted partial wave.

To enable the fitting, a reduced discrepancy function D_{dp} is defined as

$$\begin{aligned} D_{dp} &= \sum_{a}^{all} D_{dp}^a; \\ D_{dp}^a &= \frac{1}{2\,N_W^a - N_{par}^a} \times \sum_{i=1}^{N_W^a} \left\{ \left[\frac{\mathrm{Re}\, T^a(W^{(i)}) - \mathrm{Re}\, T^{a,exp}(W^{(i)})}{Err_{i,a}^{\mathrm{Re}}} \right]^2 \right. \\ &+ \left. \left[\frac{\mathrm{Im}\, T^a(W^{(i)}) - \mathrm{Im}\, T^{a,exp}(W^{(i)})}{Err_{i,a}^{\mathrm{Im}}} \right]^2 \right\} + \mathcal{P}^a, \end{aligned}$$

where

$$\mathcal{P}^a = \lambda_{k_1}^a \sum_{k_1=1}^{K^a} (c_{k_1}^a)^2\, {k_1}^3 + \lambda_{k_2}^a \sum_{k_2=1}^{L^a} (c_{k_2}^a)^2\, {k_2}^3 + + \lambda_{k_3}^a \sum_{m=1}^{M^a} (c_{k_3}^a)^2\, {k_3}^3$$

is the Pietarinen penalty function, which ensures fast and optimal convergence. N_W^a is the number of energies in channel a, N_{par}^a the number of fit parameters in channel a, $\lambda_c^a, \lambda_d^a, \lambda_e^a$ are Pietarinen weighting factors, $Err_{i,a}^{\mathrm{Re,\,Im}}\ldots$ errors of the real and imaginary part, and $c_{k_1}^a, c_{k_2}^a, c_{k_3}^a$ real coupling constants.

[4]Observe that fitting partial-wave data coming from experiment is even more favorable.

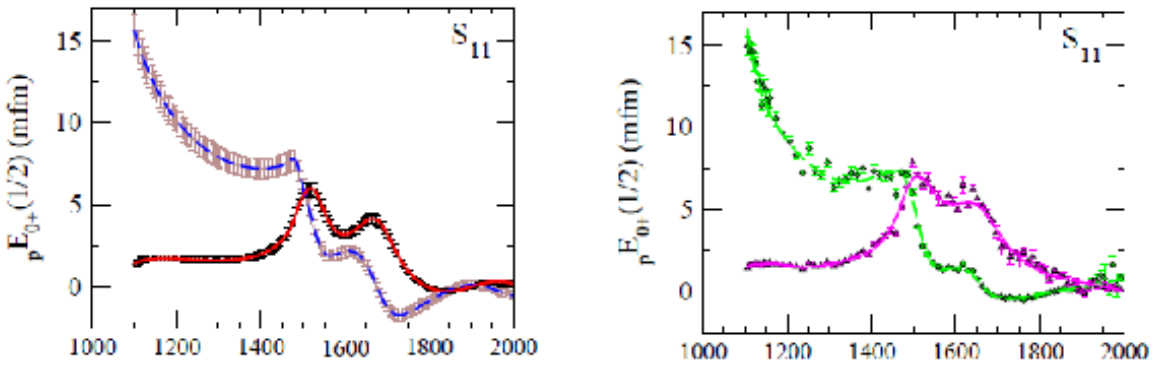

Figure 54: L+P fit to CM12 GWU/SAID pion photoproduction ${}_pE_{0+}$ ED and SE solutions [205].

In order to obtain reliable answers in the L+P model we have to build knowledge about the analytic structure of the fitted partial wave into the fitting procedure. Because we are looking for poles, we only have to define which branch-points to include. Their analytic form will be determined by the number of Pietarinen coefficients. As we have only three branch-points at our disposal we expect that the first branch-point will describe all subthreshold and left-hand cut processes, the second one is usually fixed to the dominant channel opening, and the third one is to represent background contributions of all channel openings in the physical range. So, in addition to choosing the number of relevant poles, our anticipation of the analytic structure of the observed partial wave is of great importance for the stability of the fit.

The L+P model has been successfully applied to both theoretical models and discreet partial-wave data. As an example, in Fig. 54, we give the achieved quality of the fit for the CM12 GWU/SAID pion photoproduction amplitudes [205].

In summary: Methods of the described L+P model will be used to extract pole parameters for both ED solutions, obtained by the method described in Section 7, and SE solutions developed independently.

15 Appendix A3: Statistics Tools for Spectroscopy of Strange Resonances

Several statistical aspects concerning the analysis of K_L data are discussed in the following. The proposed experiment will be capable of producing a large body of consistent data, which is a prerequisite to carry out statistical analyses. So far, the data in the strangeness $S = -1$ sector were produced in many different experiments, often from the 1980s or earlier, with different systematic uncertainties that are, moreover, unknown in many cases. The problems resemble the situation in pion-induced inelastic reactions [206, 207]. This makes any kind of analysis difficult but statis-

tical tests, e.g., on the significance of a claimed resonance signal, are indispensable to carry out meaningful baryon spectroscopy. Indeed, the search for *missing resonances* is not only a problem of implementing physical principles such as unitarity in the amplitude but also, to a large extent, a statistical one. This becomes especially relevant once one searches for states beyond the most prominent resonances.

15.1 Minimizing Resonance Content

The PWA, discussed in Section 7 is needed to extract the physically relevant information from data. For resonance spectroscopy, one needs the energy dependence of the amplitude to determine resonance positions and widths. Therefore, energy-dependent (ED) parametrizations of the partial waves are fitted either to data or to single-energy (SE) solutions, generated by conducting PWA in narrow energy bins. The resonance content is usually determined by speed-plot techniques or analytic continuation of the ED parametrization to complex scattering energies, where resonances manifest themselves as poles [208].

Yet, the ED parametrization itself contains, almost always, resonance plus background terms in one implementation or another. A problem arises if resonance terms are needed to model missing background dynamics such as triangle singularities or threshold openings in the complex plane. Then, false positive resonance signals could be obtained [183]. Adding resonance terms will always lower the χ^2 in a given fit, but the question is how significant this change is.

We plan to address this well-known, yet poorly addressed problem by applying several statistical analysis tools to the amplitude parametrization. Some techniques have been used, so far, to address this problem. For example, in so-called mass scans, the χ^2 dependence on the mass of an additional resonance is studied [209–211]. If χ^2 drops by a certain amount at a given energy, potentially in several reaction channels at once, then a resonance might be responsible.

Beyond mass scans, there exist *model selection* techniques referring to the process of selecting the simplest model with the most conventional explanation. Here, the conventional/simple explanation is an (energy-dependent) background and/or threshold cusps, while the algorithm should penalize unconventional explanations such as resonances.

Minimizing the resonance content in a systematic way is thus a goal within PWA. For this, the Least Absolute Shrinkage and Selection Operator (LASSO) technique for model selection can be applied (which provides a Bayesian posterior-mode estimate), in combination with cross validation and/or information theory to control the size of the penalty parameter λ [212–214]. The combination of these techniques effectively suppresses the emergence of resonances except for those really needed by the data. The numerical implementation is especially simple because it affects only the calculation of the χ^2. Trial-and-error techniques, sometimes still applied to check for resonances in different partial waves, will become obsolete. Here, one simply starts with an over-complete resonance set plus flexible backgrounds, and the algorithm will remove all those resonances not needed by data, without manual intervention. Apart from cross validation, we will also consider information theory to regulate λ as proposed in Ref. [215]. In particular, the Akaike and Bayesian information criteria provide easy-to-use model selection. Results should be independent of the

choice of the criterion.

In 2017, the LASSO technique was, for the first time, used in pion photoproduction at low energies for the “blindfolded" selection of the relevant multipoles and their simplest parametrization to describe the available data [216]. The analysis of kaon-induced reactions is closely related. For a recent application in a different but related context see Ref. [217]. Once the model selection process is finished, uncertainties on resonance parameters can be obtained by the usual re-sampling techniques.

The existing and proposed PWA tools use different construction principles: resonances are included in the form of bare states, K-matrix poles, or generated from hadron dynamics itself. For the first two classes of approaches, one has at one's disposal the coupling constants that tune the interaction of a bare singularity with the meson-baryon continuum. Those are fit parameters that can be explicitly included in the penalty term. If resonances are generated from the meson-baryon dynamics itself, the case is a bit more complicated, because there are no directly accessible tuning parameters. This parametrization, practiced by the GW/SAID group for many years (see, e.g., Ref. [205]), is, in principle, the cleanest analysis tool, because resonance generation does not require manual intervention. Yet, even here the emergence of resonance terms can be penalized, e.g., through the value of contour integrals on the second Riemann sheet where resonance poles are located (a value of zero corresponds then to the absence of poles).

It should be stressed that the information theory criteria do *not* require a good fit in a frequentist's sense because they merely compare the relative quality of models. This is especially relevant when it comes to the analysis of many different data sets (such as kaon-induced reactions) in which, e.g., the systematic errors might be underestimated such that a $\chi^2/\mathrm{d.o.f.} \approx 1$ is difficult to achieve.

Systematic uncertainties can be treated as in the GW/SAID approach [90] in which the χ^2 is defined as

$$\chi^2 = \sum_i \left(\frac{N\Theta_i - \Theta_i^{\mathrm{exp}}}{\epsilon_i} \right)^2 + \left(\frac{N-1}{\epsilon_N} \right)^2 , \tag{34}$$

where Θ_i^{exp} is an experimental point in an angular distribution and Θ_i is the fit value. Here the overall systematic error, ϵ_N, is used to weight an additional χ^2 penalty term due to renormalizaton of the fit by the factor N. The statistical error is given by ϵ_i. Note that the fit function is penalized, rather than the data, to avoid the bias discussed in Ref. [218]. See also Ref. [219] for further discussion of this topic.

15.2 Goodness-of-Fit Tests

The χ^2 per degree of freedom, $\chi^2_{d.o.f.}$, is usually considered as a criterion for a good fit, but becomes meaningless if thousands of data points are fitted (and should be replaced by Pearson's χ^2 test). Statistical χ^2 tests will become possible through the new data, putting resonance analysis on a firmer ground. While χ^2 tests are sensitive to under-fitting, they are insensitive to over-fitting. Here, the F-test [220] is suitable to test the significance of new fit parameters. That test, can, thus, be applied to reduce the number of internal parameters in a partial-wave parametrization, which results in more reliable estimates of uncertainties for extracted resonance parameters such

as masses, widths, and branching ratios.

With increased consistency of data through the KLF experiment, other goodness-of-fit criteria can also be applied, such as Smirnov-Kolmogorov or Anderson-Darling tests for normality [221, 222] or run tests from non-parametric statistics. For pion photoproduction, these tests are applied and extensively discussed in Ref. [216].

A prerequisite to carry out classical statistical tests is data consistency. As discussed before, this is unfortunately not always the case in the $S = -1$ sector. The proposed KLF measurements will produce, for the first time, a body of data large enough to enable such tests reliably.

15.3 Representation of Results

As mentioned, ED parametrizations are needed to extract resonance parameters, but single-energy (SE) fits are useful to search for narrow structures, or for other groups to test theoretical models of hadron dynamics. The question arises how the partial waves can be presented to allow the theory community to carry out their fits. As recently demonstrated [223], SE solutions alone carry incomplete statistical information, mainly because they are correlated quantities. We plan to provide the analysis results in a similar form as recently done in Ref. [223] for elastic πN scattering. With this, the theory community can fit partial waves through so-called *correlated* χ^2 *fits* obtaining a χ^2 close to the one obtained in a fit directly to data (see Ref. [223] for an extended discussion). This format ensures that the maximal information from experiment is transmitted to theory, allowing to address the *missing resonance problem* in the wider context of questions related to confinement and mass generation, that have been paramount problems in hadronic physics for decades.

In summary: With a large consistent data set from the KLF experiment, an entire class of statistical tools will become applicable that is needed to conduct rigorous baryon spectroscopy. With the new data, the quantitative significance of resonance signals and the quantitative uncertainties of resonance parameters can be determined.

16 Appendix A4: Neutron and Gamma Background

1. **Elements of the Be-target Assembly**

   Schematic view of the Be-target assembly (K_L production target) is given on Fig. 19. Elements of the Be-target assembly are presented in Table 4. The weight of the construction is 14.5 ton. Changeover from the photon to K_L beamline and from the K_L beamline to photon is expected to take less or about 6 months (after the radiological cooldown). This break fits current the CEBAF Accelerator schedule well and the beam collimator cave has enough space (4.52 m width) for the Be-target assembly out of the beamline.

2. **Neutron and Gamma Background**

   The schematic view of the collimator cave with the Be-target assembly is given on Fig. 17.

Table 4: Elements of the Be-target assembly.

Element	Outer ∅/Inner ∅ (m)	Height (m)	Volume (m^3)	Density (kg/m^3)	Mass (kg)
Borated polyethylen (front)	1.20/0.16	0.10	0.111	1000	111.1
Borated polyethylen (side)	1.20/1.00	1.30	0.449	1000	449.2
Borated polyethylen (back)	1.20/0.08	0.10	0.113	1000	112.6
Lead (front)	1.00/0.16	0.30	0.230	11350	2605.8
Lead (side)	1.00/0.76	0.70	0.232	11350	2635.8
Lead (back)	1.00/0.08	0.30	0.234	11350	2657.2
Tungsten (front)	0.76/0.16	0.40	0.173	19300	3346.9
Tungsten (center)	0.76/0.00	0.10	0.045	19300	875.5
Tungsten (back)	0.76/0.08	0.20	0.090	19300	1731.7
Beryllium	0.06/0.00	0.40	0.001	1848	2.1

Several tallies were placed along the beam and at the experimental hall for neutron and gamma fluence estimation. Tally descriptions are:

- **#1**: spot for flux (∅0.07 m) on the beam in the experimental hall right behind of the concrete wall;
- **#2**: spot for flux (∅0.07 m) outside the beam in the experimental hall right behind of the concrete wall;
- **#3**: spot for flux (∅0.07 m) on the beam in the experimental hall right on the face of the cryogenic target;
- **#4**: spot for flux (∅0.07 m) outside the beam in the experimental hall right on the face of the cryogenic target;
- **#5**: area for dose rate (6×6 m^2) on ceiling of the experimental hall centered at the GlueX detector - key area for the RadCon;
- **#6**: ring for dose rate (outer ∅0.08 m and inner ∅0.07 m) on the face of the cryogenic target - to evaluate a radiation damage for the SiPMs;
- **#7-9**: area for dose rate (1×1 m^2) hallway in the experimental hall following the GlueX detector;
- **#10-19**: rings for dose rate (outer ∅0.25, 0.45, 0.65, 0.85, 1.05, 1.25, 1.45, 1.65, 1.85, 2.05 m and inner ∅0.20, 0.40, 0.60, 0.80, 1.00, 1.20, 1.40, 1.60, 1.80, 2.00 m, respectively) on the face of the cryogenic target - to evaluate a radiation damage for the front of the BCAL;
- **#20**: spot for flux (∅0.07 m) on the beam right behind beryllium;
- **#21**: spot for flux (∅0.07 m) on the beam right behind tungsten.

(a) **Neutron Background**

Calculations were performed for different shielding modifications in the collimator cave to minimaize the neutron and gamma dose rate.

K_Ls, produced by the Be-target and survived after the beam tungsten or lead plug, are presented on Fig. 55. This figure shows that there is a small effect in the material difference in the beam plug. There are 10% of K_Ls, produced by the Be-target, survived after the beam tungsten plug. The neutron yield integral from the berilium is $2.4 \times 10^{10}\ n/(s \cdot cm^2)$ and then from tunsten is $4.2 \times 10^9\ n/(s \cdot cm^2)$ (Figs. 56 and 57). So, the tungsten plug reduced the neutron flux by the same amount as the neutral kaon flux and main contribution to the neutron background associated with neutrons below 10 MeV.

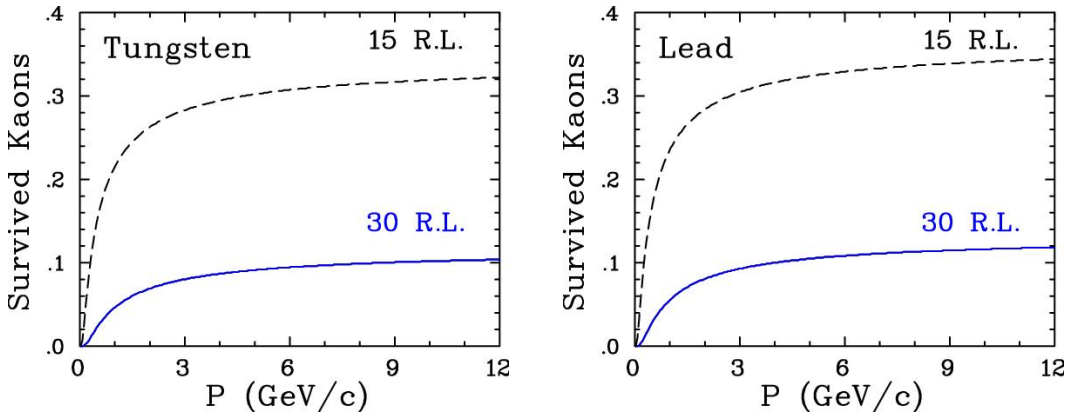

Figure 55: Survived neutral kaons (in arbitrary units) after the tungsten (left) or lead (right) plug with 15 or 30 R.L.s.

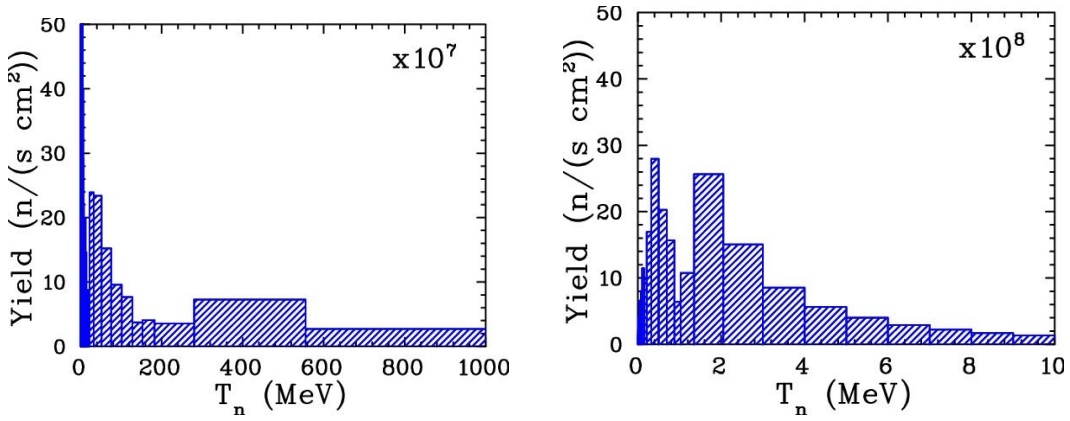

Figure 56: Survived neutrons after the berilium. Neutron calculations were performed using the MCNP Transport code [154].

Calculations were performed for different shielding modifications in the collimator cave to minimaize the neutron and gamma dose rate. The vertical (horizontal) cross section of the neutron flux is given on Fig. 58 (Fig. 59).

(b) **Gamma Background**

The vertical cross section of the gamma flux is given on Fig. 60.

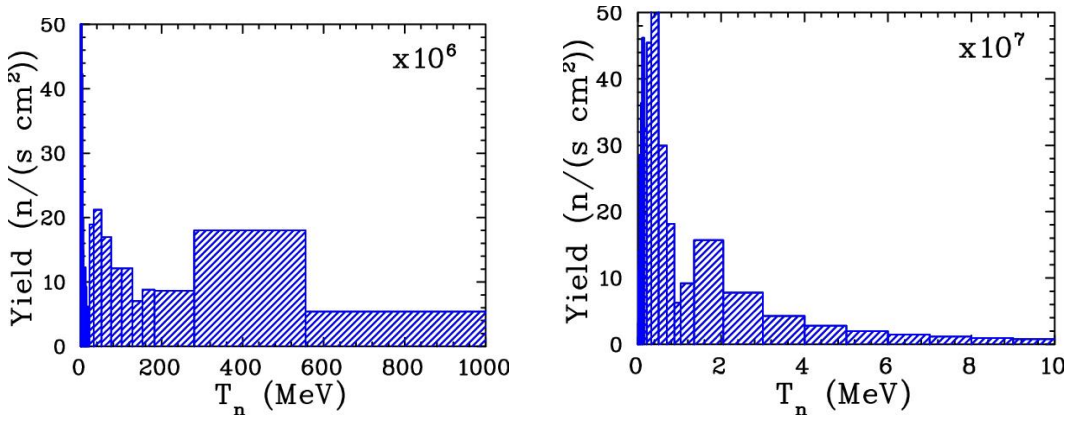

Figure 57: Survived neutrons after the tungsten. Neutron calculations were performed using the MCNP Transport code [154].

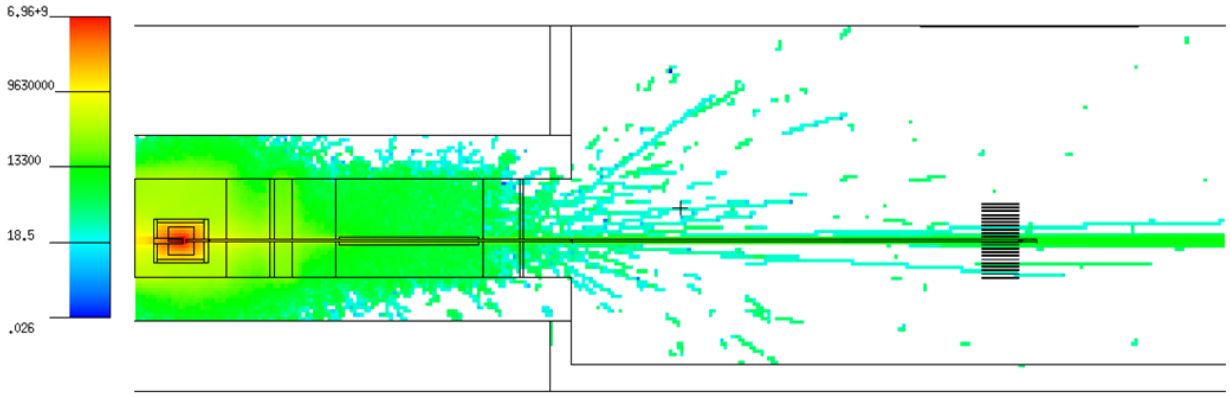

Figure 58: Vertical cross section of the neutron flux calculated for the model. Beam goes from left to right.

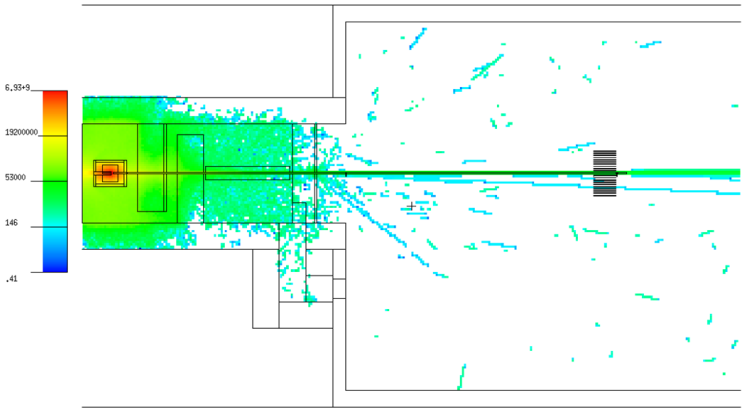

Figure 59: Horizontal cross section of the neutron flux calculated for the model. Beam goes from left to right.

Table 5: Neutron (2nd column) and gamma (3rd column) background flux calculated for different tallies (1st column).

Tally	Neutron flux (n/(s·cm^2))	Photon flux (γ/(s·cm^2))
#1	(8.0±0.6)×10^4 (8.0%)	(31.2±0.1)×10^6 (0.3%)
#2	(4.0±2.3)×10^2 (58%)	(4.7±3.3)×10^2 (71%)
#3	(1.6±0.2)×10^3 (13%)	(27.4±0.1)×10^6 (0.2%)
#4	(2.8±0.6)×10^3 (22%)	(10.3±0.5)×10^4 (4.7%)
#20	(236.0±0.2)×10^8(0.1%)	(223.0±0.1)×10^{10} (0.02%)
#21	(41.7±0.1)×10^8(0.1%)	(10.7±0.1)×10^8 (0.4%)

Table 6: Neutron (2nd column) and gamma (3rd column) dose rate background calculated for different tallies (1st column).

Tally	Dose rate (mrem/h)	Dose rate (mrem/h)
#5	0.2±0.1 (46%)	(2.1±0.1)×10^{-2} (3.6%)
#6	2.0±0.4×10^3 (18%)	(14.8±0.2)×10^3 (1.5%)
#7	> 0.1	(5.2±3.0)×10^{-3} (58%)
#8	> 0.1	(7.4±3.0)×10^{-3} (41%)
#9	> 0.1	(2.6±0.6)×10^{-2} (24%)
#10	82.8±28.5 (34%)	(12.5±1.6) (13%)
#11	4.3±2.7 (64%)	(0.72±0.08) (11%)
#12	2.1±1.3 (60%)	(0.60±0.07) (12%)
#13	1.7±1.5 (87%)	(0.60±0.09) (14%)
#14	0.2±0.1 (71%)	(0.45±0.04) (8.5%)
#15	0.1±0.1 (67%)	(0.32±0.02) (4.7%)
#16	0.5±0.3 (57%)	(0.35±0.04) (11%)
#17	0.8±0.4 (46%)	(0.29±0.02) (7.5%)
#18	0.6±0.3 (49%)	(0.26±0.02) (6.9%)
#19	0.4±0.2 (56%)	(0.21±0.01) (6.3%)

17 Appendix A5: Details of Monte Carlo Study

17.1 Particle Identification

For each topology, one primary particle (the proton for the $K_S p$ channel, the π^+ for the $\pi^+\Lambda$ channel and the K^+ for the $K^+\Xi$ and K^+n channels) provides a rough determination for the position of the primary vertex along the beamline that is used in conjunction with the ST to determine the flight time and path of the K_L from the beryllium target to the hydrogen target. Protons, pions, and kaons are distinguished using a combination of dE/dx in the chambers and time-of-flight to the outer detectors (BCAL and TOF). The energy loss and timing distributions for the $K_S p$ channel are shown in Fig. 61; the distributions are similar for the $\pi^+\Lambda$ channel, where a proton band arises from the $\Lambda \to \pi^- p$ decay. Also shown is the dE/dx distribution for the $K^+\Xi^0$ channel, where a prominent kaon band can be seen, along with pion and proton bands arising from Λ decays.

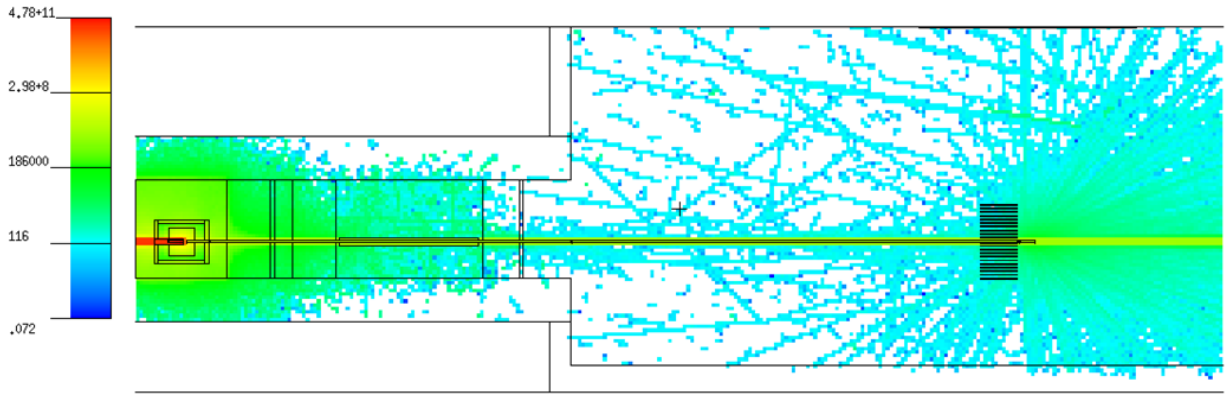

Figure 60: Vertical cross section of the gamma flux calculated for the model.

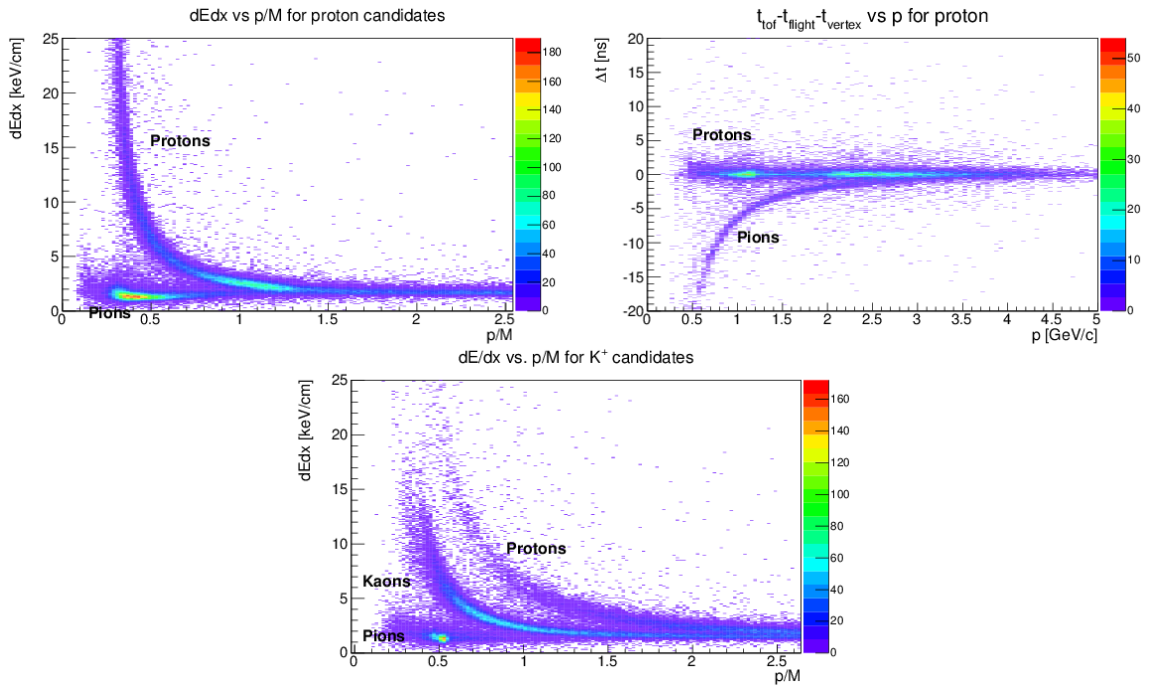

Figure 61: Particle identification. Top left panel: dE/dx for the K_Sp channel. Top right panel: time difference at the primary "vertex" for the proton hypothesis for the K_Sp channel using the TOF. Bottom panel: dE/dx for the $K^+\Xi$ channel. The proton and pion bands arise from the decay of the Λ.

Since the GlueX detector has full acceptance in ϕ for charged particles and large acceptance in θ (roughly $1 - 140°$), a full reconstruction of events is feasible for the majority of the channels. That will allow to apply four or more overconstrain kinematical fit and improve the resolution considerably. A typical comparison between W reconstruction using the K_L-momentum for 250 ps ST resolution (red dots) and the other using kinematically fitted final-state particles for the K_Sp channel (blue dots) is shown in Fig. 62.

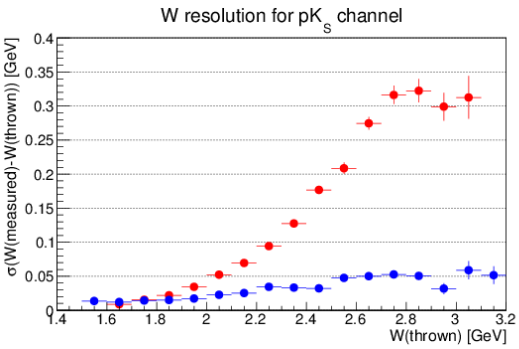

Figure 62: W resolution for the K_Sp channel, (blue dots) using kinematic fitting after reconstruction of all final state particles; (red dots) using K_L time-of-flight.

17.1.1 Details of MC study for $K_Lp \to K_Sp$

For the K_Sp channel, we take advantage of the BR of 69.2% for $K_S \to \pi^+\pi^-$ [2]: the invariant mass of the $\pi^+\pi^-$ pair and W as computed from the four-momenta of the proton and the two pions is shown in Fig. 63.

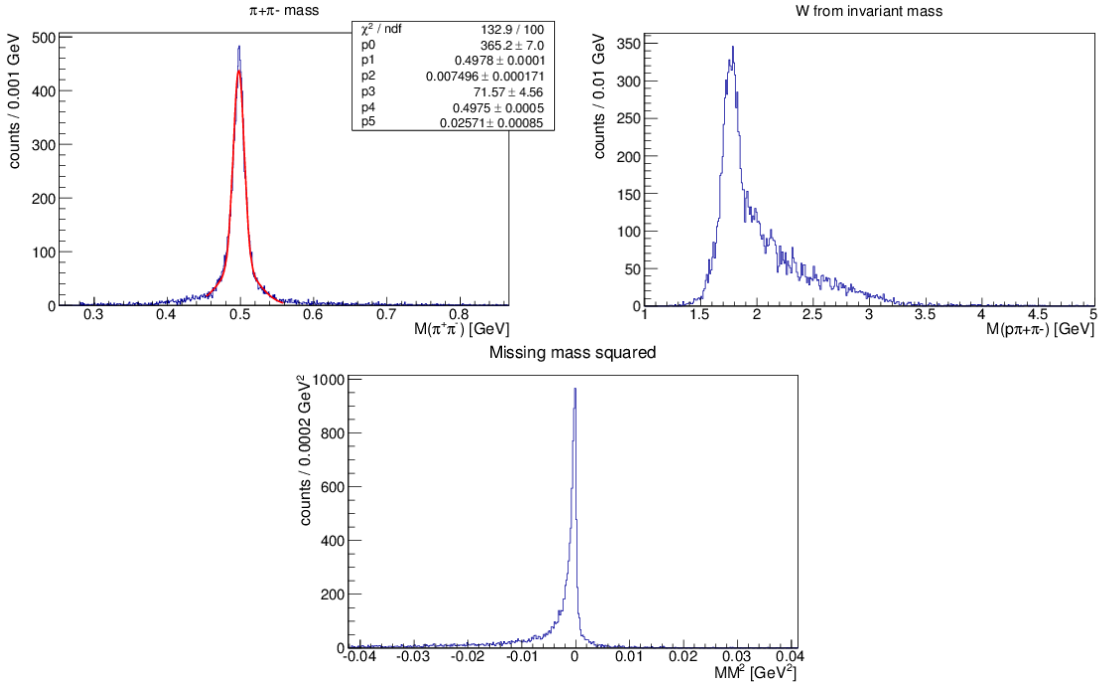

Figure 63: Full reconstruction for $K_Lp \to K_Sp$ and $K_S \to \pi^+\pi^-$. Top left panel: $\pi^+\pi^-$ invariant mass. Top right panel: W computed from $\pi^+\pi^-p$ invariant mass. Bottom panel: Missing-mass squared for the full reaction.

After combining the four-momenta of the final-state particles with the four-momenta of the beam and the target, the missing-mass squared for the full reaction should be zero, which is also shown in Fig. 63. Finally, one requires conservation of energy and momentum in the reaction by applying

a kinematic fit to the data. After applying a 0.1 cut on the confidence level of the fit, one computed an estimate for the reconstruction efficiency as a function of W as shown in Fig. 64. Here the efficiency includes the BR for $K_S \to \pi^+\pi^-$. The average reconstruction efficiency is about 7%.

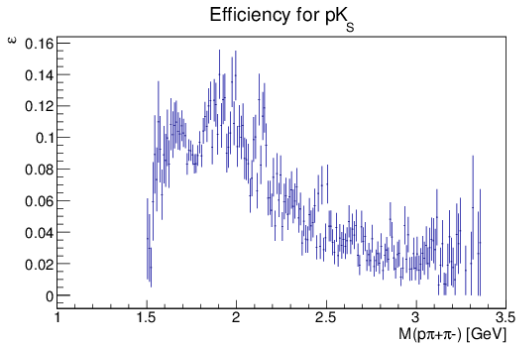

Figure 64: Estimate for efficiency for full reconstruction of the $K_L p \to K_S p$ and $K_S \to \pi^+\pi^-$ reaction chain as a function of W.

17.1.2 Details of MC study for $K_L p \to \pi^+\Lambda$

For our proposed KL Facility at Hall-D, we expect good statistics of $K_L p \to \pi^+\Lambda$ for a very wide range of K_L beam momentum. Figure 65 shows the K_L beam momentum distributions from the generated (left) and reconstructed (right) with requiring $\beta_{K_L} > 0.95$ in time-of-flight.

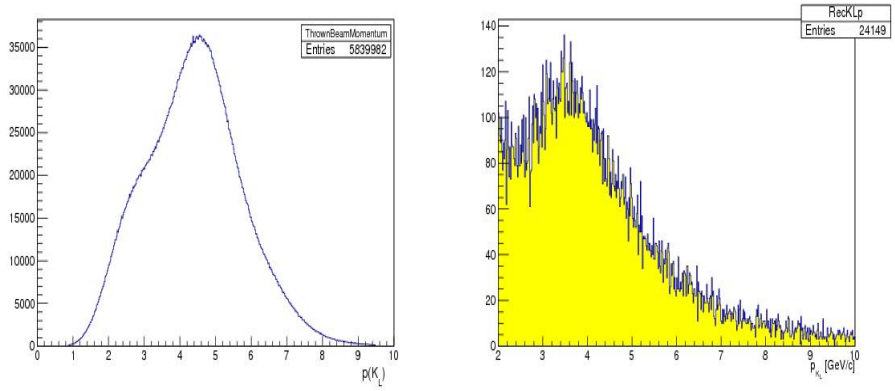

Figure 65: Beam particle (K_L) momentum distribution in MC simulation, Left panel: Generated. Right panel: Reconstructed.

We have generated the $K_L p \to \pi^+\Lambda$ reaction in phase space taking into account the realistic K_L beam momentum distribution in the event generator. This momentum spectrum is a function of the distance and angle. Then we went through the standard Hall-D full GEANT simulation with GlueX detector and momentum smearing. Finally, we utilized the JANA for particle reconstruction

that we simulated. Figure 66 shows a sample plot for polar angle versus momentum distribution of π^+, π^-, and protons from the generated event (left) and reconstructed event (right).

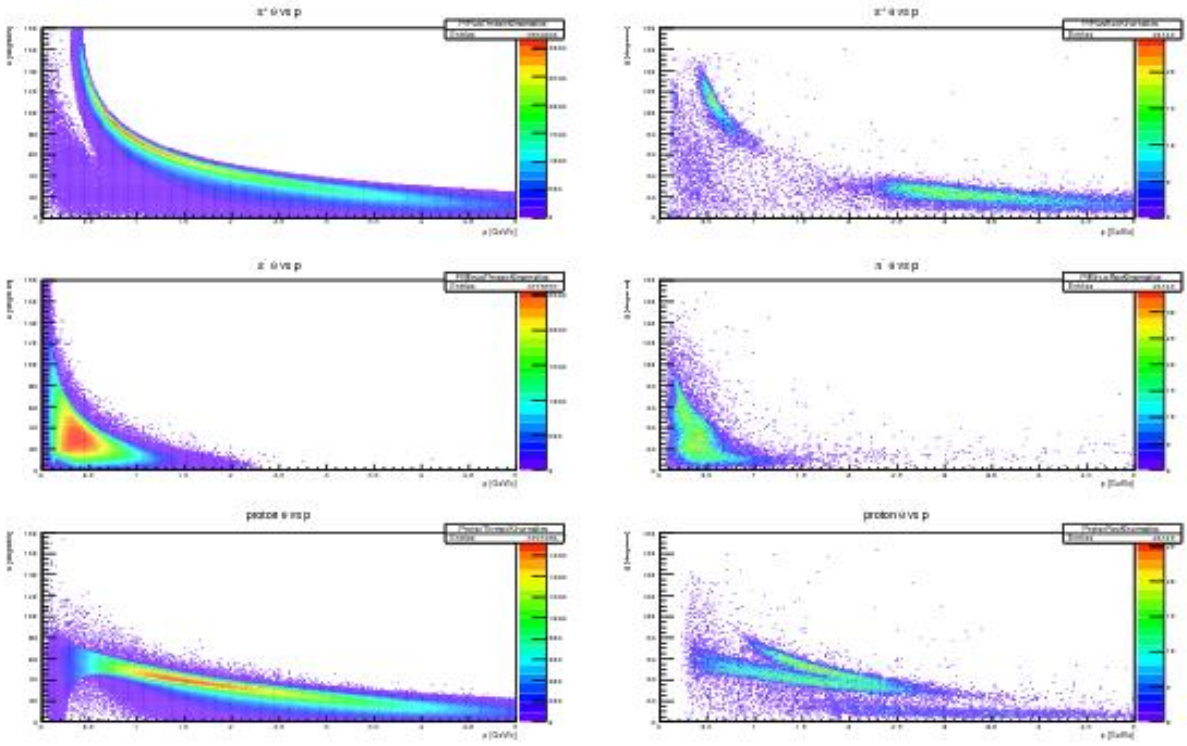

Figure 66: Momentum and angular distributions. Top row panel: π^+, Middle row panel: π^-, Bottom row panel: proton. Left column panels: Generated and Right column panels: Reconstructed events.

Figure 67 shows an example of the reconstructed the Λ particle for invariant mass (left) and missing mass (right). We obtained a 5 MeV invariant-mass resolution and a 150 MeV missing-mass resolution. We estimate the expected total number of $\pi^+\Lambda$ events as final-state particle within topology of $1\pi^+$, $1\pi^-$, and 1 proton. In 100 days of beam time with $1 \times 10^4 K_L/s$ on the liquid hydrogen target, we expect to detect around 5.3 M $K_L p \to \pi^+\Lambda$ events for $W < 3$ GeV. Such an unprecedented statistics will improve our knowledge of these states through PWA.

Moreover, Fig. 68 (left) shows the correlation between Λ invariant mass from its decay particles (p, π^-) and missing mass of π^+X. The right plot in Fig. 68 shows the Λ invariant mass as a function of pion angular distribution (θ_{π^+}). All these plots are based on the 250 ps time resolution of the ST.

The $K_L p \to \pi^+\Lambda$ reaction has a relatively high production cross section the order of a few mb in our proposed K_L-momentum range (1 – 6 GeV/c). The beam resolution has been calculated at the time-of-flight vertex time resolution (250 ps) of the start counter (TOF-ST).

The major source of systematic uncertainty for this reaction would be mistaken particle identification among π^+, K^+, and proton in the final state. However, requiring the reconstructed Λ and

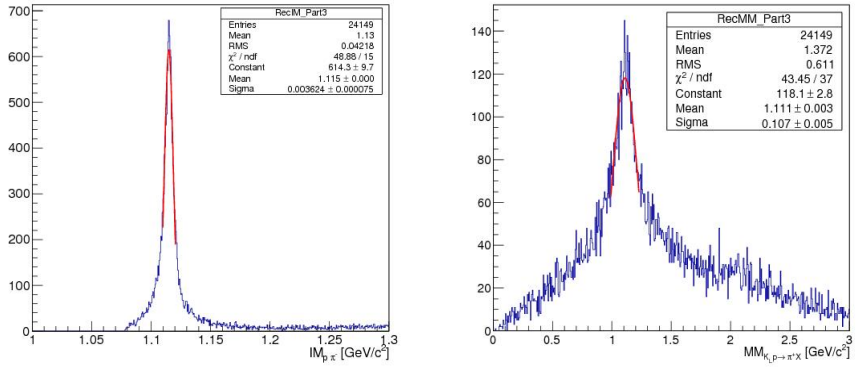

Figure 67: The Λ invariant-mass distribution reconstructed. Left panel: From its $\pi^- p$ decay particles. Right panel: The missing mass of $\pi^+ X$ (right).

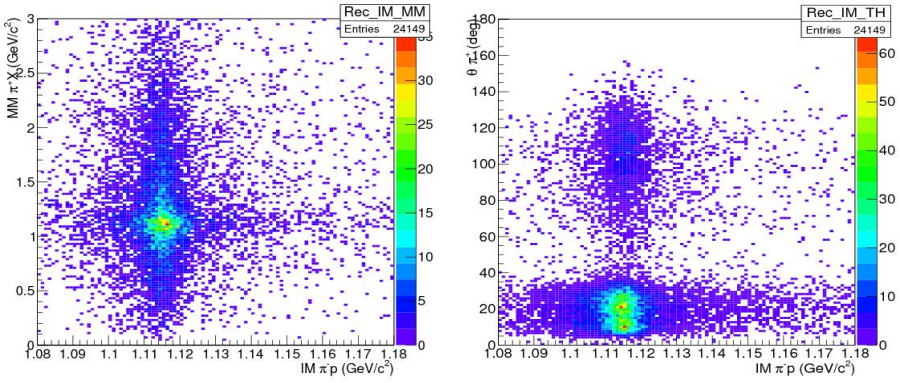

Figure 68: Left panel: The Λ invariant mass versus missing mass of $\pi^+ X$. Right panel: The θ_{π^+} angle distribution versus Λ invariant mass (right).

side-band subtraction technique for background will improve this uncertainty substantially.

17.1.3 Details of MC study for $K_L p \to K^+ \Xi^0$

The section here focuses on the reconstruction of $K_L p \to K^+ \Xi^0$ but the initial procedure for particle identification and reaction reconstruction is almost identical to the reaction on the neutron ($K_L n \to K^+ \Xi^-$). Three topologies can be used to reconstruct the reaction $K_L p \to K^+ \Xi^0$ on free proton targets. Topology 1 requires the detection of a K^+, topology 2 requires the detection of a K^+ and a Λ by utilizing its high branching ratio to a $\pi^- p$ pair (63.9%), and Topology 3 requires the detection of the two-photon decay of the π^0 from $\Xi \to \pi^0 \Lambda$. In the case of $K_L n \to K^+ \Xi^-$, features from having a target nucleon with a non-zero momentum are removed from the analysis by detecting all final state particles (one K^+, one proton, and two π^-). Particle identification is done

via a probabilistic approach involving dE/dX, time-of-flight, and track curvature information as described in Appendix A5 (Sec. 17.1). The dE/dX distributions for kaon, proton, and π^- candidates are shown in Fig. 69.

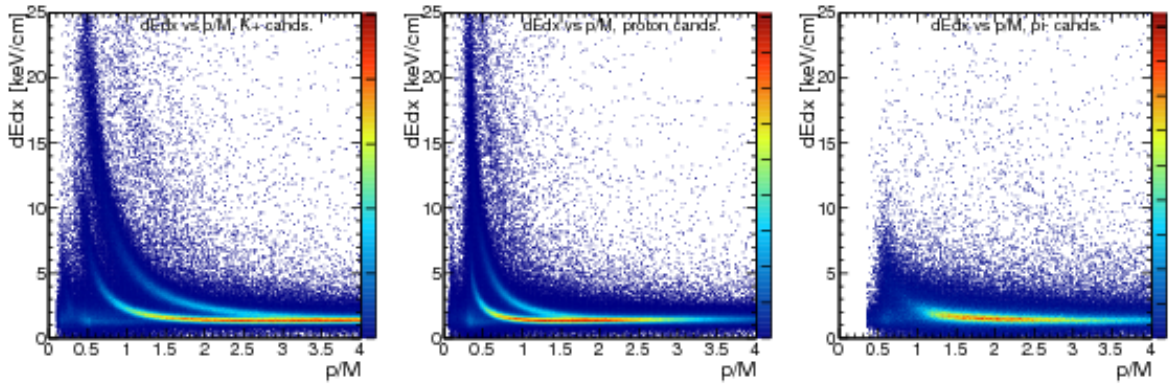

Figure 69: dE/dX distributions used in kaon proton and π^- identification for the reconstruction of $K_L p \to K^+\Xi^0$.

At low particle momenta, kaons and protons can be well separated, but high-energy particles cannot be unambiguously differentiated by dE/dX or by ToF information, which leads to particle misidentification. The higher the W, the higher ejectile energy and the more misidentification contributions we have. In this analysis (specifically Topology 2 and 3), these events were largely removed by making an invariant-mass cut on the $\pi^- p$ pair.

Figure 70 shows the missing mass of $K_L p \to K^+ X$ for simulated data for the reaction $K_L p \to K^+\Xi^0$ used in the reconstruction of all topologies, the invariant-mass distribution of the $\pi^- p$ pair used to reconstruct Topology 2 ($K_L p \to K^+\Lambda X$) and 3, and the invariant-mass of the two-photon pair used to reconstruct Topology 3 ($K_L p \to K^+\Lambda\pi^0$). A 3σ cut on these distributions allows us to reconstruct the reaction fully. The left panel of Fig. 70 shows the 3σ W-dependent cut applied to select the missing Ξ^0 as well as the W-dependent 3σ cut to reconstruct the reaction $K_L p \to K^+ n$. (See Appendix A5 (Sec. 17.1.4) for more details on the sources of resolution effects on the missing mass.) The latter is one of the major sources of background for our reaction for Topology 1; however, the missing-mass resolution (obtained with a vertex-time resolution of 250 ps) allows a clean separation of these two reactions up to $W = 2.3$ GeV Above this value, special treatment of the $K_L p \to K^+ n$ background is required as discussed in greater detail in Appendix A5 (Sec. 17.1.3).

Similarly, the reconstruction of $K_L n \to K^+\Xi^-$ is done by first identifying the pion that originates from the Λ decay. The left panel of Fig. 71 shows the invariant mass of the proton and the one of the two detected pions. It is clear from this that the pion that originates from the Λ is easily identified with minimal combinatorial background.

The invariant mass of the two pions and proton is shown on the right panel of Fig. 71.

The detection efficiency as a function of the true W for each topology for the reaction on the proton is shown in Fig. 72. As expected, the efficiency is highest for Topology 1 reaching a maximum

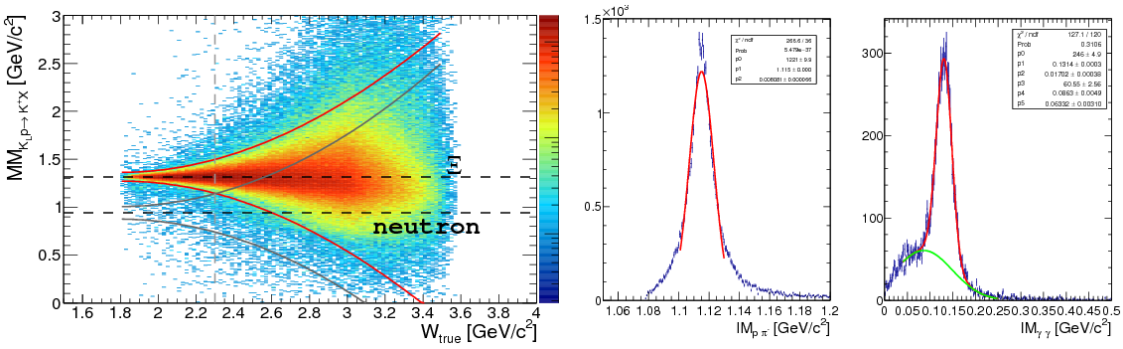

Figure 70: The missing mass of the reaction $K_Lp \to K^+X$ used to reconstruct the reaction $K_Lp \to K^+\Xi^0$ (Topology 1), and the invariant mass of $p\pi^-$ pair (Topology 2), and the invariant mass of the two-photon pair (Topology 3).

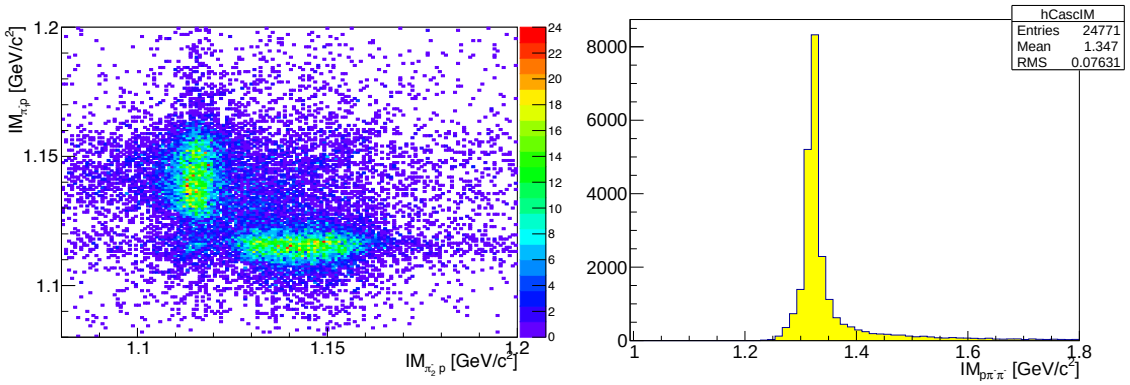

Figure 71: Left: Invariant mass of detected proton and pi_1^- as a function of Invariant mass of detected proton and pi_2^-. Right: Invariant mass of detected proton and two pi^-.

at 60% for $W = 2.05$ GeV. The efficiency for Topology 2 is about an order of magnitude less than Topology 1, and Topology 3 detection efficiency is on average 0.8%. The efficiency for the reaction on the neutron for a fully exclusive reaction is of the order of a few percent.

$K_Lp \to K^+\Xi^0$ background suppression: Different sources of background will contribute in the three topologies used to study this reaction. Disentangling our signal $K_Lp \to K^+\Xi^0$ from the reaction $K_Lp \to K^+n$ (for Topology 1), which has two orders of magnitude larger cross section is expected to be relatively straightforward. As mentioned before, a simple missing-mass cut is sufficient to remove any contributions from this reaction for $W < 2.3$ GeV. For $W > 2.3$ GeV, an s-weight approach (or neuralNets, etc.) can be utilized to remove these contribution as the shape of the background under any cascade events can be well established from simulations. Figure 73 shows the W-dependence of the missing-mass distribution of $K_Lp \to K^+X$ for the simulated reactions $K_Lp \to K^+\Xi^0$ and $K_Lp \to K^+n$ (left panel). The right panel shows the missing-mass projection at $W = 1.9$ GeV. In addition to $K_Lp \to K^+n$, the reaction $K_Lp \to \pi^+\Lambda$ is also a source of background events for Topology 1 ($K_Lp \to K^+X$) and 2 ($K_Lp \to K^+\Lambda X$). This

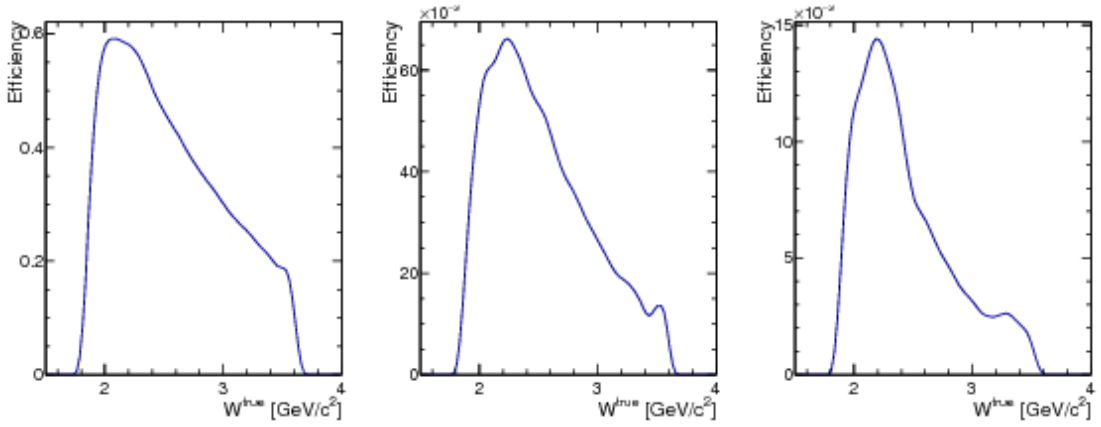

Figure 72: The detection efficiency for the reaction $K_L p \to K^+ \Xi^0$ for each topology.

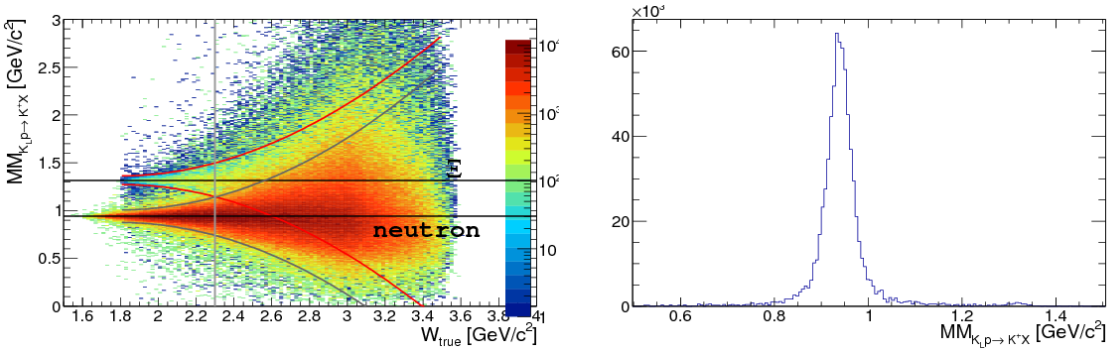

Figure 73: The missing mass of the reaction $K_L p \to K^+ X$ used to reconstruct the reactions $K_L p \to K^+ \Xi^0$ (Topology 1) and $K_L p \to K^+ n$ (which has about 2 orders of magnitude larger cross section). Right panel shows the missing mass at $W = 1.9$ GeV.

channel contributes when the final-state π^+ is misidentified as a K^+. This shifts the missing mass of $K_L p \to \pi^+ X$ to values lower than the ones expected, which leads to a good separation of this source of background below $W < 2.2$ GeV. Figure 74 shows the missing-mass distribution of these misidentified events. Contributions from these events for Topology 3 is completely removed by the requirement of two photons in the final state that reconstruct the mass of π^0. For Topology 2, coplanarity cuts between the reconstructed (misidentified) K^+ and Λ can reduce contributions, where as a background subtraction approach using the missing-mass information can be used to remove any contribution at $W > 2.2$ GeV.

Ξ^0 induced polarization: In terms of four-vectors, conservation of energy and momentum for this reaction is written as follows:

$$\mathcal{P}_{K_L} + \mathcal{P}_p = \mathcal{P}_{K^+} + \mathcal{P}_{\Xi^0}. \tag{35}$$

The production plane is then defined by

$$\hat{y} = \frac{\vec{P}_\Xi \times \vec{P}_{K_L}}{|\vec{P}_\Xi \times \vec{P}_{K_L}|}. \tag{36}$$

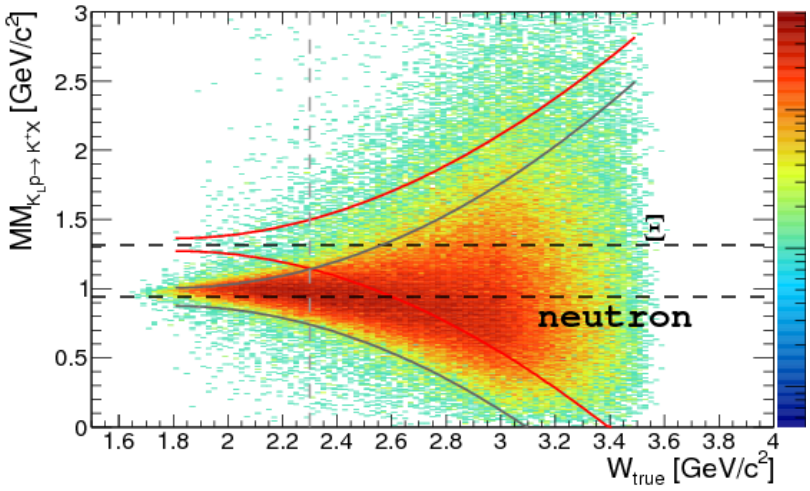

Figure 74: The missing mass of the reaction $K_Lp \to K^+X$ for simulated events from the reaction $K_Lp \to \pi^+\Lambda$. The reconstructed events here results from a pion misidentified as a kaon.

The $\hat{z}$ axis lies along the beam direction

$$\hat{z} = \frac{\vec{P}_{K_L}}{|\vec{P}_{K_L}|}, \tag{37}$$

and thus the $\hat{x}$ axis is defined to give a right-handed coordinate system:

$$\hat{x} = \hat{y} \times \hat{z}. \tag{38}$$

The determination of P_Ξ^y can be established by linear fits to the acceptance-corrected pion angular ($\cos\theta_\pi^y$) yields. Fitting these distributions with a first-degree polynomial,

$$y = a_0(1 + a_1 \cos\theta_\pi^y), \tag{39}$$

allows the determination of a_1, which gives us the the induced polarization

$$a_1 = P_\Xi^y \alpha. \tag{40}$$

Alternatively, one can determine the induced polarization transfer from determining the forward-backward asymmetry, A^y, of the pion angular distribution. This asymmetry is defined as

$$A^y = \frac{N_+^y - N_-^y}{N_+^y + N_-^y}, \tag{41}$$

where N_+^y and N_-^y are the acceptance-corrected yields with $\cos\theta_\pi^y$ positive and negative, respectively. The asymmetry is related to the induced polarization by

$$P_\Xi^y = \frac{-2A^y}{\alpha}. \tag{42}$$

The statistical uncertainty in the asymmetry measurement of P_{Ξ}^{y} is related to the Poisson uncertainty in N_{+}^{y} and N_{-}^{y}. Propagating this uncertainty to the uncertainty of A^{y} gives

$$\sigma_{A^y} = \frac{2}{(N_{+}^{y} + N_{-}^{y})^2} \sqrt{N_{+}^{y} N_{-}^{y} (N_{+}^{y} + N_{-}^{y})}. \tag{43}$$

The uncertainty in P_{Ξ}^{y} is then found by propagating σ_{A^y} and σ_{α}:

$$\frac{\sigma_{P_{\Xi}^{y}}}{P_{\Xi}^{y}} = \sqrt{(\frac{\sigma_{A^y}}{A^y})^2 + (\frac{\sigma_{\alpha}}{\alpha})^2}. \tag{44}$$

17.1.4 Details of MC study for $K_L p \to K^+ n$

As described in Section 11.1.5 we used only K^+ detection to reconstruct this reaction. Kaon identification is done with a probabilistic approach involving dE/dX, time-of-flight, and track curvature information; see Appendix A5 (Sec. 17.1) for further details. Even in pure $K_L p \to K^+ n$ MC case one can have more than one charged particle track reconstructed due to various reactions in the detector volume. That is why in addition to the pronounced K^+ banana in Fig. 75 (left) we see some traces of pion and proton bands. At low K^+-momenta, kaons can be well separated from pions and protons, but high-energy particles cannot be differentiated by dE/dX or by ToF information leading to particle misidentification. The higher W (the higher the ejectile energy), we have and the more kaons we lose due to misidentification; see Fig. 75 (right, green). In our analysis, we restricted ourselves to one and only one reconstructed charged-particle track. This condition helps to suppress the background, but does not reduce the reconstruction efficiency; see Fig. 75 (right, black).

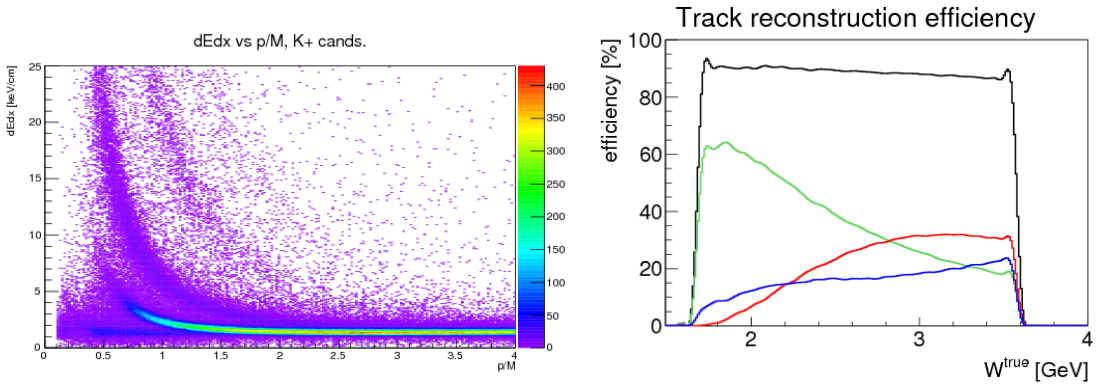

Figure 75: Left panel: dE/dx for the $K_L p \to K^+ n$ channel Right panel: single charged-particle track detection efficiency as a function of W for the $K_L p \to K^+ n$ channel. Any charged particle (black), kaon (green), proton (red), and pion (blue).

Charged-particle track detection efficiency stays flat over the full range of W, but kaon reconstruction efficiency drops from about 60% at low W to 20% at highest available energy. Since the GlueX acceptance is large and essentially hole-less, kaon reconstruction efficiency does not

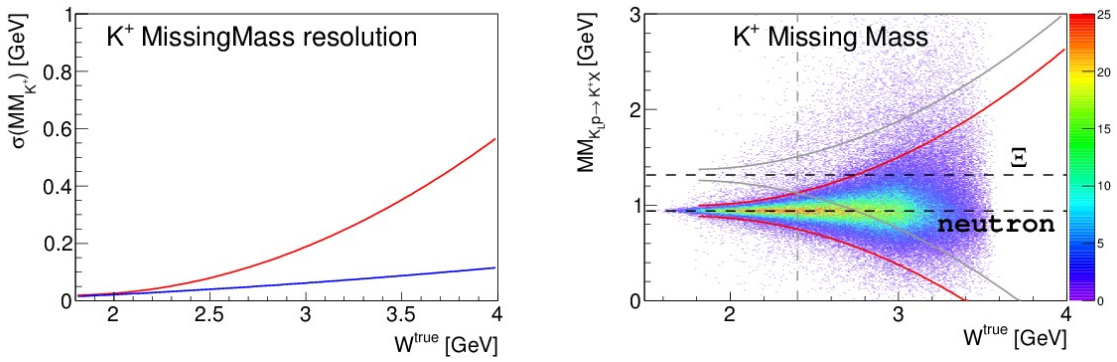

Figure 76: Left panel: Full (red) and detector related (blue) K^+ missing-mass resolution in terms of σ. In second case, the true K_L-momentum was used to calculate the missing mass. Right panel: K^+ missing-mass resolution as a function of W. 3σ missing-mass cuts for the $K_Lp \to K^+n$ (red) and $K_Lp \to K^+\Xi$ (gray) reactions are indicated by solid lines. Horizontal dashed lines show nominal masses of the neutron and Ξ baryon. The vertical gray dashed line indicates the range of pure missing-mass separation between these two reactions.

depend on yet unknown angular distributions. For the final selection of the $K_Lp \to K^+n$ reaction, we used a 3σ missing-mass cut around the neutron's mass; see Fig. 76.

Figure 76 was plotted under the assumption of a 250 ps vertex time resolution. Both W (Fig. 45) and missing-mass resolutions are driven by the K_L-momentum resolution.

Below $W = 2.4$ GeV, the $K_Lp \to K^+n$ and $K_Lp \to K^+\Xi$ reactions can be disentangled by K^+ missing mass alone. Above this value, special treatment of the $K_Lp \to K^+\Xi$ background is required. One may notice that a 3σ cut for the $K_Lp \to K^+n$ reaction rises faster than for $K_Lp \to K^+\Xi^0$. This effect has a purely kinematical explanation - due to the higher mass of the Ξ^0 baryon, the K^+ produced in $K_Lp \to K^+\Xi$ reaction has a lower energy for the same value of W. The lower the K^+ energy we have, the better missing-mass resolution we get, and the more narrow the missing-mass cut one needs to apply.

$K_Lp \to K^+n$ **background suppression:** Due to its very high cross section, the $K_Lp \to K^+n$ reaction is essentially background free. Due to the extremely high statistics expected for this reaction our uncertainties will be dominated by systematics. We have identified three major sources of physical background: $np \to K^+nn$, $np \to \pi^+nn$, and $K_Lp \to K^+\Xi$ reactions.

Details on $K_Lp \to K^+n$ and $K_Lp \to K^+\Xi$ separation can be found in Appendix A5 (Section 17.1.3). For $W < 2.3$ GeV, these two reactions can be separated by a 3σ K^+ missing-mass cut. Above $W = 2.4$ GeV, one can use standard background suppression techniques - S-weights, Q-weights, NeuralNets, etc. .... The main decay branch of Ξ is $\Xi^0 \to \pi^0\Lambda \to \pi^0\pi^-p$, which leads to several charged particles in the final state besides K^+; hence filtered out by a "one-charge-track-only" selection criterion. Another decay branch $\Xi^0 \to \pi^0\Lambda \to \pi^0\pi^0n$ cannot be filtered out that easily; however, due to its smaller branching ratio combined with the small $K_Lp \to K^+\Xi$ production cross section, this channel only contributes at the level of 10^{-3} even without any

background suppression techniques. Further suppression vetoing multiple neutral tracks and/or Q-weight should push this background far below 10^{-4}.

Neutron flux drops exponentially with energy (see Appendix A4 16 for details) and generally the high-energy neutron flux is small, but nonvanishing. If neutrons and K_Ls have the same velocity, they cannot be separated by time of flight. Neutron-induced reactions have high cross sections, which is why one needs to consider them as a possible source of background. In Fig. 77, one can see a comparison of kaon and neutron fluxes for the worse-case scenario when no neutron suppression is employed, similar to Fig. 24 (right) in terms of β. Particles with the same β cannot be separated by time of flight. At $\beta = 0.95$ neutron and kaon fluxes become equal. This speed corresponds to a neutron momentum of $p_n = 2.9$ GeV/c and kaon momentum of $p_K = 1.5$ GeV/c.

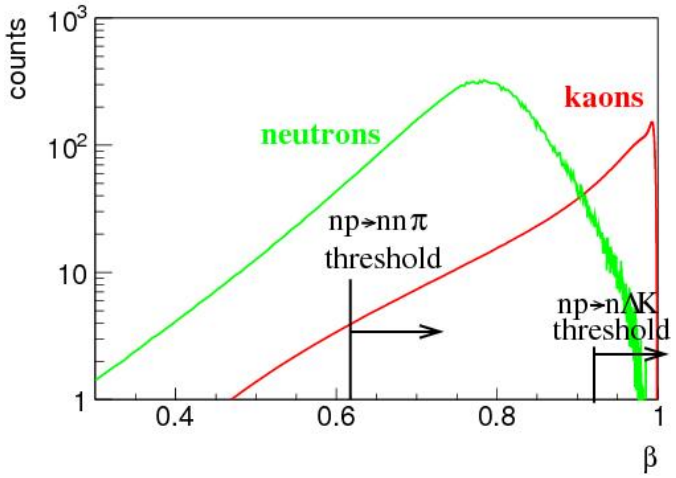

Figure 77: Neutron and K_L fluxes as a function of speed β.

To evaluate the amount of background, we need to fold this flux with production cross section and reconstruction efficiency. Let's first consider the $np \to K^+\Lambda n$ background. Unfortunately, this reaction is not very well measured, so we would use the $pp \to K^+\Lambda p$ cross-section parametrization together with the knowledge of $\frac{\sigma(pp\to K^+\Lambda p)}{\sigma(np\to K^+\Lambda n)} = 2$ from Ref. [225]. In Fig. 78, one can see the flux of K^+s from kaon-induced $K_L p \to K^+ n$ reaction in comparison to a neutron-induced $np \to K^+\Lambda n$ as a function of projectile speeds.

As one can see in Fig. 78, neutron-induced K^+ production contributes only in a very narrow range of energies. The contribution is also very small. One can further suppress this type of background by vetoing charged particles from Λ decay and performing a K^+ missing-mass cut. Altogether one can suppress this type of background below 10^{-4}.

The most dangerous type of neutron-induced background originates from the $np \to \pi^+ nn$ reaction with fast π^+ misidentification as K^+. There are no measurements of $np \to \pi^+ nn$ reaction but due to isospin symmetry one can relate this reaction to an isospin symmetric case $np \to \pi^- pp$. The later reaction is known, see Ref. [226]. The total cross section for this reaction is about 2 mb. The $np \to \pi^+ nn$ reaction has a much lower threshold compared to $np \to K^+\Lambda n$, so it can utilize

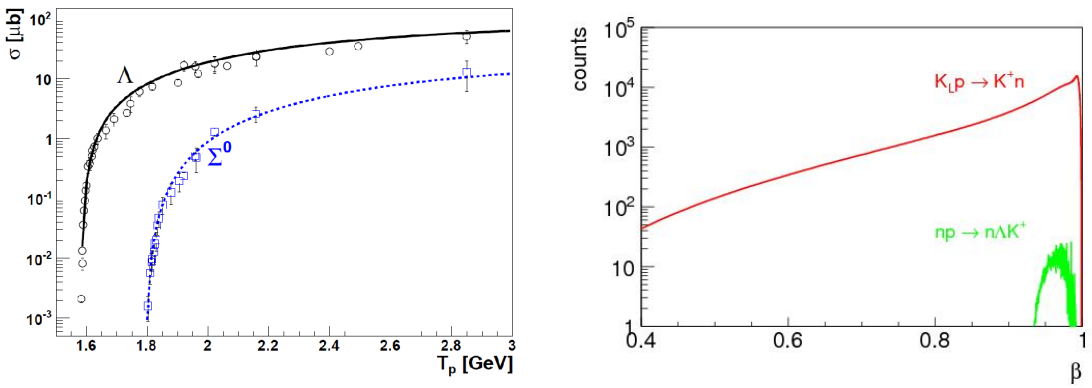

Figure 78: Left panel: $pp \to K^+\Lambda p$ total cross section from Ref. [225]. Right panel: K^+ flux as a function of projectile speed β for neutron-induced (green) and kaon-induced (red) reactions.

an enormous flux of low-energy neutrons. However, low-energy neutrons predominately produce low-energy pions, which can be separated from kaons. The background needs to be considered only for $\beta > 0.8$; see Fig. 79. The background level looks much higher compared to Fig. 78, but it can be severely suppressed with the "K^+" missing-mass cut since pion kinematics of the three-body $np \to \pi^+nn$ reaction are very different from $K_Lp \to K^+n$.

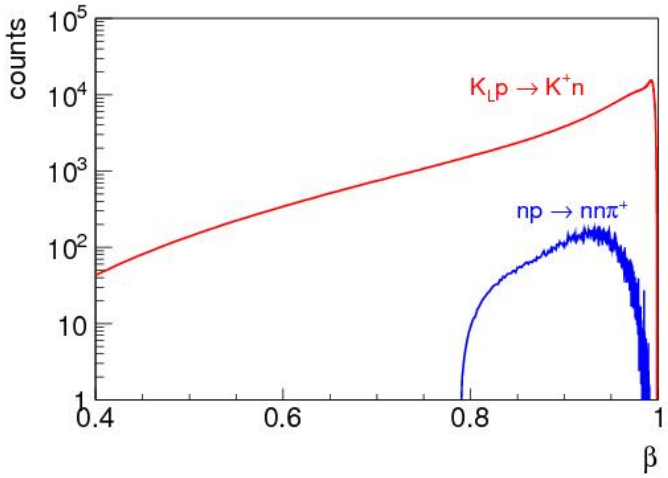

Figure 79: K^+ flux as a function of projectile speed for the $np \to \pi^+nn$ (green) and $K_Lp \to K^+n$ (red) reactions. Pion misidentification efficiency for the neutron-induced reaction is extracted from the full MC Geant simulation.

In summary: Kaon particle identification together with a simple 3σ missing-mass cut and assumption of K_L beam can efficiently suppress all physical backgrounds of the $K_Lp \to K^+n$ reaction.

18 Appendix A6: Current Hadronic Projects

Past measurements involving kaon scattering measurements were made at a variety of laboratories, mainly in the 1960s and 1980s when experimental techniques were far inferior to the standards of today (short summary is given in Sec. 6). It is important to recognize that current projects are largely complementary to the proposed Jlab KL hadron beam facility. We summarize the status of the FNAL, J-PARC, Belle, BaBar, $\overline{P}$ANDA, and COMPASS efforts here.

18.1 Hyperon Projects

18.1.1 Project X, USA

The status of Project X at FNAL [227–230] is as follows: First stage of Project X aims for neutrinos. Proposed K_L beam can be used to study rare decays and CP-violation [231]. It may be impossible to use the FNAL K_L beam for hyperon spectroscopy because of momentum range and n/K_L ratio (columns 4 and 6 at Table 7). In particular, the 8-yr old FNAL LoI addressed to the CP-violation study proposed to have a neutral kaon beam rate of 10^{10}/hr for high energies and very broad energy binning [232].

Table 7: Comparison of the K_L production yield. The BNL AGS kaon and neutron yields are taken from RSVP reviews in 2004 and 2005. The Project X yields are for a thick target, fully simulated with LAQGSM/MARS15 into the KOPIO beam solid angle and momentum acceptance from Ref. [228].

Project	Beam energy (GeV)	Target (λ_I)	p(K_L) (MeV/c)	K_L/s (into 0.5 msr)	n/K_L (E_n >10 MeV)
BNL AGS	24	1.1 Pt	300–1200	60×10^6	$\sim 1:1000$
Project X	3	1.0 C	300–1200	450×10^6	$\sim 1:2700$

18.1.2 J-PARC, Japan

While J-PARC has a whole program of charged strange particle and hypernuclear reactions, the photon beam at GlueX KLF allows unique access to other channels. J-PARC provides separated secondary beam lines up to 2 GeV/c (Table 8). The operation of the Hadron Experimental Facility resumed in April of 2015 following a two-year suspension to renovate the facility after the accident that occurred in May 2013 [233]. The primary beam intensity is currently 50 kW, and can be upgraded to 85 kW. This will correspond to $\sim 10^9$ ppp (particles per pulse) for pion beam intensity and to $\sim 10^6$ ppp for negative kaon beam flux. The K/π ratio is expected to be close to 10, which is realized with double-stage electrostatic separators. One of the main problems in the K/π separation is a high duty-factor of the J-PARC Complex.

Table 8: J-PARC beamlines in the Hadron Experimental Facility from Ref. [234]. Top part of Table gives information about beamlines in the present hall, while bottom part information is about new beamlines in the extended area.

Beamline	Particle	Momentum (GeV/c)	Number of particles per spill	Characteristics
K1.8	$K^{\pm}$, $\pi^{\pm}$	<2.0	10^6 K^-	separated
K1.8BR	$K^{\pm}$, $\pi^{\pm}$	<1.1	10^5 K^-	separated
KL	K_L	2.1 in ave.	10^7 K_L	to 16°
High-p	p		10^{10} p	primary protons
	$\pi^{\pm}$	<31	10^7 π	
K1.1	$K^{\pm}$, $\pi^{\pm}$	<1.2	10^6 K^-	separated
		0.7∼0.8		lower momentum [K1.1BR]
HIHR	$\pi^{\pm}$	<2.0	2.8×10^8 π^-	separated $\times 10$ better $\Delta p/p$
K10	$K^{\pm}$, $\pi^{\pm}$, $\bar{p}$	<10	10^7 K^-	separated
new KL	K_L	5.2 in ave.	10^8 K_L	to 5° n/K_L optimized

With K^- beams, currently there is no proposal specific for $S = -1$ hyperons, but the cascades will be studied in the early stage of E50 [235], hopefully in a few years. The beam momentum bite, $\Delta p/p$, is strongly depending on the configuration of the beam line spectrometer, but one can determine beam momentum with the resolution of $\Delta p/p \sim 10^{-3}$ or 10^{-4}. One can think that the systematic study for $S = -1$ hyperons even with charged kaons is desirable and J-PARC folks think that such a study is definitely needed but currently there is no room to accept a new proposal to require a long beamline. J-PARC is focusing on hypernuclei physics [236].

There is no K_L beamline for hyperon physics at J-PARC. It is 100% dedicated to the study of CP-violation. The momentum is spread out from 1 to 4 GeV/c, there is no concept of $\Delta p/p$ since the beam cannot be focused with EM devices.

18.1.3 Belle, Japan

The Belle Collaboration at KEK has plenty of e^+e^- data, and people in Belle [Belle Nuclear Physics Consortium (Belle NPC)] are now extracting various charm-baryon decay processes, which can be used for cascade resonance spectroscopy, from those "raw" e^+e^- data [237, 238].

18.1.4 BaBar, USA

The BaBar Collaboration at SLAC studied, for instance, properties of the $\Xi(1530)^0$ in the decay of $\Lambda_C^+ \to (\pi^+\Xi^-)K^+$ and $\Xi(1690)^0$ in the decay of $\Lambda_C^+ \to (\overline{K^0}\Lambda)K^+$ [239–241] (see, for instance, a recent overview by Ziegler [242]).

18.1.5 $\overline{P}$ANDA, Germany

The $\overline{P}$ANDA experiment [243] will measure annihilation reactions of antiprotons with nucleons and nuclei in order to provide complementary and in part uniquely decisive information on a wide range of QCD aspects. The scientific scope of $\overline{P}$ANDA is ordered into several pillars: hadron spectroscopy, properties of hadrons in matter, nucleon structure and hypernuclei. Antiprotons are produced with a primary proton beam, collected and phase-space cooled in the CR (Collector Ring), and then transferred to the HESR (High Energy Storage Ring) where they are stacked, further phase-space cooled, and then directed onto an internal target located at the center of the $\overline{P}$ANDA detector. The facility will start with a luminosity of 10^{31} cm^2/s and a momentum resolution of $\Delta p/p = 10^{-4}$, and later improve to 2×10^{32} and 4×10^{-5}, respectively. The large cross section into baryon-antibaryon final states (e.g., $\sim 1\ \mu b$ for $\Xi\overline{\Xi}$ or $0.1\ \mu b$ for $\Omega\overline{\Omega}$) make spectroscopic studies of excited multi-strange hyperons a very compelling part of the initial program of $\overline{P}$ANDA, which is expected to commence by 2025 [244].

18.1.6 COMPASS, CERN

COMPASS is thinking of the physics using an RF-separated beam of charged kaons. It is still in the discussion stage. The rates, which were presented as a very first guess by the CERN beamline group were very interesting for a strangeness physics program via diffractive production of strange resonances [245]. The cost of a RF-separated beam is high; however, something like this had been built in the past.

Charged kaons could be used to extend the χPT investigations into the strangeness sector, e.g., to measure the polarizability of the kaon and for a spectroscopy program. At present, COMPASS filters out kaons in the COMPASS charged hadron beam via Cherenkov detectors but they make up only about 2.6% of all beam particles. With an RF-separated kaon beam, they would aim for a more than 20x larger dataset compared to what has been measured so far. This would allow them to perform an analysis, similar to their analysis of pion-beam diffraction: $\pi^- p \to \pi^-\pi^-\pi^+ + p_{\text{recoil}}$ [246]. The energy of the kaon beam would probably be below 100 GeV but above 40 – 50 GeV. The latter number is defined by the stability of the power supplies for the beamline, which after all is about 1 km long.

At these high energies, diffractive production via Pomeron exchange is the dominant process and beam excitations can be well separated from target excitations. This would allow them to collect a clean data sample of kaon-beam diffraction.

19 Appendix A7: Additional Physics Potential with a K_L Beam

As stated in the summary of Mini-Proceedings of the Workshop on Excited Hyperons in QCD Thermodynamics at Freeze-Out (YSTAR2016) [247]: a very interesting further opportunity for the KL Facility is to investigate KL reactions on complex nuclei. By selecting events with the appropriate beam momentum together with a fast forward-going pion, events can be identified, in

which a hyperon is produced at low relative momentum to the target nucleus or even into a bound state. Baryons with strangeness embedded in the nuclear environment, hypernuclei or hyperatoms, are the only available tool to approach the many-body aspect of the three-flavor strong interaction. Furthermore, appropriate events with a forward-going K^+ could deposit a double-strange hyperon into the remaining nucleus, potentially enabling searches for and studies of double-Λ hypernuclei.

Similarly, the scattering of kaons from nuclear targets could be a favorable method to measure the matter form factor (and, therefore, neutron skin) of heavy nuclei, with different and potentially smaller systematics than other probes. The character of the neutron skin, therefore, has a wide impact and the potential to give important new information on neutron star structure and cooling mechanisms [248–252], searches for physics beyond the standard model [253, 254], the nature of 3-body forces in nuclei [255, 256], collective nuclear excitations [257–260] and flows in heavy-ion collisions [261, 262]. Theoretical developments and investigations will be required to underpin such a program, but the science impact of such measurements is high.

Further potential exists to search for – or exclude – possible exotic baryonic states that cannot easily be described by the usual three-valence-quark structure. Recent results from LHCb provide tantalizing hints for the existence of so-called pentaquarks that include a charm valence quark; however, the interpretation of those results is under discussion. In contrast, elastic scattering of K_L with a hydrogen target gives unambiguous information on the potential existence of such states. With the given flux of K_L at the proposed facility, a clear proof of existence or proof of absence will be obtained within the integrated luminosity required for the excited hyperon spectroscopy program that forms the basis of this proposal.

There are two particles in the reaction $K_L p \to \pi Y$ and KY that can carry polarization: the target and recoil baryons. Hence, there are two possible double-polarization experiments: target/recoil. The total number of observables is three. The formalism and definitions of observables commonly used to describe the reaction $K_L p \to KY$ is given in Sec. 7. Although one cannot easily measure recoil polarization with GlueX, the self-analyzing decay of hyperons makes this possible. Double-polarization experiments, using, e.g., a polarized target like FROST [162], will however be left for future proposal(s).

The physics potential connected with studies of CP-violating decays of the K_L is very appealing; however, that topic is not currently the focus of this proposal, since a detailed comparison with the competition from existing and upcoming experiments is needed in order to identify the most attractive measurements that could be done at the proposed KL Facility at JLab.

20 Appendix A8: List of New Equipment and of Changes in Existing Setup Required

The following major changes to existing are summarized below.

- The high intensity photon beam will be produced by a CPS, very similar to the one designed by the JLab CPS group for Halls A/C. A rough cost estimate is about \$1.5–2M per CPS.

Upon accomplishment of a conceptual design, more detailed figures may come in August 2018. In case of the approval at the upcoming PAC meeting, CUA-GW-ODU will apply for the NSF MRI grant or make supplement for available DOE grants.

- Modifications of the beamline from the beginning of the collimator cave to the cryogenic target, which includes the Be-target assembly, the shielding, etc:
  - Engineering and design: 0.5FTE*Y ME and 1FTE*Y MD[5].
  - Equipment: $300k.
  - Changeover from the photon to KL beamline: 4-6 months depending on the type of shielding, at a level of 3.5FTE MT.
  - Changeover from the KL beamline to the photon beamline (after the radiological cooldown of the KL beamline): about 4-5 months.
- The KL flux monitor is being designed by the Edinburgh Univ. team and will cost about $700k. In case of the approval of the proposal at the current PAC meeting, the Edinburgh team will apply for a grant to build this device using UK financial support.
- The upgrade of the LH_2/LD_2 cryogenic target (a rough cost estimate is about $30k).

The total cost of the project is estimated to be on the order of $2.0-2.5M.

[5]ME,MD,MT - mechanical engineer, designer, technician

References

[1] A. Aprahamian *et al.*, *Reaching for the Horizon: The 2015 Long Range Plan for Nuclear Science*; http://science.energy.gov/np/nsac/ .

[2] C. Patrignani *et al.* [Particle Data Group], Chin. Phys. C **40**, no. 10, 100001 (2016).

[3] B. M. K. Nefkens, PiN Newslett. **14**, 150 (1998).

[4] R. Koniuk and N. Isgur, Phys. Rev. Lett. **44**, 845 (1980).

[5] H. Al Ghoul *et al.* [GlueX Collaboration], Phys. Rev. C **95**, no. 4, 042201 (2017).

[6] A. AlekSejevs *et al.* [GlueX Collaboration], arXiv:1305.1523 [nucl-ex].

[7] Y. Qiang, Y. I. Azimov, I. I. Strakovsky, W. J. Briscoe, H. Gao, D. W. Higinbotham, and V. V. Nelyubin, Phys. Lett. B **694**, 123 (2011).

[8] W. J. Briscoe, M. Döring, H. Haberzettl, D. M. Manley, M. Naruki, I. I. Strakovsky, and E. S. Swanson, Eur. Phys. J. A **51**, no. 10, 129 (2015).

[9] Web page of the Workshop on *Physics with Neutral Kaon Beam at JLab* (KL2016), JLab, Newport News, VA, USA, Feb. 2016: https://www.jlab.org/conferences/kl2016/ contains presentations.

[10] Web page of the Workshop on *Excited Hyperons in QCD Thermodynamics at Freeze-Out* (YSTAR2016), JLab, Newport News, VA, USA, Nov. 2016: https://www.jlab.org/conferences/YSTAR2016/ contains presentations.

[11] Web page of the Workshop on *New Opportunities with High-Intensity Photon Sources* (HISP2017), CUA, Washington, DC, USA, Feb. 2017: https://www.jlab.org/conferences/HIPS2017/ contains presentations.

[12] Web page of the Workshop on *Pion-Kaon Interactions* (PKI2018), JLab, Newport News, VA, USA, Feb. 2018: https://www.jlab.org/conferences/pki2018/ contains presentations.

[13] M. Amaryan, Ulf-G. Meißner, C. Meyer, J. Ritman, and I. Strakovsky, eds., Mini-Proceedings, *Workshop on Physics with Neutral Kaon Beam at JLab* (KL2016); arXiv:1604.02141 [hep–ph].

[14] *Physics opportunities with secondary K_L beam at JLab*, Spokesperson: M. Amaryan (GlueX Collaborations), JLab LoI12–15–001, Newport News, VA, USA, 2015.

[15] *Strange hadron spectroscopy with a secondary KL beam at GlueX*, Spokespersons: M. J. Amaryan, M. Bashkanov, J. Ritman, J. R. Stevens, and I. I. Strakovsky (GlueX Collaboration), JLab Proposal PR12–17–001, Newport News, VA, USA, 2017; arXiv:1707.05284 [hep–ex].

[16] *Photoproduction of the very strangest baryons on the proton target in CLAS12*, Spokespersons: L. Guo, M. Dugger, J. Goetz, E. Pasyuk, I.I. Strakovsky, D.P. Watts, N. Zachariou, and V. Ziegler (Very Strange Collaboration for CLAS Collaboration), JLab Proposal E12–11–005A, Newport News, VA, USA, 2013.

[17] *Nucleon resonance structure studies via exclusive KY electroproduction at 6.6 GeV and 8.8 GeV*, Spokespersons: D.S. Carman, R. Gothe, and V. Mokeev (CLAS Collaboration), JLab E12–16–010A, Newport News, VA, USA, 2016.

[18] M. Amaryan, E. Chudakov, K. Rajagopal, C. Ratti, J. Ritman, and I. Strakovsky, eds., Mini-Proceedings, *Workshop on Excited Hyperons in QCD Thermodynamics at Freeze-Out* (YSTAR2016); arXiv:1701.07346 [hep–ph].

[19] T. Horn, C. Keppel, C. Munoz-Camacho, and I. Strakovsky, eds., Mini-Proceedings, *Workshop on High-Intensity Photon Sources* (HIPS2017); arXiv:1704.00816 [nucl–ex].

[20] M. Amaryan, C. Meyer, U.-G. Meißner, J. Ritman, and I. Strakovsky, eds., Mini-Proceedings, *Workshop on Pion-Kaon Interactions* (PKI2018); arXiv:1804.0xxxx [hep–ph].

[21] C. Amsler, S. Eidelman, T. Gutsche, C. Hanhart, S. Spanier, and N.A. Törnqvist, in: Ref. [2]; S. Descotes-Genon and B. Moussallam, Eur. Phys. J. C **48**, 553 (2006).

[22] B. Julia-Diaz, T.-S. H. Lee, T. Sato, and L. C. Smith, Phys. Rev. C **75**, 015205 (2007).

[23] T. Sato and T.-S. H. Lee, J. Phys. G **36**, 073001 (2009).

[24] N. Isgur and M. B. Wise, Phys. Rev. Lett. **66**, 1130 (1991).

[25] R. Aaij *et al.* [LHCb Collaboration], Phys. Rev. Lett. **119**, no. 11, 112001 (2017).

[26] Z. W. Liu, J. M. M. Hall, D. B. Leinweber, A. W. Thomas, and J. J. Wu, Phys. Rev. D **95**, no. 1, 014506 (2017).

[27] J. A. Oller and U.-G. Meißner, Phys. Lett. B **500**, 263 (2001).

[28] A. Cieplý, M. Mai, U.-G. Meißner, and J. Smejkal, Nucl. Phys. A **954**, 17 (2016).

[29] K. Moriya *et al.* [CLAS Collaboration], Phys. Rev. C **87**, no. 3, 035206 (2013).

[30] M. Mai and U.-G. Meißner, Eur. Phys. J. A **51**, no. 3, 30 (2015).

[31] W. Kamleh, J. M. M. Hall, D. B. Leinweber, B. J. Menadue, B. J. Owen, A. W. Thomas, and R. D. Young, PoS CD **15**, 037 (2016).

[32] R. Molina and M. Döring, Phys. Rev. D **94**, no. 5, 056010 (2016) Addendum: [Phys. Rev. D **94**, no. 7, 079901 (2016)].

[33] N. N. Scoccola, H. Nadeau, M. A. Nowak, and M. Rho, Phys. Lett. B **201**, 425 (1988); Erratum: [Phys. Lett. B **220**, 658 (1989)].

[34] C. G. Callan, Jr., K. Hornbostel, and I. R. Klebanov, Phys. Lett. B **202**, 269 (1988).

[35] K. F. Liu, Int. J. Mod. Phys. E **26**, no. 01n02, 1740016 (2017).

[36] L. Y. Glozman and D. O. Riska, Phys. Rept. **268**, 263 (1996).

[37] K. F. Liu, Y. Chen, M. Gong, R. Sufian, M. Sun, and A. Li, PoS LATTICE **2013**, 507 (2014).

[38] F. Coester, K. Dannbom, and D. O. Riska, Nucl. Phys. A **634**, 335 (1998).

[39] M. Luscher, Nucl. Phys. B **354**, 531 (1991).

[40] K. Rummukainen and S. A. Gottlieb, Nucl. Phys. B **450**, 397 (1995).

[41] S. Aoki *et al.* [CP-PACS Collaboration], Phys. Rev. D **76**, 094506 (2007).

[42] X. Feng, K. Jansen, and D. B. Renner, Phys. Rev. D **83**, 094505 (2011).

[43] J. J. Dudek *et al.* [Hadron Spectrum Collaboration], Phys. Rev. D **87**, no. 3, 034505 (2013); Erratum: [Phys. Rev. D **90**, no. 9, 099902 (2014)].

[44] D. Guo, A. Alexandru, R. Molina, and M. Döring, Phys. Rev. D **94**, no. 3, 034501 (2016).

[45] C. Alexandrou *et al.*, Phys. Rev. D **96**, no. 3, 034525 (2017).

[46] J. Bulava, B. Fahy, B. Hz, K. J. Juge, C. Morningstar, and C. H. Wong, Nucl. Phys. B **910**, 842 (2016).

[47] C. B. Lang, D. Mohler, S. Prelovsek, and M. Vidmar, Phys. Rev. D **84**, no. 5, 054503 (2011); Erratum: [Phys. Rev. D **89**, no. 5, 059903 (2014)]

[48] P. Guo, J. Dudek, R. Edwards, and A. P. Szczepaniak, Phys. Rev. D **88**, no. 1, 014501 (2013).

[49] R. A. Briceno and Z. Davoudi, Phys. Rev. D **88**, no. 9, 094507 (2013).

[50] U.-G. Meißner, G. Rios, and A. Rusetsky, Phys. Rev. Lett. **114**, no. 9, 091602 (2015); Erratum: [Phys. Rev. Lett. **117**, no. 6, 069902 (2016)].

[51] C. Liu, X. Feng, and S. He, Int. J. Mod. Phys. A **21**, 847 (2006).

[52] M. Lage, U.-G. Meißner, and A. Rusetsky, Phys. Lett. B **681**, 439 (2009).

[53] D. J. Wilson, R. A. Briceno, J. J. Dudek, R. G. Edwards, and C. E. Thomas, Phys. Rev. D **92**, no. 9, 094502 (2015).

[54] D. J. Wilson, J. J. Dudek, R. G. Edwards, and C. E. Thomas, Phys. Rev. D **91**, no. 5, 054008 (2015).

[55] J. J. Dudek *et al.* [Hadron Spectrum Collaboration], Phys. Rev. Lett. **113**, no. 18, 182001 (2014).

[56] R. A. Briceno, J. J. Dudek, R. G. Edwards, and D. J. Wilson, arXiv:1708.06667 [hep-lat].

[57] R. A. Briceno, J. J. Dudek, R. G. Edwards, and D. J. Wilson, Phys. Rev. Lett. **118**, no. 2, 022002 (2017).

[58] R. G. Edwards, J. J. Dudek, D. G. Richards, and S. J. Wallace, Phys. Rev. D **84**, 074508 (2011).

[59] G. P. Engel *et al.* [BGR Collaboration], Phys. Rev. D **87**, no. 7, 074504 (2013).

[60] J. J. Dudek and R. G. Edwards, Phys. Rev. D **85**, 054016 (2012).

[61] R. G. Edwards *et al.* [Hadron Spectrum Collaboration], Phys. Rev. D **87**, no. 5, 054506 (2013).

[62] R. Bellwied, S. Borsanyi, Z. Fodor, S. D. Katz, and C. Ratti, Phys. Rev. Lett. **111**, 202302 (2013).

[63] S. Borsanyi *et al.* [Wuppertal-Budapest Collaboration], JHEP **1009**, 073 (2010).

[64] A. Bazavov *et al.* [HotQCD Collaboration], Phys. Rev. D **90**, 094503 (2014).

[65] M. Floris, Nucl. Phys. A **931**, 103 (2014).

[66] L. Adamczyk *et al.* [STAR Collaboration], Phys. Rev. Lett. **112**, 032302 (2014).

[67] L. Adamczyk *et al.* [STAR Collaboration], Phys. Rev. Lett. **113**, 092301 (2014).

[68] P. Alba, W. Alberico, R. Bellwied, M. Bluhm, V. Mantovani Sarti, M. Nahrgang, and C. Ratti, Phys. Lett. B **738**, 305 (2014).

[69] J. Adam *et al.* [ALICE Collaboration], Nature Phys. **13**, 535 (2017).

[70] R. Dashen, S. K. Ma, and H. J. Bernstein, Phys. Rev. **187**, 345 (1969).

[71] R. Venugopalan and M. Prakash, Nucl. Phys. A **546**, 718 (1992).

[72] F. Karsch, K. Redlich, and A. Tawfik, Phys. Lett. B **571**, 67 (2003).

[73] A. Tawfik, Phys. Rev. D **71**, 054502 (2005).

[74] R. Hagedorn, Prog. Sci. Culture **1**, 395 (1976).

[75] S. Capstick and N. Isgur, Phys. Rev. D **34**, 2809 (1986).

[76] D. Ebert, R. N. Faustov, and V. O. Galkin, Phys. Rev. D **79**, 114029 (2009).

[77] A. Majumder and B. Muller, Phys. Rev. Lett. **105**, 252002 (2010).

[78] A. Bazavov *et al.*, Phys. Rev. Lett. **113**, no. 7, 072001 (2014).

[79] P. Alba *et al.*, Phys. Rev. D **96**, no. 3, 034517 (2017).

[80] M. M. Giannini and E. Santopinto, Chin. J. Phys. **53**, 020301 (2015).

[81] C. Amsler *et al.* [Particle Data Group], Phys. Lett. B **667**, 1 (2008).

[82] E. Santopinto and J. Ferretti, Phys. Rev. C **92**, no. 2, 025202 (2015).

[83] The Durham HEP Reaction Data Databases (UK) (Durham HepData): http://durpdg.dur.ac.uk/hepdata/reac.html .

[84] M. G. Albrow *et al.*, Nucl. Phys. B **23**, 509 (1970).

[85] M. Albrow, in: *Workshop on Physics with Neutral Kaon Beam at JLab: mini-Proceedings*, arXiv:1604.02141 [hep–ph] (February, 2016), p. 5.

[86] A. D. Brody *et al.*, Phys. Rev. Lett. **22**, 966 (1969).

[87] S. D. Drell and M. Jacob, Phys. Rev. **138**, B1313 (1965).

[88] W. J. Briscoe, I. I. Strakovsky, and R. L. Workman, Institute of Nuclear Studies of The George Washington University Database; http://gwdac.phys.gwu.edu.

[89] G. Höhler and H. Schopper, Berlin, Germany: Springer (1983) 601 P. (Landolt-Börnstein. New Series, I/9B2)

[90] R. A. Arndt, W. J. Briscoe, I. I. Strakovsky, and R. L. Workman, Phys. Rev. C **74**, 045205 (2006).

[91] D. M. Manley, in: *Workshop on Physics with Neutral Kaon Beam at JLab: mini-Proceedings*, arXiv:1604.02141 [hep–ph] (February, 2016), p. 42.

[92] H. Zhang, J. Tulpan, M. Shrestha, and D. M. Manley, Phys. Rev. C **88**, no. 3, 035204 (2013).

[93] H. Zhang, J. Tulpan, M. Shrestha, and D. M. Manley, Phys. Rev. C **88**, no. 3, 035205 (2013).

[94] J. K. Hassall *et al.*, Nucl. Phys. B **189**, 397 (1981).

[95] H. Kamano, S. X. Nakamura, T.-S. H. Lee, and T. Sato, Phys. Rev. C **90**, no. 6, 065204 (2014).

[96] H. Kamano, S. X. Nakamura, T.-S. H. Lee, and T. Sato, Phys. Rev. C **92**, no. 2, 025205 (2015); Erratum: [Phys. Rev. C **95**, no. 4, 049903 (2017)].

[97] B. C. Jackson, Y. Oh, H. Haberzettl, and K. Nakayama, Phys. Rev. C **91**, no. 6, 065208 (2015).

[98] Y. Ikeda, T. Hyodo and W. Weise, Nucl. Phys. A **881**, 98 (2012).

[99] Z. H. Guo and J. A. Oller, Phys. Rev. C **87**, no. 3, 035202 (2013).

[100] A. Cieplý and J. Smejkal, Nucl. Phys. A **881**, 115 (2012).

[101] M. Mai and U.-G. Meißner, Nucl. Phys. A **900**, 51 (2013)

[102] P. C. Bruns, M. Mai, and U.-G. Meißner, Phys. Lett. B **697**, 254 (2011).

[103] D. Aston *et al.*, Phys. Lett. B **201**, 169 (1988).

[104] J. R. Pelaez, Phys. Rept. **658**, 1 (2016).

[105] P. Masjuan, J. Ruiz de Elvira, and J. J. Sanz-Cillero, Phys. Rev. D **90**, no. 9, 097901 (2014).

[106] S. M. Roy, Phys. Lett. **36B**, 353 (1971).

[107] F. Steiner, Fortsch. Phys. **19**, 115 (1971).

[108] S. Descotes-Genon and B. Moussallam, Eur. Phys. J. C **48**, 553 (2006).

[109] J. R. Pelaez, A. Rodas, and J. Ruiz de Elvira, Eur. Phys. J. C **77**, no. 2, 91 (2017).

[110] D. Aston *et al.*, Nucl. Phys. B **292**, 693 (1987).

[111] D. Aston *et al.*, Nucl. Phys. B **296**, 493 (1988).

[112] B.R. Martin, D. Morgan, and G. Shaw, Pion Pion Interactions in Particle Physics (Academic press, London, 1976).

[113] P. Estabrooks, R. K. Carnegie, A. D. Martin, W. M. Dunwoodie, T. A. Lasinski, and D. W. G. S. Leith, Nucl. Phys. B **133**, 490 (1978).

[114] C. B. Lang, Fortsch. Phys. **26**, 509 (1978).

[115] D. R. Boito, R. Escribano, and M. Jamin, JHEP **1009**, 031 (2010).

[116] P. del Amo Sanchez *et al.* [BaBar Collaboration], Phys. Rev. D **83**, 072001 (2011).

[117] D. Epifanov *et al.* [Belle Collaboration], Phys. Lett. B **654**, 65 (2007).

[118] M. Antonelli *et al.* [FlaviaNet Working Group on Kaon Decays], Eur. Phys. J. C **69**, 399 (2010).

[119] F. Niecknig and B. Kubis, JHEP **1510**, 142 (2015).

[120] V. Bernard, N. Kaiser, and U. G. Meissner, Phys. Rev. D **43**, 2757 (1991).

[121] B. Adeva *et al.* [DIRAC Collaboration], Phys. Rev. D **96**, 052002 (2017).

[122] C. B. Lang, L. Leskovec, D. Mohler, and S. Prelovsek, Phys. Rev. D **86**, 054508 (2012).

[123] S. Prelovsek, L. Leskovec, C. B. Lang, and D. Mohler, Phys. Rev. D **88**, no. 5, 054508 (2013).

[124] R. Brett, J. Bulava, J. Fallica, A. Hanlon, B. Hz and C. Morningstar, arXiv:1802.03100 [hep-lat].

[125] J. Gasser and U.-G. Meißner, Nucl. Phys. B **357**, 90 (1991).

[126] U.-G. Meißner and J. A. Oller, Nucl. Phys. A **679**, 671 (2001).

[127] J. A. Oller, E. Oset, and J. E. Palomar, Phys. Rev. D **63**, 114009 (2001).

[128] M. Frink, B. Kubis, and U.-G. Meißner, Eur. Phys. J. C **25**, 259 (2002).

[129] J. Bijnens and P. Talavera, Nucl. Phys. B **669**, 341 (2003).

[130] T. A. Lahde and U.-G. Meißner, Phys. Rev. D **74**, 034021 (2006).

[131] V. Bernard and E. Passemar, JHEP **1004**, 001 (2010).

[132] Z. H. Guo, J. A. Oller, and J. Ruiz de Elvira, Phys. Rev. D **86**, 054006 (2012).

[133] J. F. Donoghue, J. Gasser, and H. Leutwyler, Nucl. Phys. B **343**, 341 (1990).

[134] V. Bernard and E. Passemar, Phys. Lett. B **661**, 95 (2008).

[135] J. R. Pelaez and A. Rodas, Eur. Phys. J. C **77**, no. 6, 431 (2017).

[136] M. Döring, U.-G. Meißner, and W. Wang, JHEP **1310**, 011 (2013).

[137] P. Büttiker, S. Descotes-Genon, and B. Moussallam, Eur. Phys. J. C **33**, 409 (2004).

[138] https://wiki.jlab.org/cuawiki/images/3/32/Sergey_Abrahamyan_WACS_NPS_2014_update.pdf

[139] *Polarization observables in wide-angle Compton scattering at photon energies up to 8 GeV*, Spokespersons: B. Wojtsekhowski, S. Abrahamyan, and G. Niculescu (Neutral Particle Spectrometer Collaboration), JLab Proposal PR12–15–003, Newport News, VA, USA, 2015.

[140] P. Degtyarenko and B. Wojtsekhowski, in: *Workshop on Physics with Neutral Kaon Beam at JLab: mini-Proceedings*, arXiv:1604.02141 [hep–ph] (February, 2016), p. 214.

[141] T. Horn, C. Keppel, C. Munoz-Camacho and I. Strakovsky, in: *Workshop on New Opportunities with High-Intensity Photon Sources: mini-Proceedings*, arXiv:1704.00816 [nucl–ex] (February, 2017), p. 61.

[142] M. Bashkanov *et al.* Flux monitor memo.

[143] We used a modified version of the Pythia package for the GlueX Collaboration at JLab Hall D, http://home.thep.lu.se/torbjorn/Pythia.html

[144] A. I. Titov and T. S. H. Lee, Phys. Rev. C **67**, 065205 (2003).

[145] G. Mcclellan, N. B. Mistry, P. Mostek, H. Ogren, A. Osborne, J. Swartz, R. Talman, and G. Diambrini-Palazzi, Phys. Rev. Lett. **26**, 1593 (1971).

[146] A. I. Titov and B. Kampfer, Phys. Rev. C **76**, 035202 (2007).

[147] T. Mibe *et al.* [CLAS Collaboration], Phys. Rev. C **76**, 052202 (2007).

[148] G. W. Brandenburg *et al.*, Phys. Rev. D **7**, 708 (1973).

[149] I. Larin, in: *Workshop on Physics with Neutral Kaon Beam at JLab: mini-Proceedings*, arXiv:1604.02141 [hep–ph] (February, 2016), p. 198.

[150] Application Software Group, GEANT - *Detector Description and Simulation Tool*, CERN Program Library Long Writeup W5013, CERN, Geneva, Switzerland (1994).

[151] L. Keller, private communication, 2015.

[152] J. Allison *et al.*, Nucl. Instrum. Meth. A **835**, 186 (2016).

[153] Y. Qiang, C. Zorn, F. Barbosa, and E. Smith, Nucl. Instrum. Meth. A **698**, 234 (2013).

[154] T. Goorley *et al.*, Nucl. Tech. **180**, 298. (2012); https://mcnp.lanl.gov/ .

[155] ICRP 116 Publication, *Conversion Coefficients for Radiological Protection Quantities for External Radiation Exposures*, Annals of the ICRP, **40**, No 2-5 (2010).

[156] D. Androic *et al.* [G0 Collaboration], Nucl. Instrum. Meth. A **646**, 59 (2011).

[157] M. Spata, private communication, 2016.

[158] E. Pooser, Ph.D. Thesis, Florida International University (2016).

[159] F. Barbosa, C. Hutton, A. Sitnikov, A. Somov, S. Somov, and I. Tolstukhin, Nucl. Instrum. Meth. A **795**, 376 (2015).

[160] G.A. Slayer*et al.*, Phys. Rev. **169**, 1045 (1968).

[161] K.G. Vorsburgh *et al.*, Phys. Rev. D **6**, 1834 (1972).

[162] C. Keith, in: *Workshop on Physics with Neutral Kaon Beam at JLab: mini-Proceedings*, arXiv:1604.02141 [hep–ph] (February, 2016), p. 223.

[163] D. Meekins, TGT-CALC-401-007: *Hall D Cryogenic Target: General calculations for relief of the LH_2 target*.

[164] H. Seraydaryan *et al.* [CLAS Collaboration], Phys. Rev. C **89**, no. 5, 055206 (2014).

[165] H. Al Ghoul *et al.* [GlueX Collaboration], AIP Conf. Proc. **1735**, 020001 (2016).

[166] S. Taylor, in: *Workshop on Physics with Neutral Kaon Beam at JLab: mini-Proceedings*, arXiv:1604.02141 [hep–ph] (February, 2016), p. 205.

[167] P. Capiluppi, G. Giacomelli, G. Mandrioli, A. M. Rossi, P. Serra-Lugaresi, and L. Zitelli, IFUB-81-25.

[168] R. Yamartino *et al.*, Phys. Rev. D**10**, 9 (1974), Ph. D Thesis, SLAC Standford University, 1974; SLAC-R-0177, SLAC-R-177, SLAC-0177, SLAC-177.

[169] D. A. Sharov, V. L. Korotkikh, and D. E. Lanskoy, Eur. Phys. J. A **47**, 109 (2011).

[170] S. F. Biagi *et al.*, Z. Phys. C **34**, 175 (1987).

[171] J. C. M. Armitage *et al.*, Nucl. Phys. B **123**, 11 (1977).

[172] D. Cline, J. Penn and D. D. Reeder, Nucl. Phys. B **22**, 247 (1970).

[173] P. Bajllon *et al.*, Nucl. Phys. B **134**, 31 (1978).

[174] A. V. Anisovich and A. V. Sarantsev, Phys. Lett. B **413**, 137 (1997). [hep-ph/9705401].

[175] C. Cawlfield *et al.* [CLEO Collaboration], Phys. Rev. D **74**, 031108 (2006).

[176] R. Delbourgo and M. D. Scadron, Int. J. Mod. Phys. A **13**, 657 (1998).

[177] M. D. Scadron, F. Kleefeld, G. Rupp and E. van Beveren, Nucl. Phys. A **724**, 391 (2003).

[178] Z. Y. Zhou and H. Q. Zheng, Nucl. Phys. A **775**, 212 (2006).

[179] J. Prevost *et al.* [Cern-Heidelberg-Saclay Collaboration], Nucl. Phys. B **69**, 246 (1974).

[180] W. Cameron *et al.* [Rutherford-London Collaboration], Nucl. Phys. B **143**, 189 (1978).

[181] J. Timmermans *et al.* [Amsterdam-CERN-Nijmegen-Oxford Collaboration], Nucl. Phys. B **112**, 77 (1976).

[182] W. Cameron *et al.* [Rutherford-London Collaboration], Nucl. Phys. B **131**, 399 (1977).

[183] S. Ceci, M. Döring, C. Hanhart, S. Krewald, U.-G. Meißner, and A. Švarc, Phys. Rev. C **84**, 015205 (2011).

[184] V. D. Burkert *et al.*, arXiv:1412.0241 [nucl-ex].

[185] A. Mueller- Groeling, K. Holinde, and J. Speth, Nucl. Phys. A **513**, 557 (1990).

[186] M. Mai, B. Hu, M. Doring, A. Pilloni, and A. Szczepaniak, Eur. Phys. J. A **53**, no. 9, 177 (2017).

[187] A. V. Anisovich, R. Beck, E. Klempt, V. A. Nikonov, A. V. Sarantsev and U. Thoma, Eur. Phys. J. A **48**, 15 (2012).

[188] H. Osmanović, Talk at The International Workshop on Partial Wave Analyses and Advanced Tools for Hadron Spectroscopy (PWA9/ATHOS4, Bad Honnef near Bonn (Germany), March, 2017.

[189] A. Švarc, Talk at The International Workshop on Partial Wave Analyses and Advanced Tools for Hadron Spectroscopy (PWA9/ATHOS4, Bad Honnef near Bonn (Germany), March, 2017.

[190] G. Hohler, PiN Newslett. **1993**, no. 9, 1 (1993).

[191] N. G. Kelkar and M. Nowakowski, Phys. Rev. A **78**, 012709 (2008); and references therein.

[192] G. F. Chew and S. Mandelstam, Phys. Rev. **119**, 467 (1960).

[193] S. Ceci, J. Stahov, A. Švarc, S. Watson, and B. Zauner, Phys. Rev. D **77**, 116007 (2008).

[194] P. Masjuan, J. Ruiz de Elvira, and J. J. Sanz-Cillero, Phys. Rev. D **90**, no. 9, 097901 (2014).

[195] A. Š, M. Hadžimehmedović, H. Osmanović, J. Stahov, L. Tiator, and R. L. Workman, Phys. Rev. C **88**, no. 3, 035206 (2013).

[196] A. Š, M. Hadžimehmedović, R. Omerović, H. Osmanović, and J. Stahov, Phys. Rev. C **89**, no. 4, 045205 (2014).

[197] A. Š, M. Hadžimehmedović, H. Osmanović, J. Stahov, L. Tiator, and R. L. Workman, Phys. Rev. C **89**, no. 6, 065208 (2014).

[198] A. Š, M. Hadžimehmedović, H. Osmanović, J. Stahov, and R. L. Workman, Phys. Rev. C **91**, no. 1, 015207 (2015).

[199] A. Š, M. Hadžimehmedović, H. Osmanović, J. Stahov, L. Tiator, and R. L. Workman, Phys. Lett. B **755**, 452 (2016).

[200] Michiel Hazewinkel: Encyclopaedia of Mathematics, Vol.**6**, Springer, 31. 8. 1990, pg. 251.

[201] S. Ciulli and J. Fischer, Nucl. Phys. **24**, 465 (1961).

[202] I. Ciulli, S. Ciulli, and J. Fisher, Nuovo Cimento **23**, 1129 (1962).

[203] E. Pietarinen, Nuovo Cim. A **12**, 522 (1972).

[204] E. Pietarinen, Nucl. Phys. B **107**, 21 (1976).

[205] R. L. Workman, M. W. Paris, W. J. Briscoe, and I. I. Strakovsky, Phys. Rev. C **86**, 015202 (2012).

[206] D. Rönchen *et al.*, Eur. Phys. J. A **49**, 44 (2013).

[207] M. Döring, C. Hanhart, F. Huang, S. Krewald, U.-G. Meißner, and D. Rönchen, Nucl. Phys. A **851**, 58 (2011).

[208] M. Döring, C. Hanhart, F. Huang, S. Krewald and U.-G. Meißner, Nucl. Phys. A **829**, 170 (2009).

[209] R. A. Arndt, I. I. Strakovsky and R. L. Workman, Phys. Rev. C **68**, 042201 (2003); Erratum: [Phys. Rev. C **69**, 019901 (2004)];

[210] Y. I. Azimov, R. A. Arndt, I. I. Strakovsky and R. L. Workman, Phys. Rev. C **68**, 045204 (2003).

[211] A. V. Anisovich, E. Klempt, V. A. Nikonov, A. V. Sarantsev, H. Schmieden and U. Thoma, Phys. Lett. B **711**, 162 (2012).

[212] R. Tibshirani, J.R. Statist. Soc. B **58**, 267 (1996).

[213] *The Elements of Statistical Learning: Data Mining, Inference, and Prediction*, T. Hasti, R. Tibshirani, J. Friedman, Springer 2009. second ed.; E-book available at http://statweb.stanford.edu/ tibs/ElemStatLearn/index.html .

[214] *An Introduction to Statistical Learning*, Gareth James, Daniela Witten, Trevor Hastie and Robert Tibshirani, Springer 2015; 6th printing; E-book available at http://www-bcf.usc.edu/ gareth/ISL/ .

[215] B. Guegan, J. Hardin, J. Stevens, and M. Williams, JINST **10**, no. 09, P09002 (2015).

[216] J. Landay, M. Döring, C. Fernández-Ramírez, B. Hu, and R. Molina, Phys. Rev. C **95**, no. 1, 015203 (2017).

[217] D. Agadjanov, M. Döring, M. Mai, U.-G. Meißner, and A. R0usetsky, JHEP **1606**, 043 (2016).

[218] G. D'Agostini, Nucl. Instrum. Meth. A **346**, 306 (1994).

[219] R. D. Ball *et al.* [NNPDF Collaboration], JHEP **1005**, 075 (2010).

[220] L. Wilkinson and G.E. Dallal, Technometrics **23**, 377 (1981).

[221] T. W. Anderson and D. A. Darling, Annals of Mathematical Statistics **23**, 193 (1952).

[222] M. A. Stephens, Journal of the American Statistical Association **69**, 730 (1974).

[223] M. Döring, J. Revier, D. Rönchen, and R. L. Workman, Phys. Rev. C **93**, no. 6, 065205 (2016).

[224] KLong bi-weekly group meeting, https://wiki.jlab.org/klproject/index.php/March-1st,-2017.

[225] Y. Valdau *et al.*, Phys. Rev. C **84**, 055207 (2011).

[226] P. Adlarson *et al.* [WASA-at-COSY Collaboration], Phys. Lett. B **774**, 599 (2017).

[227] *Project X Physics Study*, https://indico.fnal.gov/event/projectxps12 .

[228] S. D. Holmes *et al.*, arXiv:1306.5022 [physics.acc-ph].

[229] A. S. Kronfeld *et al.*, arXiv:1306.5009 [hep-ex].

[230] D. M. Asner *et al.*, arXiv:1306.5024 [physics.acc-ph].

[231] C. Quigg, private communication, 2015.

[232] B. Winstein *et al.*, *High precision, high intensitivity K^0 physics at the main injector*, FNAL LoI 0804, 1988.

[233] *Summary of the Report from the Working Group for The External Expert Panel on the Radioactive Material Leak Accident at the Hadron Experimental Facility of J-PARC*; http://j-parc.jp/en/topics/HDAccident20130827_02.p

[234] H. Fujioka *et al.*, arXiv:1706.07916 [nucl-ex].

[235] H. Noumi *et al.*, *Charmed baryon spectroscopy experiment at J-PARC*, J-PARC Proposal E50, 2012.

[236] M. Naruki, private communication, 2015.

[237] K. Abe *et al.* [Belle Collaboration], Phys. Lett. B **524**, 33 (2002).

[238] T. Lesiak *et al.* [Belle Collaboration], Phys. Lett. B **605**, 237 (2005); Erratum: [Phys. Lett. B **617**, 198 (2005)].

[239] B. Aubert *et al.* [BaBar Collaboration], Phys. Rev. D **78**, 034008 (2008).

[240] B. Aubert *et al.* [BaBar Collaboration], Phys. Rev. Lett. **97**, 112001 (2006).

[241] B. Aubert *et al.* [BaBar Collaboration], Phys. Rev. Lett. **95**, 142003 (2005).

[242] V. Ziegler, in: *Workshop on Physics with Neutral Kaon Beam at JLab: mini-Proceedings*, arXiv:1604.02141 [hep–ph] (February, 2016), p. 113.

[243] M. F. M. Lutz *et al.* [PANDA Collaboration], arXiv:0903.3905 [hep-ex].

[244] J. Ritman, invited talk at *Excited Hyperons in QCD Thermodynamics at Freeze-Out* Workshop, see Ref. [10].

[245] S. Paul, private communication, 2016.

[246] C. Adolph *et al.* [COMPASS Collaboration], Phys. Rev. D **95**, no. 3, 032004 (2017).

[247] J. Goity, P. Huovinen, J. Ritman, and A, Tang, in: Workshop on *Excited Hyperons in QCD Thermodynamics at Freeze-Out: mini-Proceedings*, arXiv:1701.07346 [hep–ph], (November, 2016) p. 158.

[248] A. W. Steiner, M. Prakash, J. M. Lattimer, and P. J. Ellis, Phys. Rept. **411**, 325 (2005).

[249] C. J. Horowitz and J. Piekarewicz, Phys. Rev. Lett. **86**, 5647 (2001).

[250] J. Xu, L. W. Chen, B. A. Li, and H. R. Ma, Astrophys. J. **697**, 1549 (2009).

[251] A. W. Steiner, J. M. Lattimer, and E. F. Brown, Astrophys. J. **722**, 33 (2010).

[252] B. G. Todd-Rutel and J. Piekarewicz, Phys. Rev. Lett. **95**, 122501 (2005).

[253] D. H. Wen, B. A. Li, and L. W. Chen, Phys. Rev. Lett. **103**, 211102 (2009).

[254] S. J. Pollock and M. C. Welliver, Phys. Lett. B **464**, 177 (1999).

[255] M. B. Tsang *et al.*, Phys. Rev. C **86**, 015803 (2012).

[256] K. Hebeler, J. M. Lattimer, C. J. Pethick, and A. Schwenk, Phys. Rev. Lett. **105**, 161102 (2010).

[257] M. Centelles, X. Roca-Maza, X. Vinas, and M. Warda, Phys. Rev. Lett. **102**, 122502 (2009).

[258] A. Carbone, G. Colo, A. Bracco, L. G. Cao, P. F. Bortignon, F. Camera, and O. Wieland, Phys. Rev. C **81**, 041301 (2010).

[259] L. W. Chen, C. M. Ko, B. A. Li and J. Xu, Phys. Rev. C **82**, 024321 (2010).

[260] A. Tamii *et al.*, Phys. Rev. Lett. **107**, 062502 (2011).

[261] B. A. Li, L. W. Chen, and C. M. Ko, Phys. Rept. **464**, 113 (2008).

[262] M. B. Tsang, Y. Zhang, P. Danielewicz, M. Famiano, Z. Li, W. G. Lynch, and A. W. Steiner, Phys. Rev. Lett. **102**, 122701 (2009).

[263] M. J. Amaryan, W. J. Briscoe, P. Degtyarenko, A. Somov, J. R. Stevens, I. I. Strakovsky, and T. Whitlatch, Preprint JLAB-TN-18-0xx, 2018.

[264] E. Pooser, F. Barbosa, W. Boeglin, C. Hutton, M. Ito, M. Kamel, P. Khetarpal, A. LLodra, N. Sandoval, S. Taylor, C. Yero, T. Whitlatch, S. Worthington, and B. Zihlmann, to be submitted to Nucl. Instrum. Meth. A.

[265] T. D. Beattie, A. M. Foda, C. L. Henschel, S. Katsaganis, G. J. Lolosa, Z. Papandreou *et al.* to be submitted to Nucl. Instrum. Meth. A.

[266] P. Degtiarenko, A. Fass, G. Kharashvili, and A. Somov, Preprint JLAB-TN-11-005, 2011.

[267] *Pion photoproduction from a polarized target*, Spokespersons: N. Benmouna, W. J. Briscoe, I. I. Strakovsky, S. Strauch, and G. V. O'Rially (CLAS Collaborations), JLab Proposal E-03-105, Newport News, VA, USA, 2003.

[268] I. G. Alekseev *et al.* (EPECUR Collaboration), Phys. Rev. C **91**, 025205 (2015).

[269] GlueX wiki: https://halldweb.jlab.org/wiki/images/d/df/CollimatorElevationSept08.png ; S. Worthington, private communication, 2018..

[270] M. Bashkanov *et al.*, *Flux Monitor Memo*.

[271] A. Somov, Preprint GlueX–doc–1646, 2011.